

ABSTRACT

Title of dissertation: GAMMA-RAY BURSTS: LIGHTING
UP THE HIGH-REDSHIFT UNIVERSE

Vicki Louise Toy
Doctor of Philosophy, 2017

Dissertation directed by: Professor Sylvain Veilleux
Department of Astronomy

Gamma-ray bursts (GRBs) are the most luminous events in the Universe with $E_{\gamma,\text{iso}} \sim 10^{48-54}$ erg. Leading models hypothesize that GRBs are created from internal collisions within collimated and ultrarelativistic jets. The jets then shock-heat the surrounding material (e.g. interstellar medium) to create GRB afterglows. These afterglows are extremely useful probes of the Universe because long GRBs are (1) bright events that can be used as backlights for absorption studies, (2) able to probe at all redshifts massive stars exist, and (3) transient events that allow us to follow-up on the host galaxies at late times. In this thesis we study the environments of GRBs.

We first explore the relationship between GRB and supernova (SN) using a nearby GRB-SN (GRB 130702A/SN 2013dx) at $z = 0.145$. There are only nine other GRB-SNe that were close enough to have extensive spectroscopic and photometric follow-up of the SN at late times. We create a quasi-bolometric light curve of SN 2013dx and fit an analytical equation to the quasi-bolometric light curve combined

with measurements of the photospheric velocity to determine SN parameters: mass of ^{56}Ni , kinetic energy, and ejecta mass. We examine the relationship between SN parameters and $E_{\gamma,\text{iso}}$ for the 10 well-studied GRB-SNe, but find no correlations despite numerical simulation predictions that the mass of ^{56}Ni should correlate with the degree of asymmetry.

We then move to larger distance scales and use GRB afterglows as bright backlights to study distant galaxies. We examine the galactic environments of Damped Lyman- α systems (DLAs; $N_{\text{HI}} \geq 10^{20.3}\text{cm}^{-2}$) identified with GRB afterglows at $z \sim 2 - 6$. We use late-time photometry after the GRB afterglow has faded to determine star formation rates (SFRs) from rest-frame ultraviolet measurements or spectral energy distribution (SED) models from multiband photometry. We compare our sample's SFRs to a sample of quasars (QSOs) DLA host galaxies. Despite the overlapping N_{HI} and redshift ranges, our GRB-DLA galaxies have much larger SFRs than the QSO-DLA host galaxy sample; this may suggest that the QSO-DLA and GRB-DLA galaxy populations are different. We also compare star formation efficiencies to the local Universe and simulations at $z = 3$.

A large portion of this thesis has focused on the development of a new ground-based GRB afterglow follow-up instrument, the Rapid infrared IMager-Spectrometer (RIMAS), that will target high-redshift GRB afterglows to study early galaxy environments. RIMAS covers 0.97-2.37 μm and can simultaneously observe two bandpasses in any observing mode: photometry, low-resolution spectroscopy ($R \sim 30$), or high-resolution spectroscopy ($R \sim 4000$).

In particular, this thesis focuses on RIMAS's three detectors: two science grade

Teledyne HgCdTe Astronomy Wide Area Infrared Imager with 2K x 2K, Reference Pixels and Guide Mode (H2RG) and a slit-viewer *Spitzer* Legacy Indium-Antimonide (InSb) array. We describe the detector hardware and characterization in detail and discuss general infrared detector troubleshooting methods at both cryogenic and room temperatures.

Several software packages have been developed for RIMAS throughout this thesis work. We introduce RIMAS's quick reduction pipeline that takes raw images from a single acquisition and returns a single result frame. We then present a generalized data reduction pipeline that we have tested on two currently operational photometers. We also describe our detailed and realistic RIMAS throughput models for all three observing modes as well as our online observer calculators with these throughput models. All of our data products are open source and are publicly available on Github repositories with detailed documentation.

GAMMA-RAY BURSTS: LIGHTING
UP THE HIGH-REDSHIFT UNIVERSE

by

Vicki Louise Toy

Dissertation submitted to the Faculty of the Graduate School of the
University of Maryland, College Park in partial fulfillment
of the requirements for the degree of
Doctor of Philosophy
2017

Advisory Committee:
Professor Sylvain Veilleux, Chair/Advisor
Dr. Alexander Kutyrev, Co-Advisor
Dr. S. Bradley Cenko
Professor Andrew Harris
Professor Suvi Gezari
Professor Eun-Suk Seo

© Copyright by
Vicki Louise Toy
2017

Preface

Large portions of this thesis have been published in peer-reviewed journals and presented at international conferences. Chapter 2 was published in the *Astrophysical Journal* as “Optical and Near-infrared Observations of SN 2013dx Associated with GRB 130702A” (Toy et al., 2016c). Chapter 3 was also published in the *Astrophysical Journal* as “Exploring Damped Lyman- α System Host Galaxies using Gamma-ray Bursts” (Toy et al., 2016a). Portions of chapter 4 and chapter 5 were previously published in non-refereed SPIE conference proceeding manuscripts (Toy et al., 2014, 2016b).

To my dad who always pushes me to do my best. To my mom who is always there for me. To my brother who taught me to be tough. And most of all to my husband, Wes, my rock and who words would not do justice.

Acknowledgments

There are a lot of people who have made this thesis possible. I would first like to thank my advisors, Alexander Kutyrev and Sylvain Veilleux, for their advice and support throughout the last five years on anything and everything RIMAS. I would also like to thank Brad Cenko and Nino Cucchiara for their patience and understanding and for teaching me how to observe. This work also would not have been possible without the hard work of the rest of the RIMAS team: John Capone, Thomas Hams, Dave Robinson, Gennadiy Lotkin, Kenichi Sakai, Harvey Moseley, Neil Gehrels, and Stuart Vogel. Thank you also to Andrew Harris, Suvi Gezari, and Eun-Suk Seo for agreeing to be on my thesis committee.

The UMD Department of Astronomy has become like a home to me and I owe that to the amazing community that my colleagues have created. In particular, I want to thank my wonderful Goddard friends, Maxime Rizzo and John Capone, who have encouraged and taught me so much. Many thanks to my friend Taro Shimizu who convinced me to come to UMD. I also have to thank my classmates Johnny Vanlandingham, Krista Smith, Ron Ballouz, and Gabriele Betancourt for being there for me throughout this roller coaster ride, I couldn't have made it through without our 2nd year hangouts (even though we aren't 2nd years anymore).

Ever since I was 9 years old I have dreamt of working at NASA and I was lucky enough to live out my dreams during this journey. My family has always been supportive of this dream and I am grateful to my dad, mom, and brother who always encouraged me to follow my passion even though I marched to the tune of a different

drummer. They always gave me wonderful advice and more importantly were there when I needed them the most. I also have to thank my wonderful extended family who supported and encouraged me at every turn.

Finally, I owe my deepest gratitude to my husband and partner, Wes. Thank you for your unconditional support and encouragement. You have been my strongest ally and most important supporter. You have been there for me in the lowest lows and the highest highs. I could not have done this without you.

Table of Contents

List of Tables	ix
List of Figures	x
List of Abbreviations	xii
1 Introduction	1
1.1 Gamma-ray Bursts	1
1.1.1 Short History	1
1.1.2 What Are Gamma-Ray Bursts?	5
1.1.3 Gamma-ray Burst Models	7
1.1.3.1 Gamma-ray Burst Progenitors	8
1.1.4 Gamma-ray Burst Afterglow Model	10
1.1.5 Detection Methods	11
1.2 Gamma-ray Burst Host Galaxies	14
1.2.1 Galaxy Properties	14
1.2.2 Reionization	16
1.3 Outline of Thesis	18
1.3.1 Open Issues	18
1.3.2 Organization	18
2 GRB 130702A/SN 2013dx	21
2.1 Introduction	21
2.2 GRB 130702A/SN 2013dx	23
2.3 Observations and Data Reduction	26
2.3.1 Optical/Near-Infrared Imaging	26
2.3.1.1 P60 Photometry	27
2.3.1.2 LT Photometry	27
2.3.1.3 RATIR Photometry	28
2.3.1.4 Keck/LRIS Photometry	28
2.3.1.5 Keck/MOSFIRE Photometry	29
2.3.1.6 LMI/DCT Photometry	30

2.3.2	Optical Spectroscopy	30
2.3.3	X-Ray Observations	32
2.4	Light-Curve Analysis	33
2.4.1	Isolating the Supernova Component	33
2.4.2	Comparison with SN 1998bw	39
2.4.3	Bolometric Light Curve	41
2.5	Spectral Analysis	44
2.5.1	Isolating the SN Component	44
2.5.2	Comparison with Other Type Ic-BL SNe	45
2.5.3	Photospheric Velocity Measurements	47
2.5.4	Line Identification	48
2.6	Supernova Explosion Parameters	51
2.6.1	Derived Parameters	51
2.6.2	Comparison with Other GRB-SNe	53
2.6.3	Caveats and Conclusions	56
2.7	Discussion and Summary	60
3	GRB-DLA host counterparts	67
3.1	Introduction	67
3.2	Sample and data reduction	72
3.2.1	Sample	72
3.2.2	LMI data reduction	73
3.2.3	Comparison to other samples	74
3.3	Star Formation	77
3.3.1	Star Formation Rates	78
3.3.1.1	SED fitting Star Formation Rate	80
3.3.1.2	Single band UV Star Formation Rate	81
3.3.1.3	DLA host Star Formation Rates	83
3.3.2	Kennicutt-Schmidt relation	87
3.3.2.1	Surface Density Estimates	87
3.3.2.2	Comparison with star formation laws & simulations	89
3.4	Enrichment time	93
3.5	Summary and Conclusions	96
4	RIMAS: Hardware	104
4.1	RIMAS Overview	104
4.1.1	Discovery Channel Telescope	104
4.1.2	RIMAS design	106
4.2	RIMAS Detectors	109
4.2.1	Detector Introduction	110
4.2.1.1	Semiconductors	110
4.2.1.2	Semiconductor Material	111
4.2.1.3	Detector Types	112
4.2.2	Operating hybrid detectors	115
4.2.2.1	Multiplexer sampling modes	118

4.2.3	RIMAS detector drivers	120
4.2.3.1	Leach/ARC detector driver	120
4.2.3.2	Labview detector driver	122
4.2.4	Detector characterization parameters	123
4.2.4.1	Quantum efficiency	123
4.2.4.2	Conversion gain	124
4.2.4.3	Read noise	125
4.2.4.4	Dark current	125
4.2.4.5	Linearity	126
4.2.4.6	Saturation	126
4.2.4.7	Dynamic range	126
4.2.4.8	Persistence	127
4.2.5	RIMAS H2RG Detectors Characterization	127
4.2.5.1	H2RG Detectors: Conversion Gain	128
4.2.5.2	H2RG Detectors: Linearity and Saturation	129
4.2.5.3	H2RG Detectors: Read noise	132
4.2.5.4	H2RG Detectors: Dynamic Range	132
4.2.5.5	H2RG Detectors: Dark Current	133
4.2.6	RIMAS InSb Detector Characterization	135
4.2.6.1	InSb Detector: Conversion gain	135
4.2.6.2	InSb Detector: Linearity and saturation	136
4.2.6.3	InSb Detector: Read Noise	138
4.2.6.4	InSb Detector: Dynamic Range	139
4.2.7	Troubleshooting near-infrared hybrid detectors	139
4.2.7.1	Testing detector driver systems	140
4.2.7.2	Testing detectors at room temperature	140
4.2.7.3	Testing detectors at cryogenic temperatures	145
5	RIMAS: Software	147
5.1	RIMAS Quick Reduce Data Pipeline	147
5.2	Generalized Photometric Data Reduction Pipeline	148
5.2.1	Preprocessing Stage	150
5.2.2	Data Reduction Stage	150
5.2.3	Photometry Stage	154
5.2.4	Pipeline Applications	155
5.3	RIMAS Instrument Throughput Models	155
5.4	RIMAS Observing Calculators	156
5.4.1	Limiting Magnitudes	157
5.4.2	Exposure time calculator	159
5.4.3	Guide Star Calculations	161
6	Final considerations	165
	Bibliography	168

List of Tables

2.1	GRB-SN References	22
2.2	Log of Spectroscopic Observations	26
2.3	SN 1998bw Template Fits	39
2.4	Velocity of Si II λ 6355	48
2.5	Physical Parameters of GRB-SNe	54
2.6	Photometry References for SN 1998bw-Independent Bolometric Light Curves	58
2.7	Observing Log	63
3.1	GRB-DLA Host Galaxy Sample	100
3.1	GRB-DLA Host Galaxy Sample	101
3.1	GRB-DLA Host Galaxy Sample	102
3.2	GRB sub-DLA Host Galaxy Sample	103
4.1	RIMAS H2RG Detector Characteristics	128
4.2	RIMAS InSb Slit-viewer Detector Characteristics	135
5.1	Slit-viewer Limiting Magnitude SNR=5	161
5.2	Guide Star Probabilities SNR=5	163

List of Figures

1.1	BATSE GRB light curve diversity	2
1.2	BATSE sky distribution	3
1.3	T_{90} distribution	4
1.4	GRB SED example: GRB 130427A	7
1.5	GRB 980425/SN 1998bw	9
1.6	GRB afterglow synchrotron emission	12
1.7	Lyman- α forest dropout for $z \sim 8.2$ GRB	13
1.8	Distinguishing dust from Lyman- α dropout	14
1.9	Host galaxy metallicity example: GRB 130606A	15
1.10	Gunn-Peterson trough	17
2.1	Optical and NIR light curves of GRB 130702A	24
2.2	Host galaxy of GRB 130702A	29
2.3	Raw spectra of SN 2013dx	31
2.4	X-ray light curve of GRB 130702A	34
2.5	Corrected spectra of SN 2013dx	36
2.6	Optical light curves of SN 2013dx compared with SN 1998bw	38
2.7	Bolometric light curves of GRB-SNe	43
2.8	Comparison of SN 2013dx spectra with Type Ic and Type Ic-BL spectra	46
2.9	SYN++ fits of SN 2013dx spectra	50
2.10	Comparison of GRB-SN explosion parameters	56
2.11	E_K and M_{Ni} for SNe Ib, Ic, Ic-BL, IIP, and GRB-SNe	57
3.1	R-band distribution of GRB host galaxies	74
3.2	Cumulative redshift distribution of GRB-DLAs compared to TOUGH sample	75
3.3	Metallicity distribution of GRB-DLAs compared to double-DLA sample	76
3.4	SFR comparison for column density and redshift with GRB-DLA sample and double-DLA sample	83
3.5	Cartoon of GRB-DLA host localization differences for ideal and realistic cases	86
3.6	Dust corrected SFR surface densities vs. HI gas surface densities for GRB-DLA hosts	90

3.7	Comparison of GRB-DLA host SFR surface densities vs. HI gas surface densities to local and moderate redshift objects	91
3.8	GRB-DLA host enrichment times	95
4.1	DCT	105
4.2	RIMAS model	106
4.3	RIMAS model slit-viewer	107
4.4	RIMAS integration	108
4.5	RIMAS science detectors	109
4.6	RIMAS slit-viewer detector	110
4.7	Semiconductor lattice	111
4.8	PN junction	112
4.9	Hybrid array	113
4.10	MOSFET energy diagram	114
4.11	MOSFET example	115
4.12	Hybrid detector readout circuit diagram	116
4.13	Hybrid detector sampling modes	119
4.14	Leach/ARC hardware	121
4.15	cRIO hardware	123
4.16	Science detector characterization: conversion gain	129
4.17	Science detector characterization: linearity	131
4.18	Science detector characterization: read noise	133
4.19	Science detector characterization: dark current	134
4.20	Slit-viewer detector characterization: conversion gain	136
4.21	Slit-viewer detector characterization: linearity	137
4.22	Slit-viewer detector characterization: read noise	139
4.23	Detector diagnostics: raw frame	141
4.24	Detector diagnostics: unconnected frame	143
4.25	Detector diagnostics: detector degradation	144
4.26	Detector diagnostics: ramping ADC bias	145
4.27	Detector diagnostics: column splitting	146
5.1	Example of pipeline processed images	153
5.2	RIMAS photometric throughput	157
5.3	RIMAS low-resolution spectroscopy throughput	158
5.4	RIMAS high-resolution spectroscopy throughput	159
5.5	Example of RIMAS observing calculator	160
5.6	R-band host galaxy magnitude as a function of redshift	162
5.7	J-band cumulative distribution for three fields from DIRBE and 2MASS164	

List of Abbreviations

ADC	analog-to-digital converter
ADU	analog-to-digital unit
ARC	Astrocam Research Camera, Inc.
CCD	charge-coupled device
CDS	correlated double sampling
CMOS	complementary metal-oxide-semiconductor
cRIO	compact real-time input output
DCT	Discovery Channel Telescope
DLA	damped Lyman- α
DN	digital number
GRB	gamma-ray burst
H2RG or HAWAII-2RG	HgCdTe Astronomy Wide Area Infrared Imager with 2K x 2K Reference Pixels and Guide Mode
HgCdTe	Mercury Cadmium Telluride
IGM	intergalactic medium
InGaAs	Indium Gallium Arsenide
InSb	Indium Antimonide
ISM	interstellar medium
LED	light emitting diode
LMI	Large Monolithic Imager
Ly- α	Lyman- α
MOSFET	metal-oxide semiconductor field-effect transistor
NIR	near-infrared
RIMAS	Rapid infrared IMager-Spectrometer
ROIC	readout integrated circuits
QE	quantum efficiency
QSO	quasi-stellar object or quasar
SED	spectral energy distribution
SFR	star formation rate
Si	Silicon
Si:As	Arsenic doped Silicon
SN	supernova
SNR	signal-to-noise ratio
TTL	transistor-transistor logic
UTR	up-the-ramp sampling

Chapter 1: Introduction

1.1 Gamma-ray Bursts

Gamma-ray bursts (GRBs) are explosive transient events in the gamma-ray band that last $\lesssim 100$ seconds. GRBs have non-thermal spectra and light curves that can vary on the order of milliseconds. In this section we will outline a brief history of GRBs, the origin of these objects, and current detection methods.

1.1.1 Short History

The first GRB was detected by the Vela satellites in 1967. The Vela satellites were launched by the United States Air Force and were equipped with X-ray, neutron, and gamma-ray detectors to identify non-compliance of the Partial Nuclear Ban Treaty with the Soviet Union. Initially the GRB detections were shelved because the signal did not resemble the characteristic light curve shape of nuclear weapons. Klebesadel et al. (1973) examined 16 of these GRBs that had near simultaneous detections in two satellites indicating that these objects were not located in our solar system. Unfortunately these objects could not be localized precisely enough for follow-up observations.

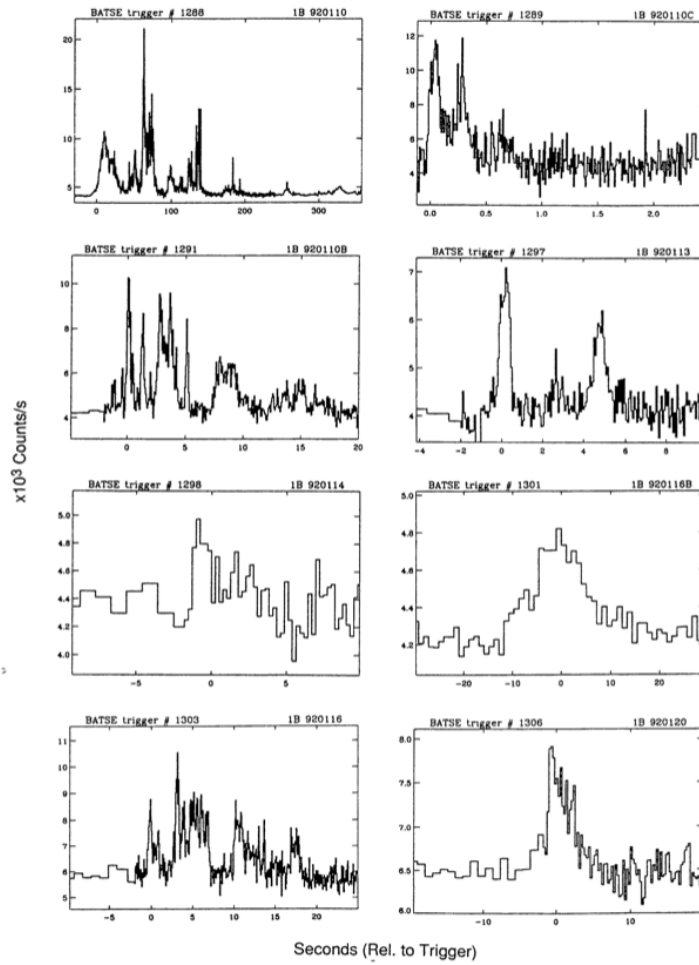


Figure 1.1 A small sample of GRB light curves from BATSE taken from Fishman & Meegan (1995). There is a large amount of variation between different bursts and there can be rapid variations within each burst.

2704 BATSE Gamma-Ray Bursts

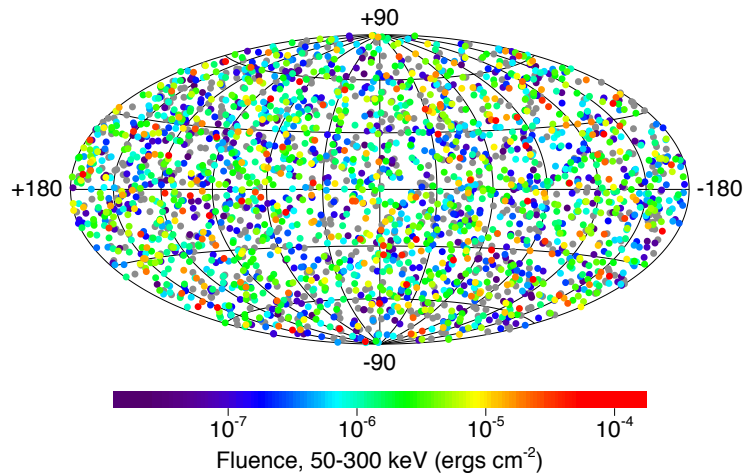


Figure 1.2 The location of GRBs detected by BATSE over the lifetime of the instrument. The isotropic distribution of the GRBs indicated that these objects were extragalactic in nature. Image retrieved from <http://gammaray.nsstc.nasa.gov/batse/grb/skymap/>.

Not much progress was made until the Compton Gamma Ray Observatory (CGRO) was launched in 1991. The CGRO carried the Burst and Transient Source Experiment (BATSE) on board which detected over 2700 GRBs over its nine year lifespan (Goldstein et al., 2013). This amounted to a detection rate of roughly one GRB per day. Figure 1.1 shows some example light curves from BATSE. The light curves show that, in general, GRBs last several seconds, but the bursts can vary drastically from one another. Figure 1.2 displays the location of each of the BATSE bursts on the sky. The isotropic nature of the BATSE GRBs indicated that these objects were extragalactic in nature (Meegan et al., 1992; Pendleton et al., 1994; Briggs et al., 1996).

The duration of a GRB is defined by a parameter called T_{90} which is the

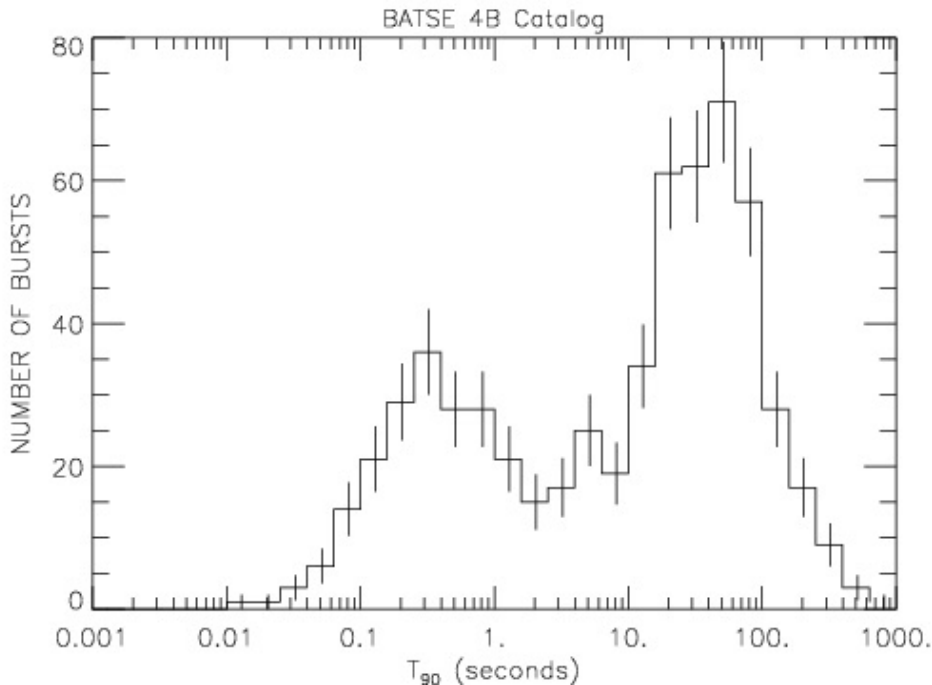


Figure 1.3 The BATSE T_{90} distribution indicated that there was a bimodal distribution of GRBs: long-duration with $T_{90} \gtrsim 2\text{s}$ and short-duration with $T_{90} \lesssim 2\text{s}$. Image retrieved from <http://f64.nsstc.nasa.gov/batse/grb/duration/>.

duration of time that the cumulative counts of the burst increase from 5% to 95% above the background and encompass 90% of the total GRB counts. BATSE data showed that GRBs fell into two classes (Figure 1.3): long-duration bursts where $T_{90} \gtrsim 2\text{s}$ and short-duration bursts where $T_{90} \lesssim 2\text{s}$ (Kouveliotou et al., 1993).

BATSE had a localization with uncertainties of several degrees which made it difficult to follow-up GRBs with other instruments. However, a major watershed event occurred in 1997 when BeppoSAX, an X-ray telescope, detected a fading X-ray source in its Wide-Field Camera (WFC) concurrent with a BeppoSax Gamma-Ray Burst Monitor (GRBM; Feroci et al., 1997) trigger. BeppoSAX was able to localize this burst, GRB 970228, to an error box of $6'$ (Costa et al., 1997). With the more precise localization, optical telescopes were able to follow-up and detect

a fading optical counterpart (van Paradijs et al., 1997; Wijers et al., 1997). This optical counterpart was associated with a faint galaxy and indicated that GRBs lie at cosmological distances. Later in 1997, observers were able to measure the first redshift of a GRB, GRB 970508, at $z = 0.835$ (Metzger et al., 1997).

In 2004, the launch of *Swift* (Gehrels et al., 2004) drastically changed the field of GRBs. *Swift* is outfitted with the Burst Alert Telescope (BAT; Barthelmy et al., 2005), a wide-field gamma-ray instrument that uses a coded aperture mask to locate the position of each burst to $\sim 3'$. *Swift* is also equipped with the X-ray Telescope (XRT; Burrows et al., 2005) and Ultraviolet/Optical Telescope (UVOT; Roming et al., 2005) which can localized GRBs to $\sim 3''$ and sub-arcseconds respectively. When a GRB trigger occurs in the BAT, *Swift* rapidly and autonomously slews the XRT and UVOT to better localize the burst. This has allowed other ground- and space-based facilities to quickly follow-up on these bursts to identify optical/radio counterparts and measure redshifts. *Swift* detects ~ 100 GRBs/year (Gehrels et al., 2009) and has allowed us to study GRBs and their host counterparts in detail. We discuss the specifics of detection methods in §1.1.5, but first we explore the origin of these bursts.

1.1.2 What Are Gamma-Ray Bursts?

GRBs are some of the most explosive events in the Universe. As the name suggests, these are bright bursts in the gamma-ray band. They have isotropic gamma-ray energies of $E_{\gamma,\text{iso}} = 10^{48} - 10^{54}$ erg and last mere seconds. However, GRBs can

have a wide variety of behavior as shown in Figure 1.1. In fact, some GRB light curves show rapid variations on the order of milliseconds. This suggests that the emitting regions are fairly compact ($c\delta t \lesssim 3 \times 10^7$ cm) if they are not relativistically expanding.

Spectral energy distributions (SEDs) of GRBs show that these objects have non-thermal spectra and emit at >1 MeV in the rest-frame. These energies are above the rest energy of an electron-positron pair and if GRBs originate from compact emitting regions, we would expect that these objects to be opaque to pair production and produce a thermal spectrum. This inconsistency is called the “compactness problem” and is resolved if the emitting regions are relativistically expanding with a Lorentz factor of $\Gamma = \frac{1}{\sqrt{1-v^2/c^2}}$. Relativistic expansion increases the radius of the emitting region, $r \sim \Gamma^2 c\delta t$, and decreases the opacity (Piran, 2004):

$$\tau_{\gamma-\gamma} \propto FD^2 r^{-2} \propto FD^2 \Gamma^{-(2\alpha+2)} c\delta t \quad (1.1)$$

where F is the fluence, D is the distance to the object, and α is the high-energy spectral index. In order for the emitting region to be optically thin ($\tau_{\gamma-\gamma} \lesssim 1$), the Lorentz factor must be large ($\Gamma \gtrsim 100$) which means that GRBs must have ultrarelativistic ejecta (ex. Lithwick & Sari, 2001). We expect that relativistic ejecta will have relativistic beaming effects which means that GRBs are collimated.

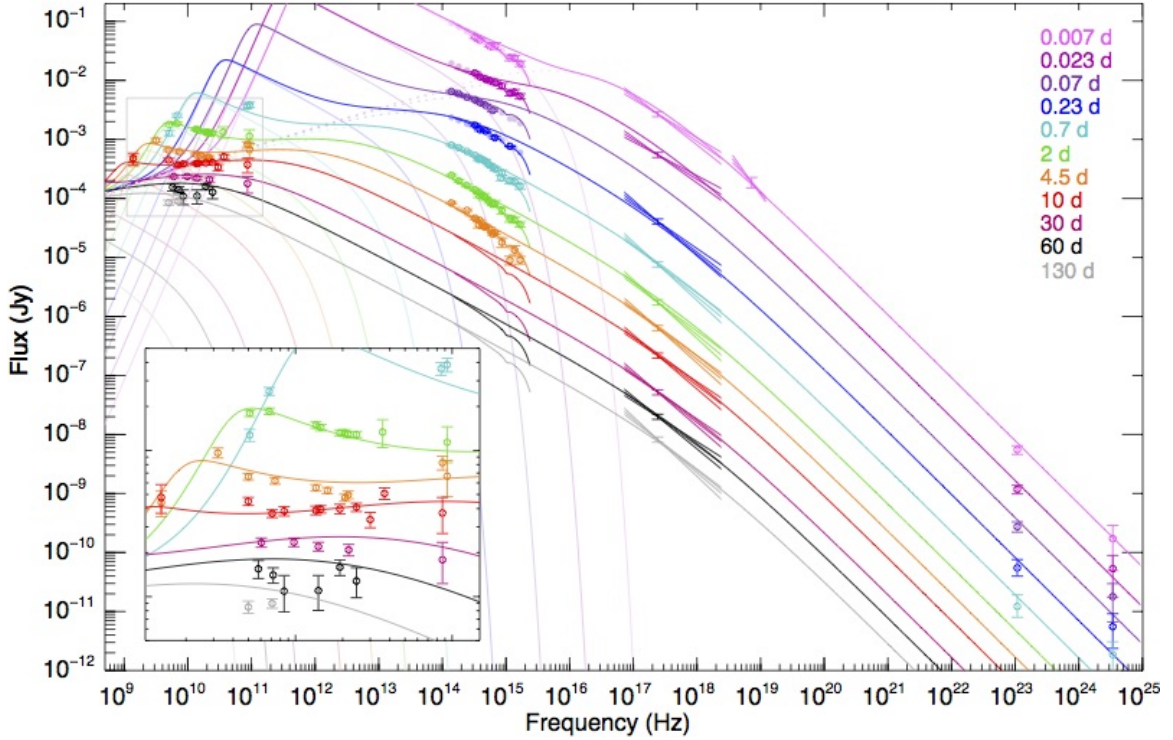


Figure 1.4 An example of a GRB SED for GRB 130427A across 16 orders of magnitude in frequency and 130 days of observations taken from Perley et al. (2014).

1.1.3 Gamma-ray Burst Models

The leading GRB model is the “fireball” model where an optically thick and compact inner engine ejects a relativistic energy flow (Piran, 1999, and references within). The optically thick jet expands and cools to eventually become optically thin. In this model, collisions between shock waves within the jet traveling at different speeds convert kinetic energy into gamma-ray photons through either Inverse Compton scattering or synchrotron emission. These gamma-ray photons are created after the jet becomes transparent and create GRBs. However, internal shocks are inefficient at removing energy from the outflow because the relative velocities between shells of relativistic material is small.

The jet still maintains a lot of energy when it interacts with the interstellar medium (ISM) and the kinetic energy from the jet shock-heats the ISM. These accelerated electrons emit synchrotron radiation when they interact with local magnetic fields creating a GRB afterglow that emits across the entire electromagnetic spectrum (ex. Figure 1.4). The energy emitted in the GRB afterglow is roughly the same amount of energy emitted in the GRB, $E_{\gamma,\text{iso}} \sim 10^{48-54}$ erg, and can last between days and weeks in the optical and up to years in the radio.

This jet model is supported by GRB afterglow observations that have a jet break at late times (Racusin et al., 2009) as well as late time ejecta velocity measurements from radio observations (ex. Figure 2 in Margutti et al., 2014a). This suggests that not only are GRBs collimated, ultrarelativistic material, they also come from jets and are not emitted isotropically. Therefore, observational evidence points to GRBs being formed from highly collimated and ultrarelativistic jets.

1.1.3.1 Gamma-ray Burst Progenitors

Any proposed GRB central engine must have very large angular momentum to create these collimated and ultrarelativistic jets. The leading models use two different types of central engines to explain what powers the jet: an accreting black hole (MacFadyen & Woosley, 1999; Woosley, 1993; Giacomazzo et al., 2013) or a rapidly spinning neutron star with large magnetic fields (Usov, 1992). The GRB central engines are believed to be formed through different channels for long and short GRBs.

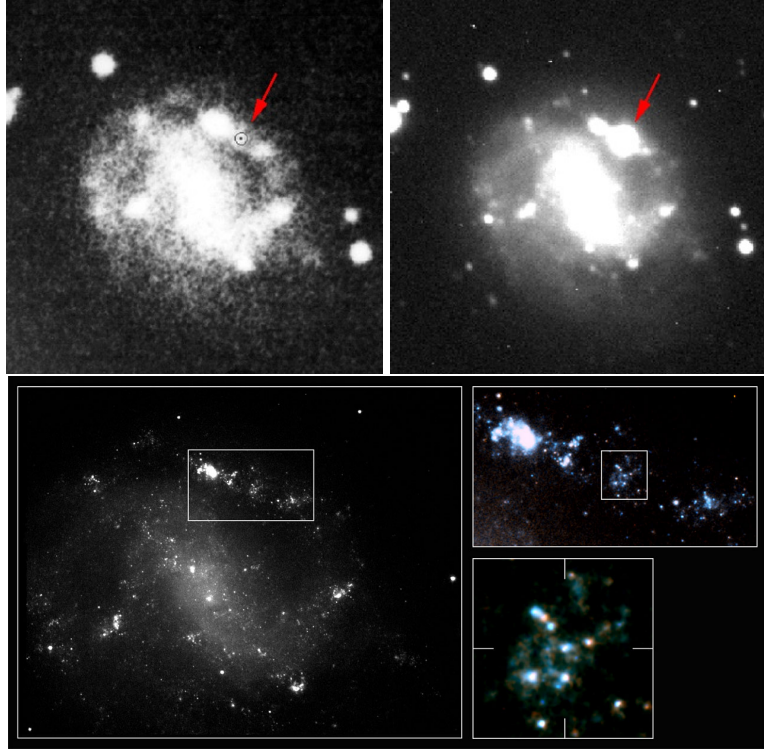


Figure 1.5 Host galaxy of GRB 980425 from archival images (upper left) and images taken shortly after SN 1998bw (upper right). Late follow-up zoomed in *Hubble Space Telescope* images are shown in the bottom panel. The GRB-SN occurred in a blue, star forming region of the spiral arm of the host galaxy. Images taken from Hjorth & Bloom (2012).

Long GRBs are associated with the explosion of massive stars. While there was observational evidence that placed long GRBs in bluer galaxies with higher star formation rates (Woosley & Bloom, 2006, and references within), the conclusive evidence came with SN 1998bw. This supernova (SN) was both spatially and temporally coincident with GRB 980425 (Figure 1.5; Galama et al., 1998; Iwamoto et al., 1998; Kulkarni et al., 1998). Since then, multiple SNe have been associated with nearby GRBs (see Table 2.1). All of these GRB-SNe are Type Ic-BL SNe which have no hydrogen in their spectra, but have helium and are marked by their incredibly broadened lines with velocities of $\gtrsim 10,000$ km/s.

The leading short GRB progenitor model is either a neutron star-neutron star (NS-NS) merger or a neutron star-black hole (NS-BH) merger (Eichler et al., 1989; Narayan et al., 1992). This is supported by observational evidence that short GRBs tend to be located at large radial offsets from their host galaxies and a mixture of early-type and star-forming galaxies (Berger, 2014, and references within). The strongest evidence comes from GRB 130603B which displayed an infrared excess consistent with a “kilonova” (Tanvir et al., 2013) which is an explosion that is fainter than a supernova but creates r-process elements created during a NS-NS or NS-BH merger. The real smoking gun would be a gravitational wave detection coincident both temporally and spatially with a short GRB.

1.1.4 Gamma-ray Burst Afterglow Model

The GRB afterglow can be observed from seconds up to years after the initial GRB trigger depending on the bandpass. The characteristic afterglow synchrotron spectrum (Figure 1.6) is described by a four-part broken power law separated by ν_a , ν_m , and ν_c (Sari et al., 1998). ν_a is the synchrotron self-absorption frequency, ν_m is the frequency associated with the minimum energy imparted to an electron when it crosses the shock wave, and ν_c is associated with the cooling rate of electrons. Frequencies above ν_c can easily cool and radiate energy away, therefore when $\nu_c < \nu_m$ the afterglow undergoes fast cooling and when $\nu_c > \nu_m$ the afterglow undergoes slow cooling. Sari et al. (1998) shows that $\nu_c \propto t^{-0.5}$ and $\nu_m \propto t^{-1.5}$ for adiabatic evolution or $\nu_c \propto t^{-2/7}$ and $\nu_m \propto t^{-12/5}$ for radiative evolution so at late times

the afterglow undergoes slow cooling and the peak of the afterglow moves towards longer wavelengths. ν_a , ν_c , ν_m , and the flux of ν_m can be expressed in terms of blast wave properties and therefore we can determine blast wave properties when we have a full SED model for the GRB afterglow (Wijers & Galama, 1999). This requires a coordinated multiwavelength observation effort.

1.1.5 Detection Methods

The majority of GRBs are detected using gamma-ray instruments on either *Swift* with the BAT or the Fermi satellite with the Gamma-ray Burst Monitor (GBM; Meegan et al., 2009) or the Large Area Telescope (LAT; Atwood et al., 2009). The instruments are complementary: the BAT covers the lower energy range of 15-150 keV, the GBM covers the lower and middle energy range of 8 keV-40 MeV, and the LAT covers a much higher energy range of 20 MeV-300 GeV. However, the GBM and the LAT can only localize to a few degrees so *Swift* works in conjunction with Fermi to localize GRBs. The GRB detections are disseminated through the GRB Coordinates Network (GCN; Barthelmy et al., 1998) through circular notices which allow observers to coordinate follow-up observations of the GRB afterglow. Observers initially use GCNs to disseminate information about the GRB trigger time, GRB location, and GRB energy.

Optical observatories typically measure the redshift of the GRB once the GRB is well localized. The redshift can be measured by identifying either metal or hydrogen spectral emission lines or absorption lines from the host galaxy using the GRB

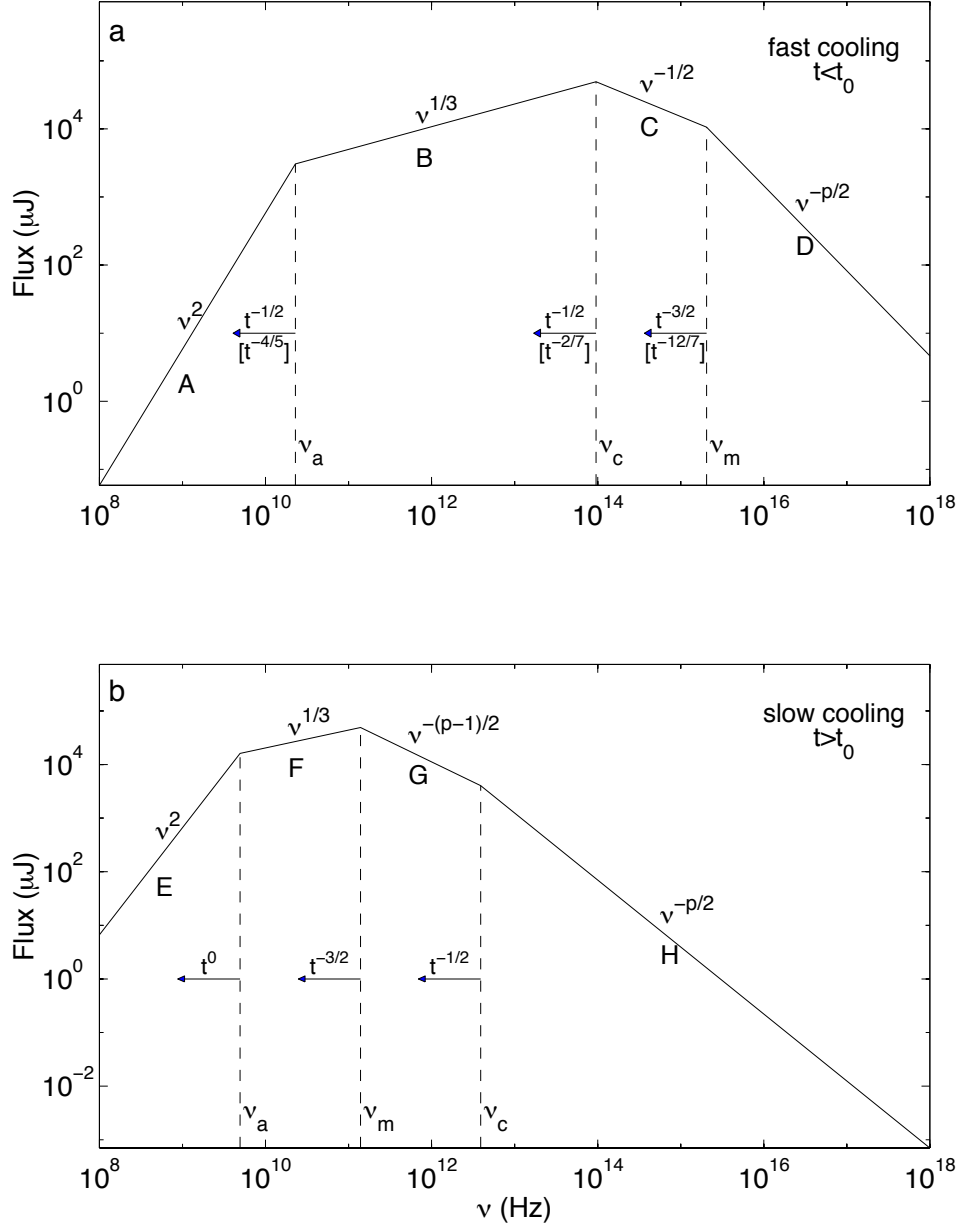


Figure 1.6 Synchrotron emission models for GRB afterglows taken from Sari et al. (1998). The top panel shows the case where the frequency associated with the minimum energy imparted to an electron when it crosses the shock wave (ν_m) is larger than the cooling frequency (ν_c) which is called fast cooling. The bottom panel shows the case where $\nu_c > \nu_m$ and the GRB afterglow undergoes slow cooling. The frequencies that separate the four-part broken power law change as function of time.

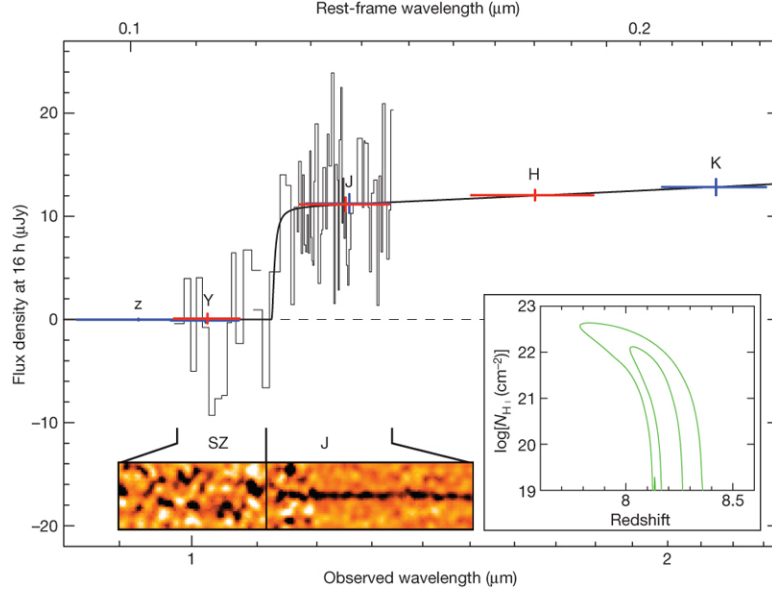


Figure 1.7 Photometry (red and blue errorbars) and low-resolution spectrum (black) of GRB 090423, the most distant spectroscopically confirmed GRB, at $z \sim 8.2$ from Tanvir et al. (2009). The GRB flux density drops off sharply at onset of neutral hydrogen clouds creating a well defined Ly- α edge starting at the first IGM absorber. The redshift of a burst can be determined from this Ly- α edge.

afterglow as a backlight. The GRB redshift can also be measured using photometry because as distant light travels from GRB afterglows through the host galaxy and intergalactic medium (IGM), neutral hydrogen creates a very distinct absorption feature: the Lyman- α (Ly- α) forest. This is created from a combination of the host galaxy and multiple cosmologically redshifted pockets of neutral hydrogen along the line of sight absorbing Ly- α photons. At higher redshifts the Ly- α absorption line is shifted to longer wavelengths. The spectrum drops out blue-ward of the first IGM absorber (Figure 1.7) creating the Ly- α forest edge. This drop-off is very evident in both photometry and spectroscopy and the drop-off's abrupt edge will be distinguishable from the more gradual dust extinction slope (Figure 1.8). For higher redshift bursts, the Ly- α forest is shifted into the near-infrared so the redshift is

determined with either near-infrared photometry or spectroscopy. GRBs have been discovered at $z \sim 8 - 9$ (Tanvir et al., 2009; Cucchiara et al., 2011).

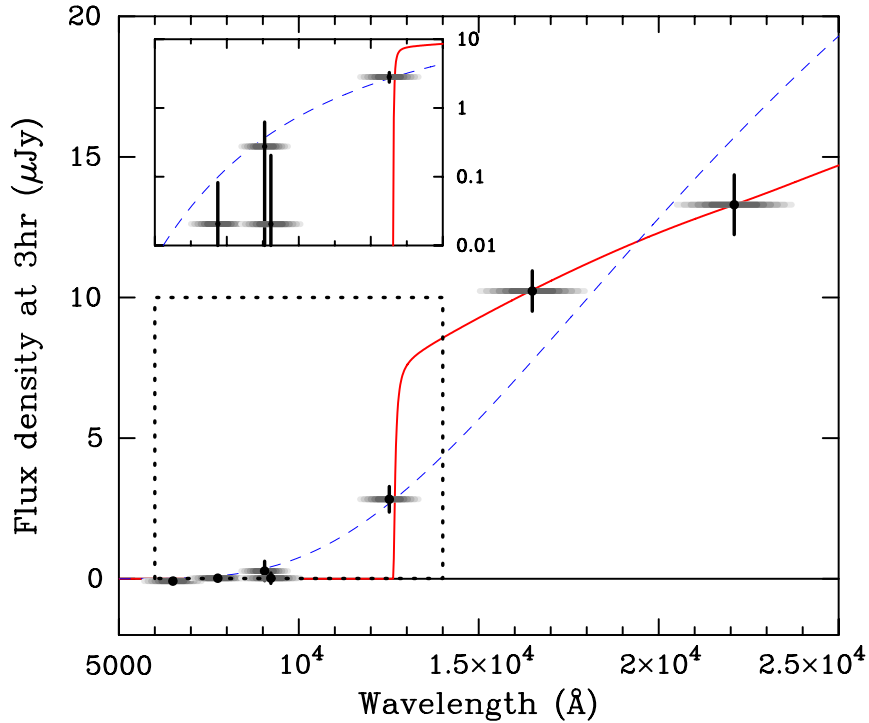


Figure 1.8 Photometry from GRB 090429B, the most distant imaged GRB, at $z \sim 9.4$ taken from Cucchiara et al. (2011). Two models are overlaid: (solid red) $z=9.36$ with rest-frame extinction $A_V=0.10$, (dashed blue) $z\sim 0$ with high-extinction $A_V=10.6$. The high-extinction model is ruled out due its low confidence level.

1.2 Gamma-ray Burst Host Galaxies

1.2.1 Galaxy Properties

GRB afterglows act as a bright backlight to study the intervening material between the GRB and us. In particular, GRB afterglows can be used to study the properties of the GRB host galaxies. The GRB afterglow flux, at a fixed time from the prompt emission, is nearly independent of its redshift (Ciardi & Loeb,

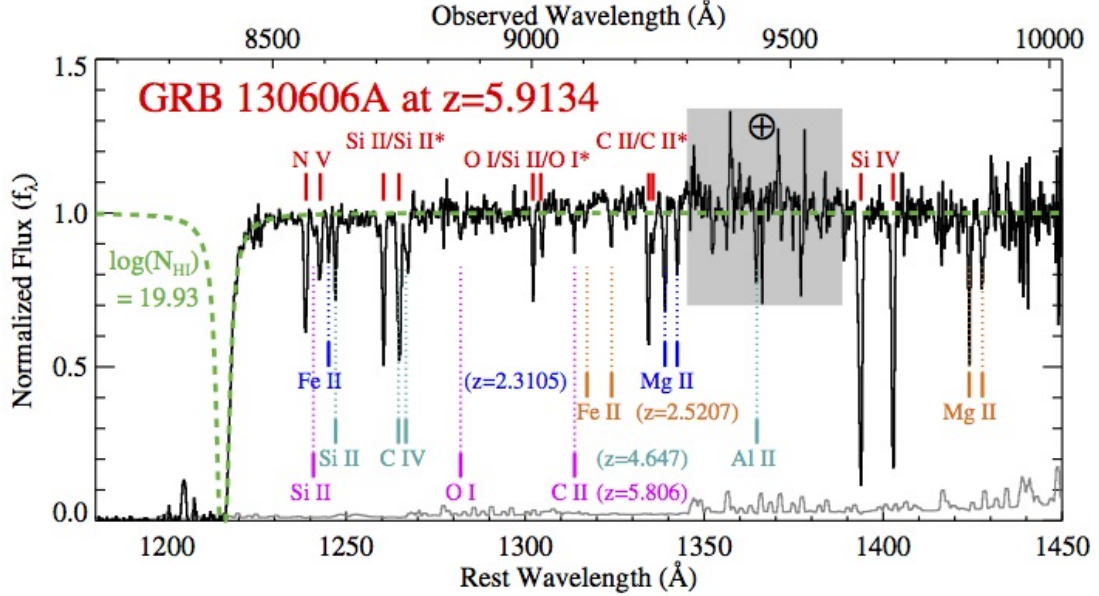


Figure 1.9 An example of absorption line identification from a GRB afterglow, GRB 130606A taken from Chornock et al. (2013). The metal lines at the same redshift of the burst are shown in red while metal lines for material along the line-of-sight are shown in blue, cyan, orange, and pink at $z \sim 2.3 - 5.8$. Also in green is a fit to the Ly- α line that gives a measurement of the atomic hydrogen column density.

2000); therefore GRB afterglows can be used to study high-redshift galaxies that may otherwise be too faint to detect from galaxy surveys. The GRB afterglow can be used to identify the redshift (discussed in §1.1.5) and host galaxy metallicities (e.g. Figure 1.9).

Due to the transient nature of GRBs, the host galaxies can be observed after the GRB afterglow has faded. Late-time observations of the host galaxy can be used to measure the star formation rates (SFRs) and SED models can be used to infer other galaxy properties like stellar mass and dust extinction (e.g. Savaglio et al., 2009; Perley et al., 2009, 2016a). GRBs have been spectroscopically observed at redshifts between $z = 0.0085$ (GRB 980425; Tinney et al., 1998) and $z = 8.2$ (GRB 090423; Tanvir et al., 2009) and therefore can be used to probe different galactic

environments throughout the observable Universe. However, observations of GRB host galaxies suggest that these galaxies may be biased towards low metallicity, low mass, and high SFR environments (Kocevski et al., 2009; Levesque et al., 2010; Wang & Dai, 2014).

1.2.2 Reionization

While at the present time the Universe is almost completely ionized, measurements of the Cosmic Microwave Background (CMB) have shown that recombination occurred at $z \sim 1100$ and analysis of Planck data indicate that reionization occurred at $z = 8.8_{-1.4}^{+1.7}$ (Planck Collaboration et al., 2016). Reionization occurs due to the formation of galaxies and stars in the Universe outputting radiation that ionize the surrounding environments; the Epoch of Reionization is a critical time to study the evolution of metallicity, star formation, and stellar masses.

Gunn & Peterson (1965) theorized that the presence of neutral hydrogen along a quasar line-of-sight would cause a trough in the quasar spectrum where the flux of the quasar almost drops to zero; this feature is called a Gunn-Peterson trough. SDSS 1030+0524 was the first object observed to have a Gunn-Peterson trough at $z = 6.28$, while other distant quasars at $z = 5.80$, $z = 5.82$, and $z = 5.99$ did not have Gunn-Peterson troughs (Figure 1.10; Becker et al., 2001). This indicates that reionization occurs at $z \sim 6 - 11$. While the initial Gunn-Peterson trough prediction was for quasar spectra, GRB afterglow spectra should also show the same effect at high redshifts.

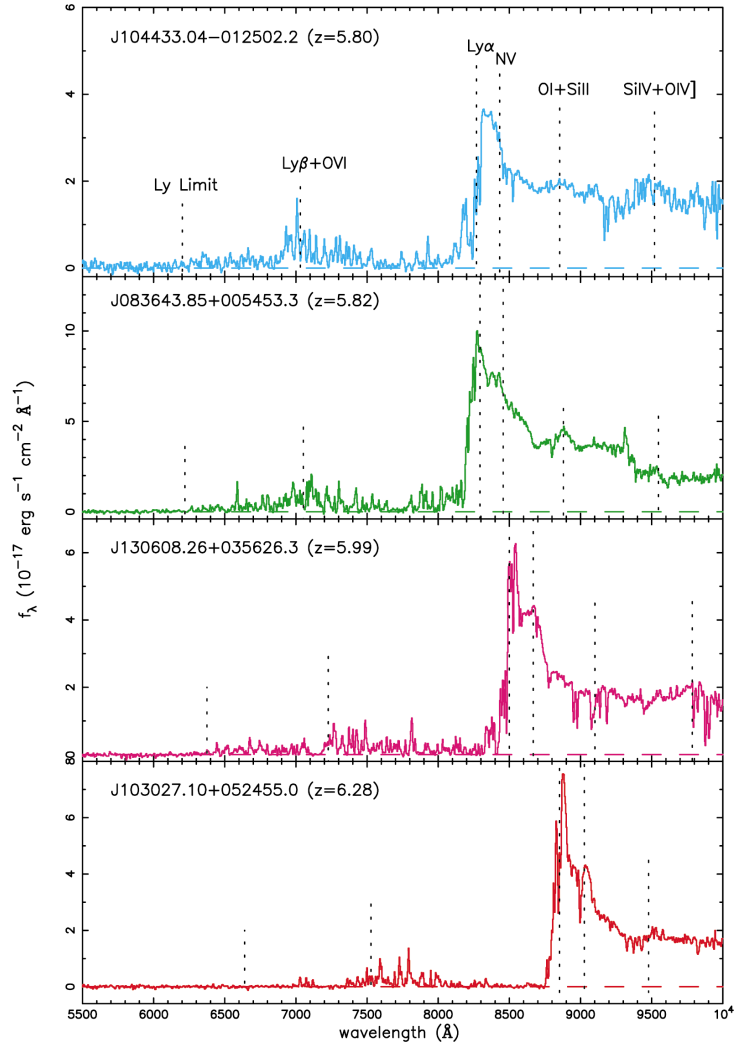


Figure 1.10 Four quasar spectra at $z \sim 5.5 - 6.5$ taken from Becker et al. (2001). The bottom panel is of SDSS 1030+0524 at $z = 6.28$ which is the first detection of the Gunn-Peterson trough. The flux in the trough goes to zero which indicates a large amount of neutral hydrogen. The top three panels do not have Gunn-Peterson troughs and indicate that the end of reionization is $z \sim 6$ for these lines-of-sight.

1.3 Outline of Thesis

1.3.1 Open Issues

This thesis sets out to explore the environments around GRBs. We look both locally, trying to understand how long GRB and SN properties are related, and on larger scales, examining the star formation properties of distant host galaxies with large column densities of atomic hydrogen identified by GRBs. A large component of this thesis is the development of a near-infrared (NIR) GRB afterglow follow-up instrument, the Rapid infrared IMager-Spectrograph (RIMAS). RIMAS's primary science motivation is to probe the environments of high redshift GRBs.

1.3.2 Organization

This thesis combines astronomical instrumentation with GRB afterglow science. RIMAS will be able to quickly follow-up high-redshift ($z \gtrsim 7$) GRB afterglows that cannot be observed with optical instruments due to the Ly- α forest. These bursts are of interest because they allow us to probe the environments of the early Universe and possibly study the very first stars and galaxies. More excitingly, we can potentially map reionization along multiple lines-of-sight using high-redshift GRB afterglows.

In this thesis we first explore a nearby GRB-SN (GRB 130702A/SN 2013dx) at $z = 0.145$ in chapter 2. Only nearby GRB-SNe can be studied in detail with photometry and spectroscopy and thus far there have only been 10 GRB-SNe, in-

cluding SN 2013dx, with extensive photometric and spectroscopic follow-up of the SNe. In this chapter we perform a detailed analysis of SN 2013dx: constructing a quasi-bolometric light curve of the SN and fitting SN parameters. We also compare SN 2013dx to other GRB-SNe and attempt to determine if SN parameters are correlated with GRB properties: a correlation between these properties would allow us to infer information about the SN at large distances where we can detect the GRB but not the SN.

RIMAS would prove useful in future GRB-SNe studies as the near-infrared makes up $\sim 15 - 30\%$ of the flux at late times and consequently excluding the NIR component can greatly affect SN parameters. Currently there is a dearth of NIR photometers and spectrographs on mid-sized telescopes like RIMAS.

Then, in chapter 3, we explore the host galaxy properties of Damped Lyman- α systems (DLAs) identified with GRBs. GRBs are extremely well suited for this purpose because (1) GRBs can be used as bright backlights to identify the DLA, (2) GRBs occur within the host galaxy associated with the DLA unlike other bright sources like quasars, and (3) GRBs are transient in nature which allows us to follow-up the host galaxy after the GRB afterglow has faded. We begin with a sample of DLAs identified by GRBs and analyze the host galaxy photometry of these objects. In particular, we examine the host galaxies' SFRs and star formation efficiencies. Our sample of GRB-DLA host galaxy detections triples the number of previously known DLA host galaxies.

Once RIMAS is commissioned, RIMAS would be able to add on to this study of GRB-DLA host galaxies. Additional NIR photometry would allow us to extend

to higher redshifts and allow more objects to be modeled by constraining SEDs to understand more about the host galaxy properties.

In chapter 4 we turn towards instrumentation and describe the RIMAS hardware. We go in depth on how RIMAS's NIR detectors operate and describe the RIMAS detector hardware. RIMAS will be very a precise photometer and spectrometer so we detail the RIMAS detector characterization. Our characterization includes dark current, read noise, saturation, conversion gain, and linearity measurements. Finally, we discuss general NIR detector troubleshooting methods at both room temperature and at cryogenic temperatures.

In chapter 5 we describe software products developed for RIMAS. We outline a quick reduce RIMAS pipeline that outputs a single result frame from a multiple frame acquisition. We then describe the development of a generalized photometry data reduction pipeline that can and has been used for multiple photometers. We also summarize our detailed instrument throughput models as well as our RIMAS observer calculators for limiting magnitudes and exposure times that use our throughput models. All of our software products are built with open-source software and are publicly available on GitHub that is packaged with detailed documentation.

Finally, in chapter 6, we summarize the results of this thesis work.

Chapter 2: GRB 130702A/SN 2013dx

2.1 Introduction

The evidence for the association between long-duration gamma-ray bursts (GRBs) and the death of massive stars has been steadily growing over the last two decades (see Woosley & Bloom 2006 and Hjorth & Bloom 2012 for reviews). The first direct evidence of this link was a spatially and temporally coincident supernova (SN), SN 1998bw, with GRB 980425 at redshift $z = 0.0085$ (Galama et al., 1998; Iwamoto et al., 1998; Kulkarni et al., 1998). Since SN 1998bw, there have been a number of spectroscopically confirmed supernovae (SNe) associated with GRBs (Table 2.1).

While most, if not all low- z long-duration GRBs appear to be accompanied by SNe (the exceptions being GRB 060614 and GRB 060505; Fynbo et al. 2006; Gal-Yam et al. 2006; Della Valle et al. 2006), only a small fraction of core-collapse explosions are capable of generating relativistic ejecta (Berger et al., 2003; Soderberg et al., 2010; Bietenholz et al., 2014). Even when limited to the specific subtype of SNe associated with GRBs, the broad-lined Type Ic SNe, those with and without relativistic ejecta appear to be indistinguishable based on their light curves (e.g., Drout et al. 2011). However, spectra of the host galaxies reveal that GRB-SNe pre-

Table 2.1. GRB-SN References

GRB-SN	References
GRB 980425/SN 1998bw	Galama et al. (1998); Iwamoto et al. (1998); Kulkarni et al. (1998)
GRB 030329/SN 2003dh	Stanek et al. (2003); Matheson et al. (2003)
GRB 031203/SN 2003lw	Malesani et al. (2004); Gal-Yam et al. (2004); Thomsen et al. (2004)
GRB 060218/SN 2006aj	Campana et al. (2006); Modjaz et al. (2006); Mirabal et al. (2006); Ferrero et al. (2006) Sollerman et al. (2006); Pian et al. (2006); Kocevski et al. (2007)
GRB 091127/SN 2009nzb	Cobb et al. (2010); Berger et al. (2011)
GRB 100316D/SN 2010bh	Starling et al. (2011); Bufano et al. (2012); Olivares E. et al. (2012) Cano et al. (2011); Chornock et al. (2010)
GRB 120422A/SN 2012bz	Melandri et al. (2012); Schulze et al. (2014)
GRB 130427A/SN 2013cq	Xu et al. (2013); Levan et al. (2014); Melandri et al. (2014); Perley et al. (2014)
GRB 130702A/SN 2013dx	This work; D’Elia et al. (2015)
GRB 140606B/iPTF14bfu	Cano et al. (2015)

Note. — We do not include the recent detection of GRB 111209A/SN 2011kl associated with a superluminous SN (Greiner et al., 2015a) because it is believed to be powered by a magnetar and not solely powered by ^{56}Ni .

fer more metal-poor environments than Type Ic-BL SNe without associated GRBs (Modjaz et al., 2008; Graham & Fruchter, 2013).

Furthermore, within the GRB population, there is a considerable diversity in the observed prompt gamma-ray energies spanning six orders of magnitude, $E_{\gamma,\text{iso}} = 10^{48}\text{--}10^{54}$ erg. It has been suggested that low-luminosity GRBs ($E_{\gamma,\text{iso}} \lesssim 10^{49}$ erg) have “failed” jets that cannot pierce their stellar envelope and instead dissipate energy into the star to create relativistic shock breakout (Bromberg et al., 2011; Margutti et al., 2014b; Nakar, 2015). But despite their very different appearance at high energies, as of yet there is no clear distinction between SNe associated with low-luminosity GRBs (e.g., SN 1998bw) and the larger (observed) cosmological population (e.g., SN 2003dh, SN 2013cq).

With still only a handful of well-observed examples, each new nearby GRB affords a unique opportunity to understand the *central engine* powering these outflows. In particular, we can probe the progenitor from two different angles by studying the

SN simultaneously with the GRB. Here we present observations of SN 2013dx associated with GRB 130702A. At $z = 0.145$, SN 2013dx is sufficiently nearby to enable a detailed photometric and spectroscopic study of the SN evolution. Furthermore, with $E_{\gamma,\text{iso}} = 6.4 \times 10^{50}$ erg (for 1 keV to 10 MeV in the rest frame), the prompt-emission properties place GRB 130702A between most low-luminosity GRBs and the more energetic cosmological population.

Throughout this paper we use the convention $F_{\nu}(t) \propto \nu^{-\beta} t^{-\alpha}$ and photon index $\Gamma = \beta + 1$. We assume a Λ CDM model with $H_0 = 69.6 \text{ km s}^{-1} \text{ Mpc}^{-1}$, $\Omega_m = 0.286$, and $\Omega_{\Lambda} = 0.714$ (Bennett et al. 2014). All photometry is in the AB system (Oke & Gunn, 1983), and quoted uncertainties are 1σ (68%) confidence intervals unless otherwise noted. Dates and times are UT in all cases.

2.2 GRB 130702A/SN 2013dx

GRB 130702A was detected by the Gamma-Ray Burst Monitor (GBM; Meegan et al. 2009) on the *Fermi* satellite at 00:05:23.079 on 2013 July 2 (Collazzi & Connaughton, 2013). As observed by the GBM, the prompt-emission duration¹ was $T_{90} \approx 59$ s (50–300 keV). High-energy emission was also detected by the *Fermi* Large Area Telescope (LAT; Atwood et al. 2009; Cheung et al. 2013), as well as by Konus-Wind (Golenetskii et al., 2013). We adopted the Konus-Wind 20–1200 keV fluence of $f_{\gamma} = (6.7 \pm 0.8) \times 10^{-6} \text{ erg cm}^{-2}$ (assuming a power-law spectrum with photon index $\Gamma = 1.87 \pm 0.11$).

¹ T_{90} is defined as the time over which a burst emits from 5% of its total measured counts to 95%.

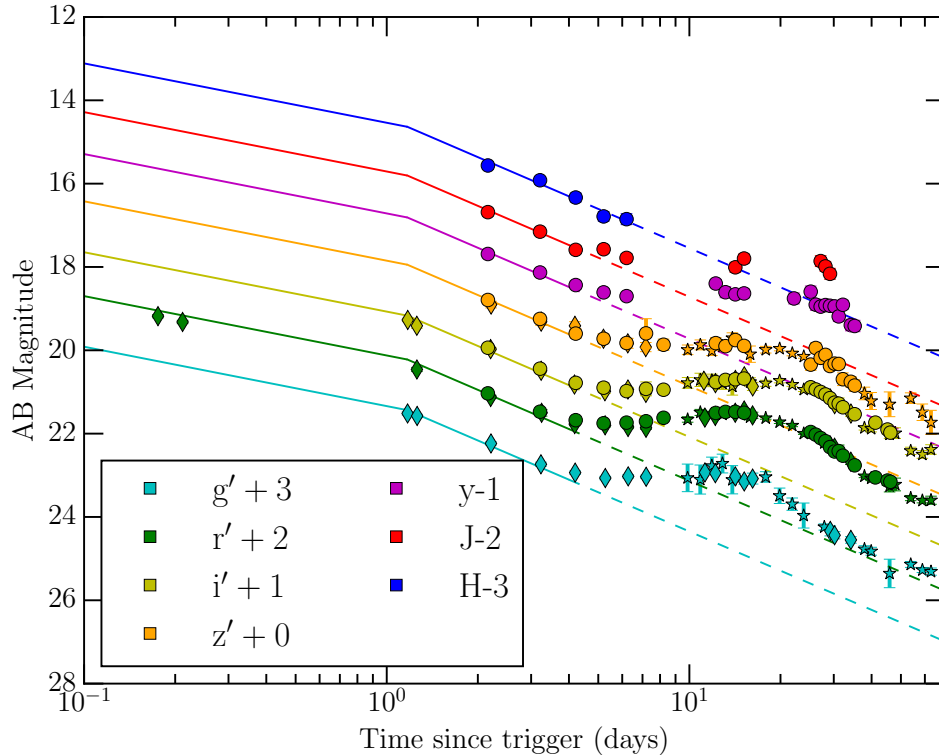


Figure 2.1 Optical and NIR light curves of GRB 130702A, corrected for Galactic extinction and host extinction (assuming $A_{V,\text{host}} = 0.10$ mag). Note that the host-galaxy contribution is not removed. Diamonds are P48/P60 data, circles are RATIR data, and stars are Liverpool data; error bars are overplotted on all datapoints. Solid lines indicate power-law fits with $\alpha_1 = 0.57$ and $t_b = 1.17$ d taken from Singer et al. (2013a) and $\alpha_2 = 1.25$ from the XRT power-law decay index. Dashed lines mark the extrapolated power law where we assume α_2 for all times beyond t_b .

Employing the wide-field imaging and rapid transient identification capabilities of the Intermediate Palomar Transient Factory (iPTF; Law et al. 2009; Rau et al. 2009), Singer et al. (2013b) discovered the optical afterglow of GRB 130702A. The source, also referred to as iPTF13bxl, is located at (J2000.0) coordinates $\alpha = 14^{\text{h}}29^{\text{m}}14^{\text{s}}.78$, $\delta = +15^{\circ}46'26''4$.

Subsequently, the redshift of GRB 130702A was determined to be $z = 0.145$ based on the detection of narrow host-galaxy emission lines ([O III] and $\text{H}\alpha$) at the afterglow location (Mulchaey et al., 2013b,a; D’Avanzo et al., 2013). Several other

galaxies at or near this redshift located in the field indicate that GRB 130702A occurred in a group or cluster environment, which is highly unusual for a GRB (Kelly et al., 2013; D’Elia et al., 2015). The GRB host galaxy may be a metal-poor satellite of an adjacent massive spiral (SDSSJ142914.57+154619.3), which has an offset of only ~ 19 kpc in projected distance and < 60 km s $^{-1}$ in line-of-sight velocity (Kelly et al., 2013).

At $z = 0.145$, the observed Konus-Wind fluence corresponds to an isotropic energy release of $E_{\gamma,\text{iso}} = 6.4_{-1.0}^{+1.3} \times 10^{50}$ erg (1 keV to 10 MeV in the rest frame). This places GRB 130702A securely between the low-luminosity class of events represented by GRB 980425 / SN 1998bw and typical cosmologically distant events with $E_{\gamma,\text{iso}} \gtrsim 10^{52}$ erg.

Butler et al. (2013) reported a flattening of the optical afterglow 5.26 d after the burst. A spectrum taken ~ 6 d after the burst showed broad features resembling those of SN 1998bw (Schulze et al., 2013). Cenko et al. (2013) and D’Elia et al. (2013) obtained spectra that confirmed the presence of an emerging SN, dubbed SN 2013dx, and identified similarities with SN 1998bw and SN 2006aj. D’Elia et al. (2015) (hereafter D15) reported GRB 130702A/SN 2013dx light curve, spectra, and SN energetics properties with which we will compare throughout this paper.

Table 2.2. Log of Spectroscopic Observations

Δt (d)	Instrument	Exposure (s)	Wavelength Range (nm)	Slit ($''$)	Grating/Grism	Airmass
1.17	DBSP	1800	340–1000	1.0	1200/5000 + 1200/7100	1.06
3.25	DBSP	1800	340–1000	1.0	600/4000 + 316/7500	1.36
6.22	DBSP	1800	340–890	2.0	600/4000 + 600/10000	1.25
9.33	DEIMOS	600	450–950	1.0	600/7500	1.19
11.34	DEIMOS	600	490–1010	1.0	600/7500	1.32
14.21	DBSP	1200	350–1000	1.5	600/4000 + 316/7500	1.27
31.28	DEIMOS	900	450–950	1.0	600/7500	1.30
33.27	LRIS	1200	330–1020	1.0	400/3400 + 400/8500	1.30
330.39	LRIS	1460	330–1020	1.0	400/3400 + 400/8500	1.04

Note. — Δt is the time from *Fermi* trigger in observer frame.

2.3 Observations and Data Reduction

2.3.1 Optical/Near-Infrared Imaging

We obtained optical and near-infrared (NIR) images of the location of GRB 130702A / SN 2013dx with the robotic Palomar 60 inch telescope (P60; Cenko et al. 2006), the 2 m Liverpool Telescope (LT; Steele et al. 2004), the Reionization and Transients Infrared/Optical camera on the 1.5 m Harold L. Johnson Telescope (RATIR; Butler et al. 2012; Watson et al. 2012), the Large Monolithic Imager on the 4.2 m Discovery Channel Telescope (LMI/DCT), and the Low Resolution Imaging Spectrometer (LRIS; Oke et al. 1995) on the 10 m Keck-I telescope. Additionally, we included early-time Palomar 48-inch r' observations (0.17 d and 0.21 d after the GRB trigger) from Singer et al. (2013a). The reduction procedures for each individual facility are described below, while the resulting photometry is presented in Table 2.7 and plotted in Figure 2.1. Photometry from different telescopes is calibrated to same

stars for uniform calibration. After removing extinction, afterglow, and host galaxy (see §2.4.1), the cross-calibration errors are $\sim 0.03\text{--}0.05$ mag (approximately 3–5% in flux).

2.3.1.1 P60 Photometry

P60 observed the location of GRB 130702A in the g' , r' , i' , and z' filters beginning 1.17 d after the *Fermi* GBM trigger. Basic CCD reductions are provided in real time by a custom IRAF²/PyRAF³ pipeline. At later times ($\Delta t \gtrsim 3$ d), images were stacked with SWarp (Bertin et al., 2002) on a nightly basis to increase the signal-to-noise ratio (SNR). We performed aperture photometry at the afterglow location, calibrating with respect to nearby point sources from the Sloan Digital Sky Survey (SDSS; Aihara et al. 2011).

2.3.1.2 LT Photometry

LT began observing the location of GRB 130702A with the IO:O CCD camera 9.87 d after the GBM trigger. Observations were obtained in the g' , r' , i' , and z' filters. Standard reduction techniques were applied to detrend the data, and photometry was performed in the same manner as for the P60 images (including the same SDSS reference stars for photometric calibration).

²IRAF is distributed by the National Optical Astronomy Observatory, which is operated by the Association of Universities for Research in Astronomy (AURA), Inc. under cooperative agreement with the National Science Foundation (NSF).

³See http://www.stsci.edu/institute/software_hardware/pyraf.

2.3.1.3 RATIR Photometry

RATIR obtained simultaneous multi-color ($r'i'z'yJH$) imaging of the location of GRB 130702A beginning 2.16 d after the GBM trigger. The RATIR data were reduced using an automatic python pipeline with bias subtraction and twilight-sky flat fielding. Given the lack of a cold shutter in RATIR's design, IR dark frames were not available. Laboratory testing, however, confirmed that the dark current is negligible in both IR detectors (Fox et al., 2012). Astrometric solutions were calculated from `astrometry.net` (Lang et al., 2010) and the individual frames are stacked using `SWarp`.

We performed aperture photometry on the resulting stacked images using `SExtractor` (Bertin & Arnouts, 1996) with an inclusion radius determined from the median full width at half-maximum intensity (FWHM) of the images. The resulting instrumental magnitudes were compared to SDSS in the optical and 2MASS (Skrutskie et al., 2006) in the NIR to calculate zeropoints. For the y band, we created a spectral energy distribution (SED) from the combination of optical and NIR catalog sources and interpolated to the appropriate wavelength. To place all photometry on the AB system, we used the J - and H -band offsets from Blanton & Roweis (2007).

2.3.1.4 Keck/LRIS Photometry

The location of GRB 130702A was observed with Keck/LRIS on 2014 May 28 ($\Delta t = 330$ d) in the u' , g' , and R -band filters. The resulting images were reduced

using the LPipe package⁴. Because the host galaxy was clearly resolved in some of the better-seeing images (FWHM = 0''75), we adopted an aperture radius of 1''5 to incorporate all of the flux from the visible extent of the galaxy (Figure 2.2). Photometric calibration was performed relative to point sources from SDSS.

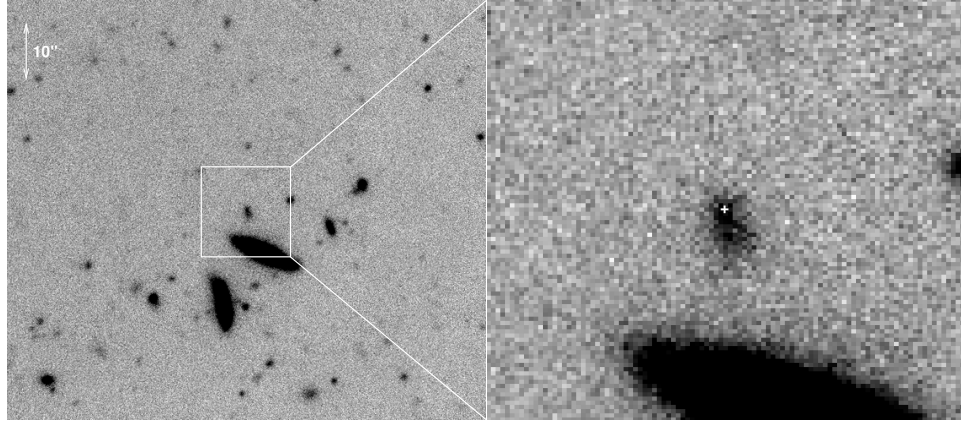


Figure 2.2 Keck/LRIS g' -band image of the host galaxy of GRB 130702A, obtained at $\Delta t = 330.48$ d after the GBM trigger (i.e., when the afterglow and SN emission had faded away). The location of the transient is displayed in the inset with the white cross. The dwarf host is clearly elongated in the N-S direction, with the bulk of the star formation (as evidenced by the transient location and the nebular emission lines) apparent in the northern component. The image is oriented with N up and E to the left.

2.3.1.5 Keck/MOSFIRE Photometry

We imaged the location of GRB 130702A with the Multi-Object Spectrometer For InfraRed Exploration (MOSFIRE; McLean et al. 2012) on the 10 m Keck I telescope on 2014 June 16. Images were obtained in the J and K_s filters and reduced using custom IDL scripts. We performed aperture photometry using a 1''5 inclusion radius (see §2.3.1.4), with photometric calibration relative to 2MASS.

⁴See <http://www.astro.caltech.edu/~dperley/programs/lpipe.html> for details.

2.3.1.6 LMI/DCT Photometry

The location of GRB 130702A was observed with LMI/DCT on 2015 March 27 ($\Delta t = 633$ d) in the g' , r' , i' , and z' filters. The resulting images were detrended with a custom IRAF pipeline. Individual frames were astrometrically aligned with *Scamp* (Bertin, 2006) and coadded using *SWarp*. Photometry was calculated in the manner described in §2.3.1.3.

2.3.2 Optical Spectroscopy

We obtained a series of optical spectra of GRB 130702A, beginning at $\Delta t = 1.17$ d after the *Fermi*-GBM trigger, with the Double Spectrograph (DBSP; Oke & Gunn 1982) on the 5 m Palomar Hale telescope, Keck/LRIS on Keck-I, and the DEep Imaging Multi-Object Spectrograph (DEIMOS; Faber et al. 2003) on the 10 m Keck-II telescope. An observing log is presented in Table 2.2. All spectra were obtained with the slit oriented at the parallactic angle to minimize differential losses due to atmospheric dispersion (Filippenko 1982; though note also that LRIS employs an Atmospheric Dispersion Corrector to further mitigate against differential slit losses). The resulting reduced one-dimensional spectra are displayed in Figure 2.3.

All spectra were reduced using standard routines and optimally extracted (Horne, 1986) within the IRAF environment (see, e.g., Cenko et al. 2008 for details). A dispersion solution was computed using calibration spectra of comparison lamps, and then adjusted for each individual exposure using night-sky emission lines. For the LRIS and DEIMOS spectra, sky background emission was subtracted using

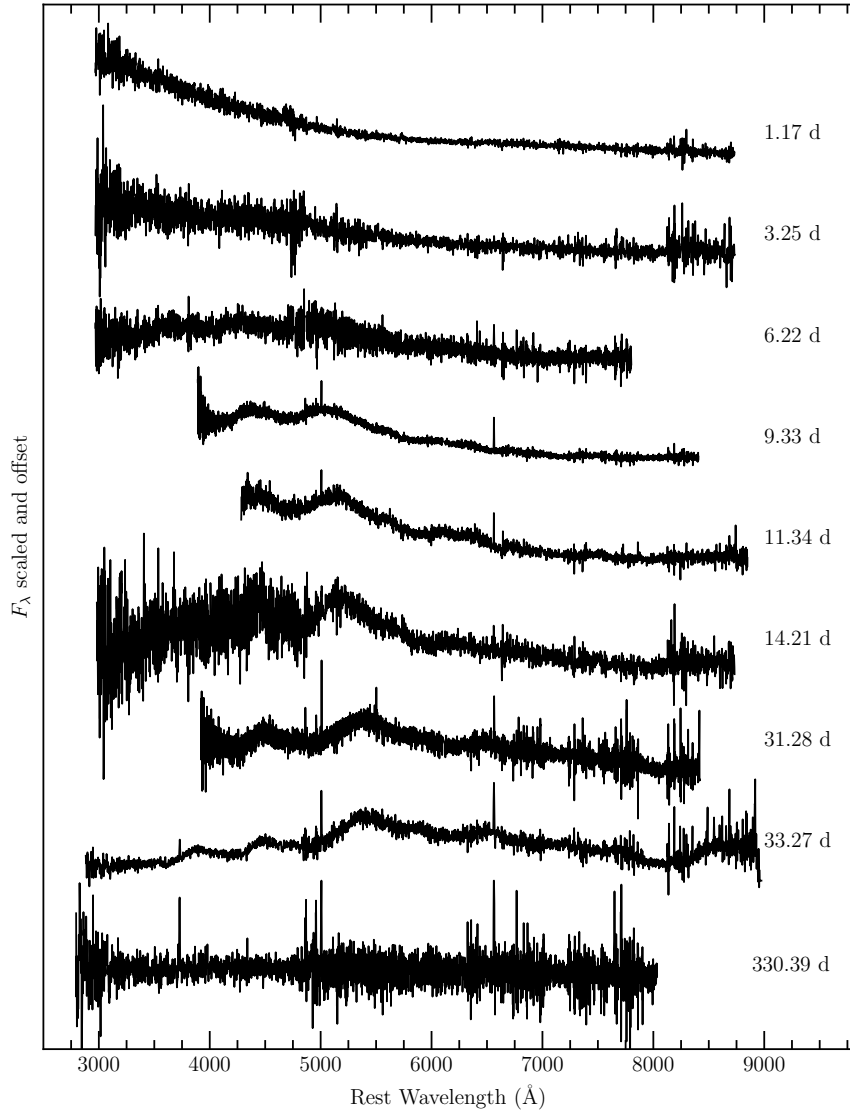


Figure 2.3 Spectra uncorrected for slit losses, extinction, afterglow, or host-galaxy contamination. Early-time spectra are dominated by the afterglow component. The broad features associated with SN 2013dx become visible after about a week.

the algorithm described by Kelson (2003). Telluric atmospheric absorption features were removed using the continuum from spectrophotometric standard stars (Wade & Horne, 1988; Matheson et al., 2000). Finally, a sensitivity function was applied using observations of spectrophotometric standards at a comparable airmass. We caution that the final Keck/LRIS spectrum obtained at $\Delta t = 330.39$ suffered from a failure of the blue shutter, which may impact the relative-flux calibration.

Upon publication of this manuscript, all one-dimensional spectra will be made publicly available via the Weizmann Interactive Supernova data REPOSITORY (WISEREP; Yaron & Gal-Yam 2012).

2.3.3 X-Ray Observations

The afterglow of GRB 130702A was observed by the X-Ray Telescope (XRT; Burrows et al. 2005) onboard the *Swift* satellite (Gehrels et al., 2004) beginning at $\Delta t = 1.03$ d after the *Fermi*-GBM trigger (e.g., Singer et al. 2013a). We downloaded the X-ray light curves from the XRT Light Curve Repository⁵. The time-averaged spectrum was well described (W-stat = 299.10 for 374 degrees of freedom) by a power-law model, $\Gamma = 1.84 \pm 0.12$, with no evidence for N_{H} in excess of the Galactic value ($N_{\text{H,Gal}} = 1.83 \times 10^{20} \text{ cm}^{-2}$; Kalberla et al. 2005).

We initiated deep X-ray follow-up observations of GRB 130702A with the *Chandra* X-ray Observatory on 2013 September 5, corresponding to $\Delta t = 65.2$ d since trigger (PI R. Margutti). The data were reduced with the CIAO software

⁵See http://www.swift.ac.uk/xrt_curves and the associated description in Evans et al. (2009).

package (version 4.6) and corresponding calibration files. Standard ACIS data filtering has been applied. In 14.9 ks of observations we find clear evidence for X-ray emission at the location of GRB 130702A, with significance $> 50\sigma$. The spectrum was well modeled by an absorbed power law with $\Gamma = 1.66 \pm 0.15$, consistent with the *Swift*-XRT time-averaged spectrum. We found no evidence for an intrinsic absorption component, with a 3σ limit of $N_{\text{H,host}} < 1.5 \times 10^{21} \text{ cm}^{-2}$. Adopting these spectral parameters, the unabsorbed flux is $F_X = (1.20 \pm 0.08) \times 10^{-13} \text{ erg s}^{-1} \text{ cm}^{-2}$ (0.3–10 keV).

A second epoch of *Chandra* observations was obtained on 2013 December 6 ($\Delta t = 157.5 \text{ d}$) with an exposure time of 34.6 ks. GRB 130702A was clearly detected with significance $> 40\sigma$, which allows us to constrain the spectral evolution (or lack thereof) of GRB 130702A at very late times. Our spectral analysis reveals no evidence for spectral evolution. The best-fitting power-law index was $\Gamma = 1.85 \pm 0.16$, with $N_{\text{H,host}} < 1.6 \times 10^{21} \text{ cm}^{-2}$ at 3σ confidence level. The corresponding unabsorbed flux is $F_X = (4.5 \pm 0.45) \times 10^{-14} \text{ erg s}^{-1} \text{ cm}^{-2}$ (0.3–10 keV).

The X-ray light curve of GRB 130702A, comprising *Swift*-XRT and *Chandra* observations, is presented in Figure 2.4.

2.4 Light-Curve Analysis

2.4.1 Isolating the Supernova Component

Emission from the location of GRB 130702A results from three distinct components: the GRB afterglow, the associated SN, and the underlying host galaxy.

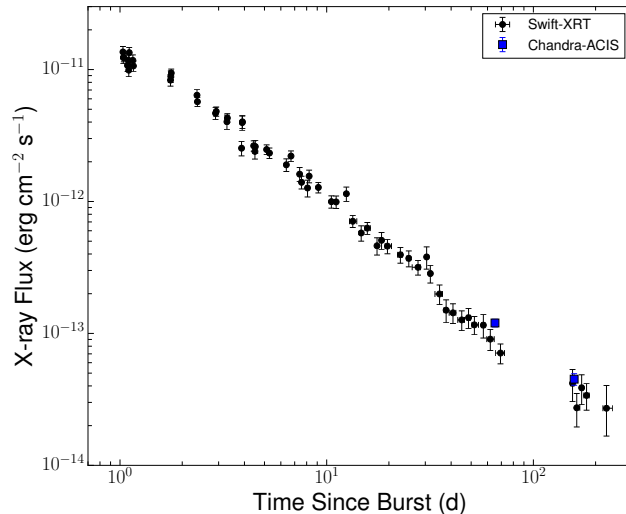


Figure 2.4 X-ray light curve of GRB 130702A.

Here we try to isolate the emission resulting from the associated SN, including a proper accounting for line-of-sight extinction, in order to study the properties of SN 2013dx.

First, we correct our broadband photometry for extinction, both in the Milky Way and in the host galaxy. For the Galactic component, we employ the dust-map calibration of Schlafly & Finkbeiner (2011), resulting in $E(B - V)_{\text{MW}} = 0.038$ mag, and the Milky Way extinction law of Cardelli et al. (1989). In order to estimate the host extinction, $A_{V,\text{host}}$, we create an SED at $\Delta t = 2.25$ d from linear interpolation. We assume the observed emission at this stage will be dominated by the (synchrotron) afterglow, and thus we fit the SED to a simple power-law model of the form $f_\nu \propto \nu^{-\beta}$ (e.g., Sari et al. 1998). We incorporate $A_{V,\text{host}}$ as a free parameter, assuming a Small Magellanic Cloud (SMC)-like extinction law (Pei, 1992). We find $A_V = 0.13 \pm 0.23$ mag and $\beta = 0.52 \pm 0.19$ with a reduced $\chi_{\text{red}}^2 = 0.83$. Adopting Large Magellanic Cloud (LMC) and Milky Way (MW) dust extinction laws did not

alter the derived parameters or fit quality. For the rest of this paper we assume $A_{V,\text{host}} = 0.10$ mag. This is consistent with other GRB host-extinction values: 50% of GRBs have $A_{V,\text{host}} < 0.4$ mag and 87% of GRBs have $A_{V,\text{host}} < 2$ mag (Covino et al., 2013).

Next, we attempt to remove any contribution from the afterglow. Singer et al. (2013a) modeled the early-time optical emission ($\Delta t \lesssim 4$ d) as a broken power law with an initial decay index of $\alpha_1 = 0.57 \pm 0.03$ up to the break time, $t_b = 1.17 \pm 0.9$ d, after which the model followed a power-law decay index of $\alpha_2 = 1.05 \pm 0.03$. We repeat this analysis with our larger photometric dataset and find mostly consistent results. However, even as early as several days post-trigger, the observed emission will likely have some contribution from the emerging SN (e.g., the broad features becoming apparent in the $\Delta t = 3.25$ d DBSP spectrum in Figure 2.5). Consequently, the true afterglow decay index may be steeper than indicated here.

Instead, we consider the decay of the corresponding X-ray emission, which is unlikely to be contaminated by the SN at $\Delta t \gtrsim 1$ d. We fit the X-ray light curve to a power-law model and find $\alpha_X = 1.25 \pm 0.03$. Combining this with the measured X-ray spectral index from the *Swift*-XRT data, $\beta_X = 0.84 \pm 0.12$, we can use standard afterglow closure relations (e.g., Racusin et al. 2009, and references therein) to evaluate where the X-rays fall on the broadband synchrotron spectrum. The best fit is found for a constant-density circumburst medium with the X-rays falling below the synchrotron cooling frequency, ν_c .

As a result, the optical bandpass must fall below ν_c as well, which is consistent with the measured X-ray to optical spectral index of $\beta_{OX} \approx 0.7$ at $\Delta t = 2$ d. Thus,

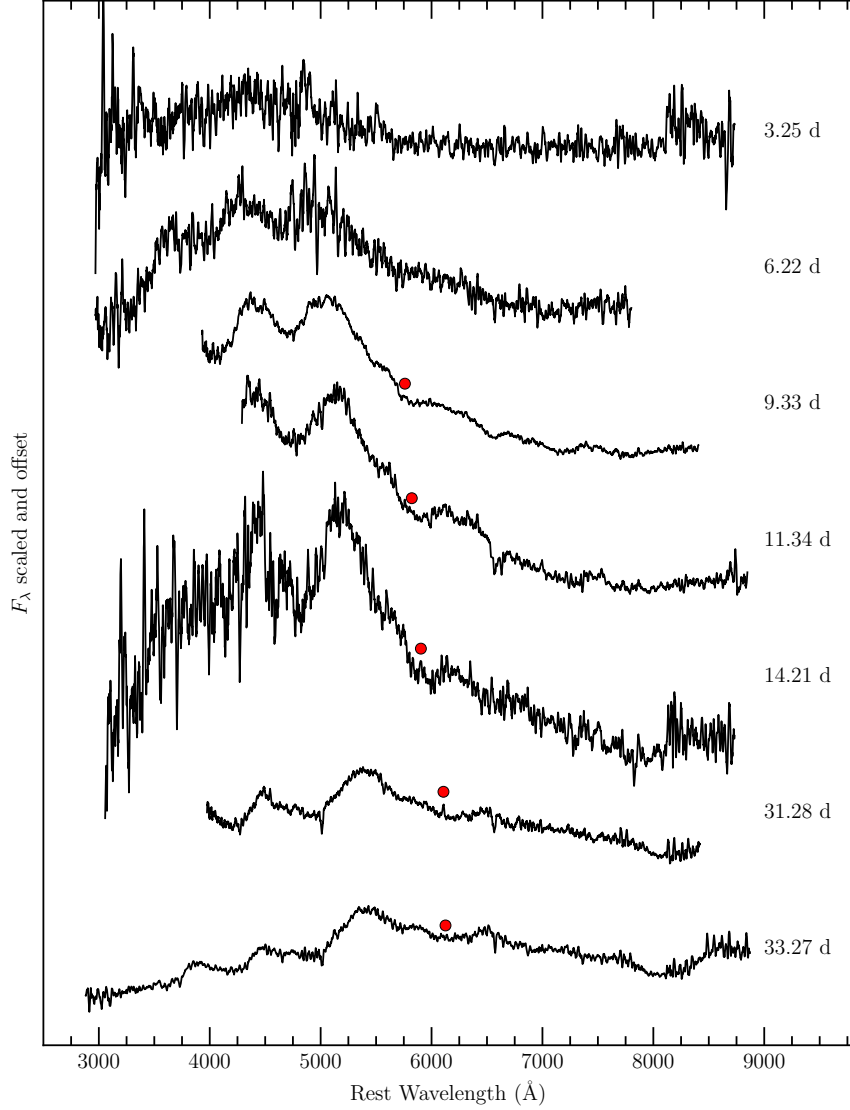


Figure 2.5 SN 2013dx spectra with host galaxy and GRB afterglow removed. They are smoothed using a Savitzky-Golay filter with a 30 \AA window. We excluded the spectrum at $t = 1.17 \text{ d}$ because it is dominated by the afterglow. Red filled circles mark the position of Si II $\lambda 6355$ calculated in §2.5.3, used to determine the photospheric velocity of the ejecta. The uncertainties are smaller than the symbol width; they are 20 \AA for $t = 9.33 \text{ d}$ and 10 \AA for subsequent epochs.

since the optical emission falls on the same segment of the SED as the X-rays, it should decay with the same power-law index, $\alpha_O = 1.25$. We further assume that both the optical afterglow spectral and temporal indices remain constant in time over the course of our observations. We use this model to calculate the afterglow contribution for all our photometric observations.

We note that this is a significantly shallower decay index than the $\alpha_O = 2.2$ adopted by D15, who did not incorporate multi-wavelength observations into their afterglow analysis. A steeper α_O may overestimate the SN flux at early times, but is negligible at the peak and late times when the SN is significantly brighter than the afterglow.

Finally, we must remove the contribution from the underlying host galaxy. In our best-seeing images at late times (FWHM $\approx 0''.75$), the host is clearly resolved, with the afterglow/SN location falling on a blue “knot” to the north (Figure 2.2). This location is also responsible for the nebular emission lines seen in the final Keck/LRIS spectrum (Figure 2.3).

To remove the host contribution from our photometry, we adopt host flux values from our late-time DCT ($g'r'i'z'$) and Keck/MOSFIRE (J) imaging and directly subtract these from the measured transient fluxes. While this does not account for the resolved nature of the host, since the typical seeing in our SN data ($\sim 1''.5$) is comparable to the size of the extended emission, this should have minimal impact on the resulting photometry. We do not have host-galaxy detections in the y and H bands, but the host contribution is negligible compared to the afterglow and SN components.

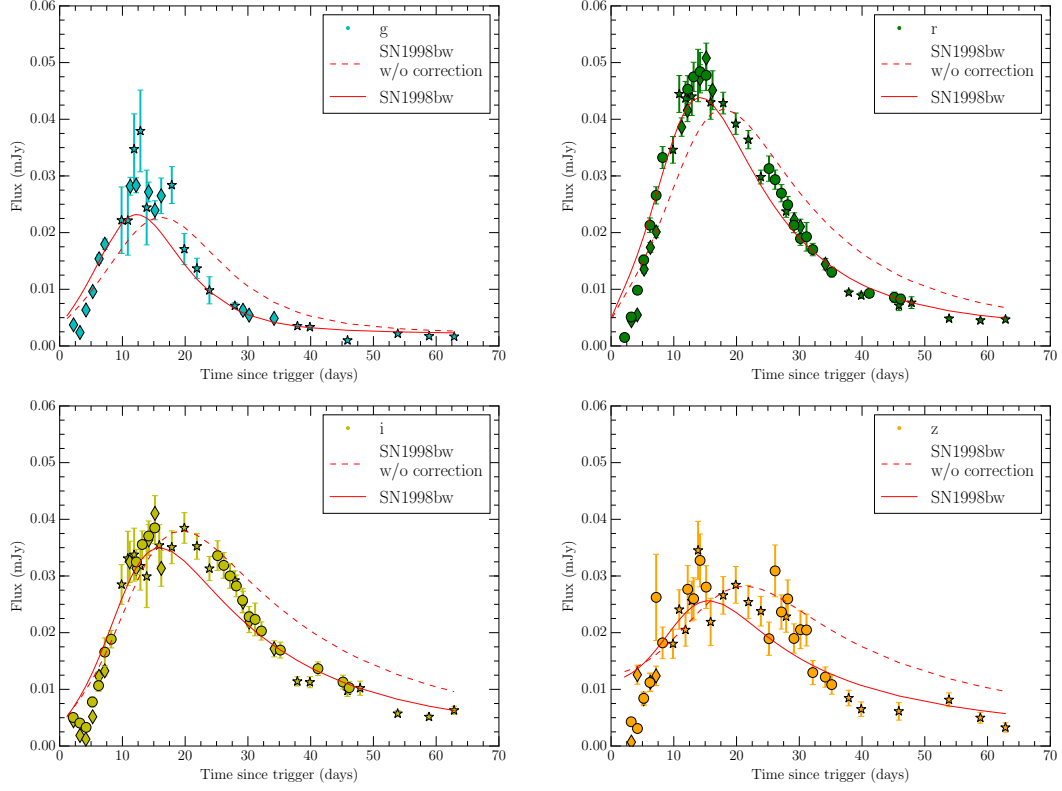


Figure 2.6 Observed SN 2013dx $g'r'i'z'$ data (top left, top right, bottom left, and bottom right, respectively), with synthetic SN 1998bw light-curve fit (dashed red line) and an optimized synthetic SN 1998bw light-curve fit scaled by a peak-amplitude factor k and time-stretch factor s (solid red line; see §2.4.2) overlaid. SN 1998bw template created from Clochiatti et al. (2011), Galama et al. (1998), Sollerman et al. (2002), and Patat et al. (2001). Diamonds are P48/P60 data, circles are RATIR data, and stars are Liverpool data.

The resulting SN light curves are displayed in Figure 2.6. The peak times of the light curves are useful for constraining theoretical models, in particular the convolution of total ejected mass, kinetic energy, and opacity of the SN explosion (via the diffusion time). We measure the rest-frame peak times by fitting a second-order polynomial at $7 \leq \Delta t < 20$ d and find the following: $t_p(g') = 11.7 \pm 0.3$ d, $t_p(r') = 13.2 \pm 0.3$ d, $t_p(i') = 14.7 \pm 0.6$ d, and $t_p(z') = 15.1 \pm 1.6$ d (statistical uncertainties only). These values generally agree well with those reported by D15. We do not include peak times for yJH because the data are not well sampled close

Table 2.3. SN 1998bw Template Fits

Filter	s	k	χ_{red}^2
g'	0.76 ± 0.05	1.02 ± 0.06	7.78
r'	0.79 ± 0.01	1.05 ± 0.02	4.67
i'	0.82 ± 0.02	0.92 ± 0.03	4.07
z'	0.74 ± 0.04	0.91 ± 0.05	2.85

to the peak.

There is marginal evidence in the i' -band light curve (Figure 2.6) of a decline in flux at early times ($\Delta t \lesssim 3$ d). This is consistent with early signatures of shock cooling (e.g., SN 2006aj, Campana et al. 2006; SN 2010bh, Cano et al. 2011). However, shock breakout should be significantly stronger in bluer bands and we see no indication of it in either the g' or r' bands. The relatively bright optical afterglow of GRB 130702A, compared to the optical afterglows of (for example) GRB 060218 and GRB 100316D, greatly complicates isolating the SN component at early times. Thus, it is difficult to reach firm conclusions regarding the presence or absence of a shock-breakout signature.

2.4.2 Comparison with SN 1998bw

Following past studies of GRB-associated SNe in the literature, we next attempt to compare SN 2013dx to the well-studied SN 1998bw (associated with GRB 980425). We create K-corrected synthetic SN 1998bw light curves in the $g'r'i'z'$ filters at the redshift of SN 2013dx, $z = 0.145$, using methods described by Hogg et al. (2002). We utilize SN 1998bw photometry and spectra from Clocchiatti et al. (2011), Galama et al. (1998), Sollerman et al. (2002), and Patat et al. (2001). The

K-corrected synthetic SN 1998bw light curves were also time dilated to match the observer frame of SN 2013dx.

Owing to gaps in the temporal coverage of SN 1998bw photometry, especially in the rising phase, we fit the synthetic SN 1998bw light curve in each filter with the empirical functional form from Cano et al. (2011),

$$U(t) = A + pt \left(\frac{e^{(-t^{\alpha_1}/F)}}{1 + e^{(p-t/R)}} \right) + t^{\alpha_2} \log(t^{-\alpha_3}), \quad (2.1)$$

allowing $A, p, F, R, \alpha_1, \alpha_2,$ and α_3 to vary. The resulting SN 1998bw synthetic light curves are plotted as dashed lines in Figure 2.6.

We then assume the light curves of SN 2013dx in each of our four filters can be modeled by simply varying the peak amplitude (k) and stretch factor (s):

$$L_{13dx}(t) = k U_{98bw}(t/s). \quad (2.2)$$

The resulting fits are plotted in Figure 2.6, while the measured stretch and amplitude values are displayed in Table 2.3. We find that SN 2013dx has a peak flux comparable to that of SN 1998bw in all four filters reported here (slightly more luminous in the bluer filters, and slightly less luminous in the redder filters). With a constant stretch value of $s \approx 0.8$ in all four filters, the evolution of SN 2013dx (in particular the rise time) is noticeably faster than that of SN 1998bw.

However, it is also clear from the fits that SN 1998bw is not an ideal match to SN 2013dx, especially in the redder i - and z -band filters. Given these important

differences, we refrain from drawing any physical inferences (e.g., M_{Ni} , E_{K}) from these fits, and instead use the more model-independent bolometric light curve in §2.6.

Cano (2014) and Lyman et al. (2014a) suggested that GRB-SNe can be used as standardizable candles. Cano (2014) proposed that s and k (measured relative to SN 1998bw) are analogous to the absolute peak SN magnitude and the amount the light curve fades from maximum light to 15 d later (Δm_{15}) used in the Phillips relation (Phillips, 1993) for SNe Ia. We add the uncertainties from our s and k fit in quadrature and find that our measurements of SN 2013dx deviate by 3.7σ from the Cano (2014) fits. The worst fits to Cano (2014) are for g' and r' at 3.7σ ; however, z' is within 0.9σ . This further supports the notion that SN 1998bw is not a perfect match for all GRB-associated SNe.

2.4.3 Bolometric Light Curve

We construct the quasi-bolometric light curve of SN 2013dx using our photometry in the g' , r' , i' , z' , y , and J filters (H had only upper limits at $\Delta t \gtrsim 5$ d). We include synthetic photometry for $\Delta t = 31.28$ and 33.27 d from our spectra (see §2.5.1) to supplement photometric coverage at these epochs. We assume a 10% flux error on all synthetic photometry data points. We convert the extinction, host-galaxy, and afterglow-corrected magnitudes to monochromatic fluxes and create SEDs from linear interpolation of the data for each epoch between 1 d and 70 d with 0.25 d spacing. Epochs that are > 0.5 d from observations are removed to mitigate

linear-interpolation errors, which only affects observations in the y and J bands (see below). We assume that the flux is constant across the bandwidth of each filter and use trapezoidal integration to calculate the quasi-bolometric luminosity. We note that our photometry provides coverage over the observer-frame bandpass $0.4\text{--}1.35\ \mu\text{m}$ (rest-frame $0.35\text{--}1.18\ \mu\text{m}$).

At $\Delta t \approx 15\text{--}25$ d and $\Delta t > 35$ d, the y - and J -band data are relatively sparse. We therefore calculate the bolometric luminosity for the entire light curve both including y and J ($g'r'i'z'yJ$) and excluding them ($g'r'i'z'$) to determine the NIR to integrated flux ratio. We find that the fraction of flux at these wavelengths increases monotonically as a function of time, from 13% at $\Delta t \approx 6$ d to 23% at $\Delta t \approx 29$ d. For epochs when only $g'r'i'z'$ observations were available, we add a fractional NIR contribution for the y - and J -band from our linear fit. At late times we adopt the last NIR ratio measurement at $\Delta t \approx 29$ d of $\sim 23\%$ instead of extrapolating our linear fit. This may underestimate the NIR contribution at late times. Our NIR contribution measurements are consistent with an analogous measurement for SN 2008D (Modjaz et al., 2009), though slightly smaller than for SN 2009bb and SN 2010bh (Cano et al., 2011), which have maximum NIR contributions of 35–45% at $\Delta t \approx 25$ d.

The resulting bolometric light curve is displayed in Figure 2.7. Our associated uncertainty measurements incorporate errors from the flux measurements, as well as bandpass uncertainties, but do not include errors introduced from linear interpolation.

Lyman et al. (2014b) have created a model for core-collapse SN bolometric

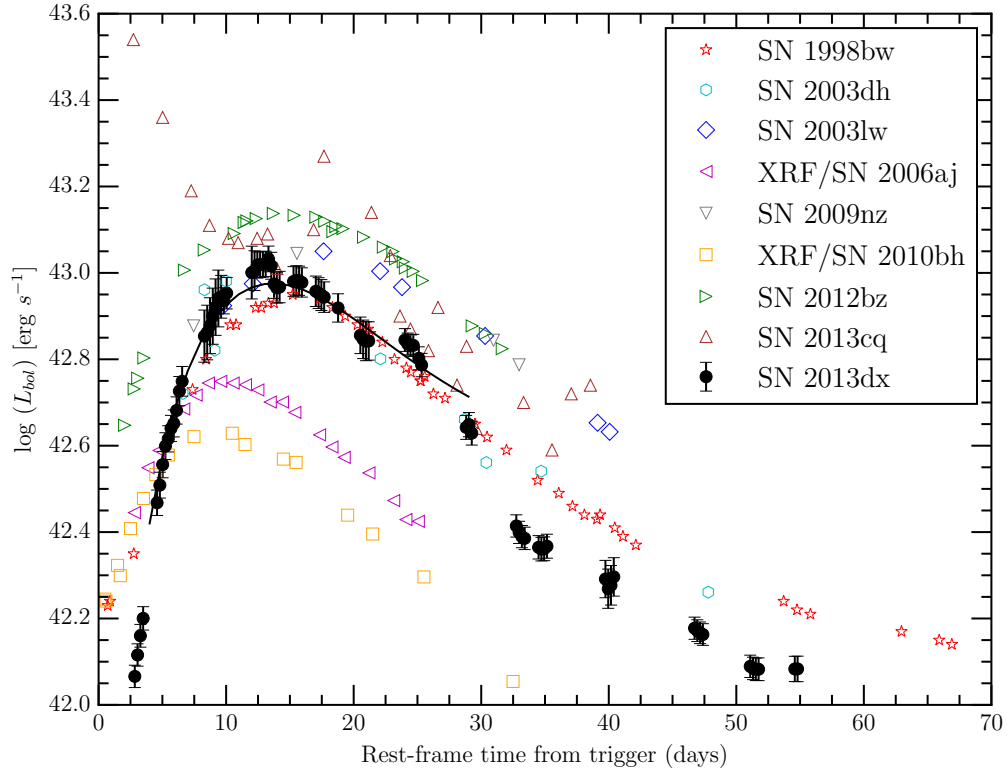


Figure 2.7 $g'r'i'z'yJ$ bolometric light-curve fit with Arnett-Valenti relation fit for $4 \leq t \leq 30$ d (solid black line). Bolometric light curves of other spectroscopically confirmed GRB-SNe are included for comparison. Note that these “bolometric” light curves are actually “quasi-bolometric” and cover different wavelength ranges.

corrections using two filters for nearby events. The corrections include ultraviolet and NIR contributions. Since SN 2013dx is at $z = 0.145$, we use our K-corrected spectra (see §2.5.1) to extract g' and r' synthetic photometry. We apply the methodology described by Lyman et al. (2014b) and find that this model leads to excellent agreement with our brute-force $g'r'i'z'yJ$ bolometric light curve. This confirms that we are not underestimating the ultraviolet and NIR contributions in our quasi-bolometric light curve.

2.5 Spectral Analysis

2.5.1 Isolating the SN Component

In a similar manner to that of §2.4.1, we wish to isolate the SN component from our spectroscopic observations of GRB 130702A. First, for absolute-flux calibration, we normalize our spectra to (uncorrected) broadband photometry at the appropriate epoch. This accounts for slit losses caused by variable seeing.

We next deredden our spectra of SN 2013dx in an analogous manner to that of §2.4.1. This includes contributions from both the Milky Way [$E(B-V) = 0.038$ mag] and the host galaxy ($A_{V,\text{host}} = 0.1$ mag).

To remove the afterglow contribution, we assume that the spectrum can be described at all times (and frequencies) as a power law of the form $f_\nu(t, \alpha) \propto t^{-\alpha} \nu^{-\beta}$, with $\alpha = 1.25$ and $\beta = 0.52$ (§2.4.1). We normalize this function to our (extinction-corrected) broadband photometry, and subtract the appropriate power-law model at the epoch of each spectrum.

Finally, we fit the LMI/DCT late-time photometry to a variety of template galaxies from Kinney et al. (1996). Similar to D15, we find that the best-fit template is a starburst galaxy, and we adopted this (appropriately normalized) as the host contribution to the spectra. We take this approach instead of using our final Keck/LRIS spectrum because of the blue-shutter failure.

After these corrections, only the SN component remains. Figure 2.5 displays the resulting spectra of SN 2013dx after smoothing. We exclude the first spec-

trum ($\Delta t = 1.17$ d) because it is completely afterglow dominated. In addition, we manually excise nebular emission lines from the host galaxy of SN 2013dx.

2.5.2 Comparison with Other Type Ic-BL SNe

The early-time spectra of SN 2013dx are fairly featureless, but after a week, broad ($v \approx 3 \times 10^4 \text{ km s}^{-1}$) features appear. Together with the lack of obvious H and He emission, this leads us to classify SN 2013dx as a broad-lined Type Ic SN (Ic-BL), as has been the case for essentially all well-studied GRB-associated SNe thus far (e.g., Woosley & Bloom 2006).

In Figure 2.8, we plot the spectrum of SN 2013dx obtained around maximum light ($\Delta t = 14.2$ d) and at late times ($\Delta t = 33.3$ d) with pseudocontinuum removed, bandpass filtered, scaled, and binned to a common logarithmic wavelength scale along with mean spectra of Type Ic-BL SNe both with and without GRBs from Modjaz et al. (2015). We note that the mean spectra include spectra of SN 2013dx from D15, but this is one of many objects. The absorption features from mean Type Ic-BL SNe both with and without GRBs align well with SN 2013dx absorption features. This indicates that SN 2013dx has similar photospheric velocities as other Type Ic-BL SNe.

At maximum light SN 2013dx has a similar blueshifted, broad Si II $\lambda 6355$ line as both SNe Ic-BL with and without GRBs. The blended Fe II absorption feature around a blueshifted wavelength of 4800 \AA is similar to that of SNe Ic-BL with GRBs but is weaker than that of SNe Ic-BL without GRBs. SN 2013dx has a stronger

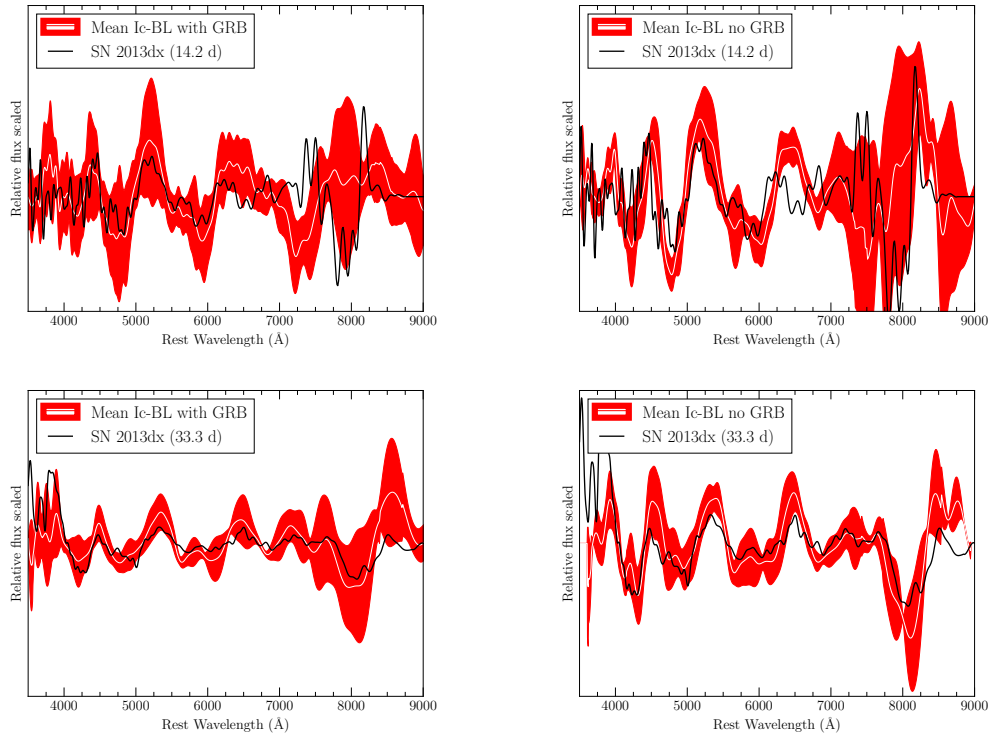


Figure 2.8 SN 2013dx spectrum with pseudocontinuum removed and bandpass filtered, binned to a common logarithmic wavelength scale (black). The mean (white) and standard deviation (red) of Type Ic-BL spectra from Modjaz et al. (2015) with (left) and without (right) GRB within 2 rest-frame days of the SN 2013dx spectrum. (*top*) Spectrum taken at $\Delta t = 14.2$ d, closest to maximum light in r' ($\Delta t = 13.2$ d) and i' ($\Delta t = 14.7$ d). (*bottom*) Spectrum taken at $\Delta t = 33.3$ d.

Ca II absorption feature around 7900 \AA and weaker O I absorption feature around 7200 \AA than most SNe Ic-BL both with and without GRBs.

At later epochs, SN 2013dx does not deviate from the mean SN Ic-BL both with and without GRBs except beyond 8200 \AA . However, the relative variation from the continuum seems weaker than the mean spectra of both SNe Ic-BL with and without GRBs. SN 2013dx has a similar Ca II absorption feature around 7900 \AA as SNe Ic-BL with GRBs but weaker than that of SNe Ic-BL without GRBs.

To search for other similar objects in the literature, we use the cross-correlation

tool SN Identification code (SNID; Blondin & Tonry 2007). Several SNe Ic-BL that were not associated with GRBs, such as SN 1997ef (Iwamoto et al., 2000) and SN 2007I (Blondin et al., 2007; Modjaz et al., 2014), also provide good matches to SN 2013dx. In addition, D15 highlight similarities to the energetic SN 2010ah (PTF10bzf; Corsi et al. 2011; Mazzali et al. 2013).

2.5.3 Photospheric Velocity Measurements

In order to estimate the photospheric velocity of SN 2013dx, we measure the velocity of the most prominent spectral feature, the Si II 6355 Å absorption line. We employ a fitting code in IDL that removes a linear pseudocontinuum and fits a Gaussian to the absorption line (see Silverman et al. 2012 and Silverman et al. 2015 for a detailed description of the code). Table 2.4 displays the inferred velocities for each spectrum. Our results are also consistent with those reported by D15. The first three spectra ($\Delta t = 1.17, 3.25,$ and 6.22 d) are too noisy for reliable velocity measurements.

We note that Parrent et al. (2015) suggests the absorption feature at ~ 6100 Å, normally identified as Si II 6355 Å, may be instead associated with H α . Therefore, we compare mean SN Ic-BL photospheric velocities measured using Fe II 5169 Å (Modjaz et al., 2015) at maximum light. We find that our measurements are consistent with the measurements from the less-contaminated Fe II 5169 Å.

Table 2.4. Velocity of Si II λ 6355

Δt (d)	Velocity (km s^{-1})
9.3	$28,100 \pm 1000$
11.3	$25,200 \pm 500$
14.2	$21,300 \pm 500$
31.3	$11,700 \pm 500$
33.3	$10,800 \pm 500$

Note. — In observer frame. The reported uncertainties come from fitting the Si II λ 6355 absorption feature with a single Gaussian function and do not include errors from potential blending.

2.5.4 Line Identification

We use SYN++ (Thomas et al., 2011) to help identify the ions present in our spectra of SN 2013dx. SYN++ is derived from SYNOW (Fisher et al., 1997), which uses the Sobolev approximation (Sobolev, 1960; Castor, 1970; Jeffery, 1989) to produce synthetic spectra of SNe during the photospheric phase. SYN++ assumes that spectral lines are formed via resonance scattering above a sharp photosphere. The location of the photosphere is expressed in velocity coordinates as v_{ph} (in km s^{-1}) and takes into account the homologous expansion of the ejecta.

The optical depths for each species must also be input and line strengths are computed assuming Boltzmann excitation (i.e., local thermodynamic equilibrium, LTE) using a specified excitation temperature T_{exc} (in K). Non-LTE effects are partially taken in account by allowing different T_{exc} values for each species, all of which can be different from the photospheric temperature T_{phot} . The latter is used

only in computing the blackbody radiation emitted by the photosphere. All our SYN++ fits are computed with all ions turned on simultaneously with a blackbody.

We attempt to model the major spectral features of SN 2013dx at $\Delta t = 9.3$ and 33.3 d and look for evolution during the photospheric phase (see Figure 2.9). At 9.3 d after the burst, SYN++ indicates a photospheric velocity of $30,000 \text{ km s}^{-1}$, an outer velocity of the line-forming region of about $90,000 \text{ km s}^{-1}$, and an estimated photospheric temperature of $16,000 \text{ K}$. The spectrum contains absorption from O I, Si II, and Fe II, and possible absorption signatures of Fe III, Mg II, C II, Ca II, and Na I. We caution that because of the relatively uncertain line identifications, the derived velocities are robust indicators only for the lines of Fe II and Si II.

By 33.3 d after the burst, according to our second SYN++ fit, the SN ejecta have slowed down and cooled off significantly. This model indicates approximate values for the photospheric velocity, outer velocity, and photospheric temperature of $11,000 \text{ km s}^{-1}$, $60,000 \text{ km s}^{-1}$, and 9000 K , respectively. The majority of the absorption in this spectrum is likely produced by Fe II and Ti II, though there is some evidence of Si II, Ca II, and possibly O I as well. While the fit to this spectrum at wavelengths below $\sim 4700 \text{ \AA}$ is not perfect, the broad peaks and troughs roughly match. This part of the spectrum is notoriously difficult to model owing to hundreds of overlapping spectral features, mostly from iron-group elements.

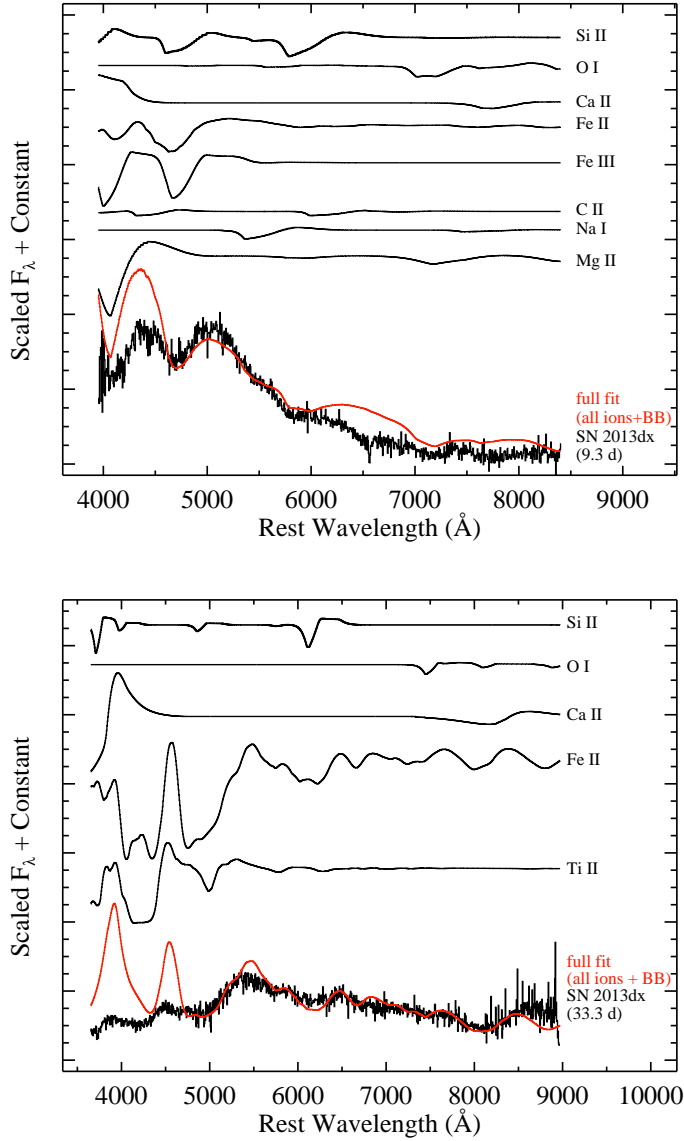


Figure 2.9 SYN++ fits to the 9.3 d (top) and 33.3 d (bottom) spectra of SN 2013dx. The spectrum of each individual ion is labeled. Their sum – plus a 16,000 K (top) and 9000 K (bottom) blackbody – is plotted in red on top of the actual observed spectra of SN 2013dx (binned to 6 \AA per pixel).

2.6 Supernova Explosion Parameters

2.6.1 Derived Parameters

We model the basic explosion parameters of SN 2013dx by fitting its bolometric light curve with the Type I SN analytical model of Arnett (1982) and Valenti et al. (2008). This model assumes (1) homologous expansion of the ejecta, (2) spherical symmetry, (3) all ^{56}Ni is located at the center of explosion and no mixing, (4) radiation-pressure dominated ejecta, (5) the initial radius before explosion is small, (6) the diffusion approximation is appropriate for photons (i.e., the ejecta are in the photospheric phase), and (7) a single opacity over the duration of the explosion.

The peak luminosity correlates with the mass of ^{56}Ni (M_{Ni}), while the light-curve shape is determined by the total ejecta mass (M_{ej}) and the ejecta kinetic energy (E_{K}). We can break the degeneracy between M_{ej} and E_{K} with photospheric-velocity measurements from our optical spectra.

The timescale of the light curve is given by

$$\tau_m = \left(\frac{\kappa}{\beta c}\right)^{1/2} \left(\frac{6M_{\text{ej}}^3}{5E_{\text{K}}}\right)^{1/4}, \quad (2.3)$$

where $\beta \approx 13.8$ is an integration constant. For a uniform density (Arnett, 1982)⁶,

$$E_{\text{K}} \approx \frac{3}{5} \frac{M_{\text{ej}} v_{\text{ph}}^2}{2}. \quad (2.4)$$

⁶Note there is a typo incorrectly stating $E_{\text{K}} \approx \frac{5}{3} \frac{M_{\text{ej}} v_{\text{ph}}^2}{2}$ in the original text that was corrected by Arnett (1996). This has been taken into account in Equations 2.3 and 2.4. This typo has been propagated throughout the literature.

We assume $\kappa = 0.07 \text{ cm}^2 \text{ g}^{-1}$ to directly compare with the literature for other GRB-SNe (e.g., Cano et al. 2011).

We fit our quasi-bolometric light curve (§2.4.3) with the Arnett-Valenti relation,

$$L_{\text{ph}}(t) = M_{\text{Ni}} e^{-x^2} \times \left[(\epsilon_{\text{Ni}} - \epsilon_{\text{Co}}) \int_0^x A(z) dz + \epsilon_{\text{Co}} \int_0^x B(z) dz \right], \quad (2.5)$$

with

$$\begin{aligned} A(z) &= 2ze^{-2zy+z^2}, \\ B(z) &= 2ze^{-2zy+2zs+z^2}, \\ x &\equiv t/\tau_m, \\ y &\equiv \tau_m/(2\tau_{\text{Ni}}), \text{ and} \\ s &\equiv \tau_m(\tau_{\text{Co}} - \tau_{\text{Ni}})/(2\tau_{\text{Co}}\tau_{\text{Ni}}). \end{aligned} \quad (2.6)$$

The decay times of ^{56}Ni and ^{56}Co are $\tau_{\text{Ni}} = 8.77 \text{ d}$ and $\tau_{\text{Co}} = 111.3 \text{ d}$, and the energies produced in one second by one gram of ^{56}Ni and ^{56}Co were taken as $\epsilon_{\text{Ni}} = 3.90 \times 10^{10} \text{ erg s}^{-1} \text{ g}^{-1}$ and $\epsilon_{\text{Co}} = 6.78 \times 10^9 \text{ erg s}^{-1} \text{ g}^{-1}$ (Sutherland & Wheeler, 1984; Cappellaro et al., 1997).

From our spectra and light curves, the SN component was dominant starting at $\Delta t \approx 4 \text{ d}$ (compare with SN 2010bh, where shock breakout was prominent out to 7 d; Cano et al. 2011). The Arnett-Valenti relation assumes that the material is in the photospheric phase, which is no longer valid at $\Delta t \gtrsim 30 \text{ d}$. Therefore, our fit

only includes $4 \leq \Delta t \leq 30$ d. We find $M_{\text{Ni}} = 0.37 \pm 0.01 M_{\odot}$ and $\tau_{\text{m}} = 11.35 \pm 0.17$ d (statistical errors only). Using $v_{\text{ph}} = 21,300 \text{ km s}^{-1}$ from our spectral fit near peak (§2.5.3), we calculate $M_{\text{ej}} = 3.1 \pm 0.1 M_{\odot}$ and $E_{\text{K}} = (8.2 \pm 0.43) \times 10^{51}$ erg.

2.6.2 Comparison with Other GRB-SNe

We compare our bolometric light curve of SN 2013dx with that of other spectroscopically confirmed GRB-SNe in Figure 2.7 (SN 1998bw, Galama et al. 1998; SN 2003lw, Mazzali et al. 2006; SN 2003dh, Deng et al. 2005; SN 2006aj, Pian et al. 2006; SN 2009nz, Olivares E. et al. 2015, SN 2010bh, Olivares E. et al. 2012; SN 2012bz: Melandri et al. 2012 and Schulze et al. 2014; SN 2013cq: Melandri et al. 2014; iPTF14bfu: Cano et al. 2015). We note that the NIR contribution to the bolometric luminosity for SN 2012bz is assumed to be the same as that observed for SN 2010bh. Although these GRB-SN bolometric light curves cover different wavelength ranges, we can get a sense of the light-curve evolution. SN 2013dx most closely matches the light-curve shape of SN 2012bz, but with the caveat that SN 2013dx has a steeper rise than SN 2012bz.

After 30 days, SN 2013dx appears to drop in luminosity rapidly. This is unlike the three bursts with late-time coverage – SN 2003lw, SN 2003dh, and SN 1998bw – seen particularly well juxtaposed against SN 1998bw, which has extensive observations out to hundreds of days. This drop in luminosity is not from underestimating the NIR contribution at late times; we still observe a rapid drop in luminosity at 30 d if we continue the monotonically increasing NIR ratio function from §2.4.3 instead

Table 2.5. Physical Parameters of GRB-SNe

GRB-SN	z	$E_{\gamma,\text{iso}}$ (erg)	v_{ph} (km s^{-1})	M_{Ni} (M_{\odot})	M_{ej} (M_{\odot})	E_{K} (10^{52} erg)	Reference
GRB 980425/SN 1998bw	0.0085	$(9.29 \pm 0.35) \times 10^{47}$	18,000	0.42 ± 0.02	6.80 ± 0.57	$1.31 \pm 0.10^{\text{a}}$	(1), (2)
GRB 030329/SN 2003dh	0.1685	1.33×10^{52}	20,000	0.54 ± 0.13	5.06 ± 1.65	$1.21 \pm 0.39^{\text{a}}$	(1), (2)
GRB 031203/SN 2003lw	0.105	$1.67^{+0.04}_{-0.10} \times 10^{50}$	18,000	0.57 ± 0.04	8.22 ± 0.76	$1.59 \pm 0.15^{\text{a}}$	(1), (2)
GRB 060218/SN 2006aj	0.0335	$4.33^{+0.41}_{-1.74} \times 10^{49}$	20,000	0.21 ± 0.03	2.58 ± 0.55	$0.61 \pm 0.14^{\text{a}}$	(1), (2)
GRB 091127/SN 2009nz	0.49	$(4.3 \pm 0.3) \times 10^{52}$	17,000	0.33 ± 0.01	4.69 ± 0.13	$0.81 \pm 0.02^{\text{a}}$	(1), (3)
GRB 100316D/SN 2010bh ^b	0.059	$\geq (3.9 \pm 0.3) \times 10^{49}$	25,000	0.12 ± 0.02	2.47 ± 0.23	$0.92 \pm 0.08^{\text{a}}$	(1), (4)
GRB 120422A/SN 2012bz ^b	0.283	4.5×10^{49}	20,500	0.57 ± 0.07	6.10 ± 0.49	$1.53 \pm 0.13^{\text{a}}$	(1), (5)
GRB 130427A/SN 2013cq	0.3399	$(9.6 \pm 0.04) \times 10^{53}$	32,000	0.28 ± 0.02	6.27 ± 0.69	6.39 ± 0.70	(6)
GRB 130702A/SN 2013dx	0.145	$6.4^{+1.3}_{-1.0} \times 10^{50}$	21,300	0.37 ± 0.01	3.1 ± 0.1	0.82 ± 0.04	(7)
GRB 140606B/iPTF14bfu	0.384	$(3.47 \pm 0.02) \times 10^{51}$	19,820	0.42 ± 0.17	4.8 ± 1.9	$1.1 \pm 0.7^{\text{a}}$	(8)

Note. — ^a E_{K} originally calculated as $E_{\text{K}} = \frac{M_{\text{ej}}v_{\text{ph}}^2}{2}$, scaled by a factor of 3/5 to directly compare with our values. All $E_{\gamma,\text{iso}}$ values calculated over 1 keV – 10 MeV, except those indicated by superscript “b” which are calculated over 15–150 keV or superscript “c” which are calculated over 20–1400 keV. (1) Cano (2013), (2) Kaneko et al. (2007), (3) Troja et al. (2012), (4) Starling et al. (2011), (5) Zhang et al. (2012), (6) Xu et al. (2013), (7) this work, (8) Cano et al. (2015).

of adding a flat NIR contribution of 23% after 29 d.

In order to compare the derived properties of SN 2013dx with a broader sample of GRB-associated SNe, we use the derived values for M_{Ni} , M_{ej} , and E_{K} for all well-sampled events from Cano (2013). The authors fit a template of SN 1998bw to determine the appropriate stretch and scale parameters (e.g., §2.4.2). Using average s and k values for each burst, the authors then fit a scaled version of the *UBVRIJH* SN 1998bw light curve to the Arnett-Valenti model to derive the explosion parameters. This method has the benefit of (effectively) uniform wavelength coverage, even for events that were only observed in a few filters. However, the primary drawback is the assumption that all bolometric light curves are well fit by an appropriately scaled version of SN 1998bw. As evidenced by Figure 2.6, this assumption breaks down at the very least for the redder filters for SN 2013dx (see also Lyman et al. 2014a). Nonetheless, the explosion parameters for all well-studied GRB-associated SNe derived in this manner⁷ are presented in Table 2.5.

To avoid any biases introduced by GRB-SNe that are not well matched with SN 1998bw, we also create our own quasi-bolometric light curves by compiling photometry from the literature (Table 2.6). We fit these light curves with the Arnett-Valenti relation described in §2.6.1 and break our results into those events with only optical datasets and those with optical and NIR photometry in Figure 2.10 (right panel). This provides an estimate of the fundamental explosion parameters that is independent of any assumed similarity with SN 1998bw.

⁷We note that Cano (2013) and Cano et al. (2015) assume that $E_{\text{K}} = \frac{M_{\text{ej}}v_{\text{ph}}^2}{2}$, so we scaled their reported E_{K} values by a factor of 3/5.

We plot the inferred M_{Ni} as a function of both the isotropic prompt gamma-ray energy release (Figure 2.10) and the derived SN kinetic energy (E_K ; in Figure 2.11).

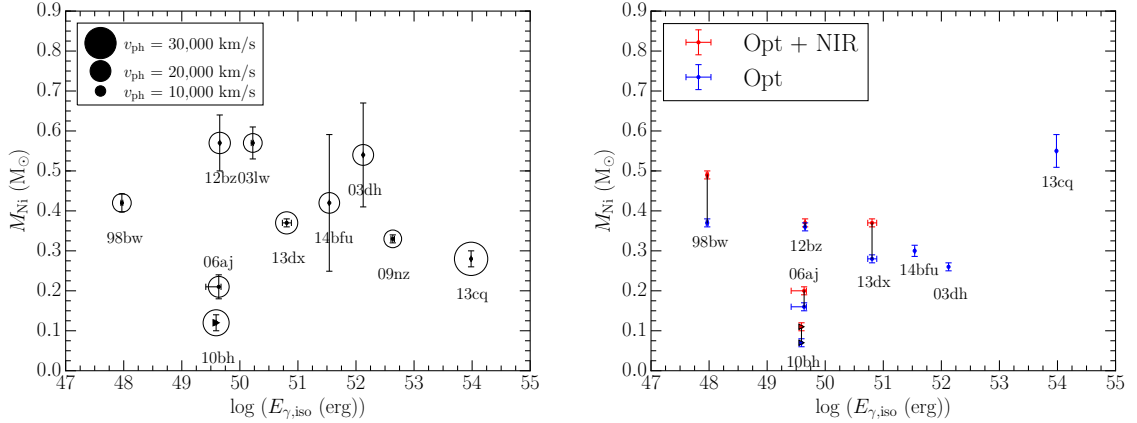


Figure 2.10 (*left*) Comparison of SN explosion parameters from template GRB-SNe and SN 2013dx from Table 2.5. The size of the points indicates v_{ph} near the SN brightness peak. There does not appear to be any correlation between M_{Ni} and $E_{\gamma,\text{iso}}$ or M_{Ni} and v_{ph} .

(*right*) Comparison of SN explosion parameters using photometric data reported in the literature with our quasi-bolometric fitting procedure. This avoids using SN 1998bw as a template for other GRB-SNe bolometric fits (see text for details). Blue points are fit to only optical data, red points are fit to optical and NIR data. Black line connects points that have both.

2.6.3 Caveats and Conclusions

From Figure 2.10, it is clear that there is no correlation between M_{Ni} and the prompt energy release using either method for calculating SN explosion parameters of other GRB-SNe. For example, SN 2013dx has a comparable mass of synthesized ^{56}Ni as the subluminous GRB 980425 / SN 1998bw and the extremely luminous GRB 130427A / SN 2013cq (Levan et al., 2014; Melandri et al., 2014). Even if we were to apply a beaming correction, GRB 130427A would still have E_{γ} several orders of magnitude larger than GRB 980425 (Perley et al., 2014), but comparable M_{Ni} .

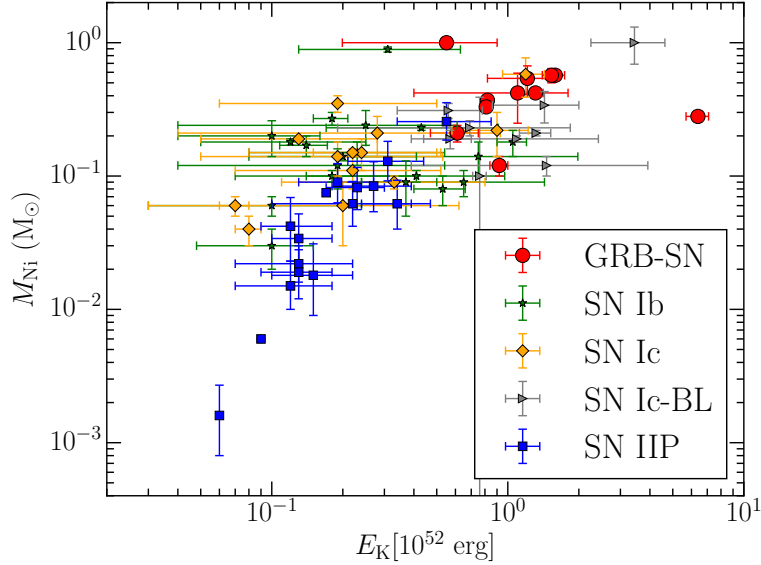


Figure 2.11 There is a clear correlation between explosion energy, E_K , and M_{Ni} for SNe Ib, Ic, Ic-BL (Cano 2013, and references therein), IIP (Hamuy 2003, and references therein), and GRB-SNe from Table 2.5. See Filippenko (1997) for a review of SN classification.

Similarly, there is no clear correlation between M_{Ni} and photospheric velocity at peak. Numerical simulations unambiguously predict that the mass of synthesized ^{56}Ni should be correlated with the degree of asymmetry in the explosion (González-Casanova et al., 2014; Umeda & Nomoto, 2008); to the extent that our models faithfully reproduce the relevant (global) SN explosion parameters, this result is clearly not borne out by the data.

On the other hand, the explosion energy *of the SN ejecta* is clearly correlated with M_{Ni} , particularly when including other core-collapse events. As shown by previous authors (e.g., Cano 2013 and Lyman et al. 2014a for recent compilations), GRB-associated SNe on average have a higher mass of synthesized ^{56}Ni and larger kinetic energies than any other class of core-collapse SNe (except perhaps the super-luminous SNe; Gal-Yam 2012). That said, the SN explosion energies are typically

Table 2.6. Photometry References for SN 1998bw-Independent Bolometric Light Curves

GRB-SN	Filter Coverage	References
GRB 980425/SN 1998bw	<i>UBVRIJHK</i>	Clocchiatti et al. (2011)
GRB 030329/SN 2003dh	<i>UBVR</i>	Deng et al. (2005)
GRB 031203/SN 2003lw ^a	—	
GRB 060218/SN 2006aj	<i>BVRIJHK</i>	Ferrero et al. (2006); Kocevski et al. (2007)
GRB 091127/SN 2009nzz ^a	—	
GRB 100316D/SN 2010bh ^b	<i>grizJH</i>	Olivares E. et al. (2012)
GRB 120422A/SN 2012bz	<i>grizJ</i>	Schulze et al. (2014)
GRB 130427A/SN 2013cq ^c	<i>BVRI</i>	Melandri et al. (2014)
GRB 130702A/SN 2013dx	<i>grizyJ</i>	This work
GRB 140606B/iPTF14bfu	<i>griz</i>	Cano et al. (2015)

Note. — ^aSimultaneous epochs near peak were limited and were insufficient for our analysis tools. ^bUsed lower host-galaxy extinction from Cano et al. (2011) and Bufano et al. (2012). ^cPoor fit using our analysis tools; we fit to the bolometric curve provided by E. Pian (private communications).

narrowly clustered and do not appear to significantly exceed 10^{52} erg, consistent with (perhaps even indicative of) a magnetar origin for these events (Mazzali et al., 2014). SN 2013cq (associated with GRB 130427A) appears to be a significant outlier in terms of its inferred E_K , however, which remains to be fully explained.

D15 created a bolometric light curve over the range 3000–10,000 Å extrapolated from u' and i' . We examined the bolometric light curve from D15 and found that our peak luminosity is consistent with theirs when accounting for our additional NIR coverage. D15 report $M_{Ni} \approx 0.2 M_{\odot}$, a factor of two lower than our quoted value. On the other hand, they derive a total ejecta mass ($M_{ej} \approx 7 \pm 2 M_{\odot}$) and a SN kinetic energy ($E_K \approx (3.5 \pm 1.0) \times 10^{52}$ erg) approximately a factor of two and four (respectively) larger than those presented here. D15 scale numerical simulations of the similarly shaped SN 2003dh (Mazzali et al., 2006) to estimate SN explosion parameters, as opposed to using an analytical model (e.g., Arnett-Valenti)

as adopted in this paper.

Since M_{Ni} is closely related to the peak luminosity, we believe that our reported M_{Ni} estimate is more accurate than the value D15 report. When NIR contributions are included, SN 2013dx has a similar peak luminosity as SN 1998bw. We therefore expect SN 2013dx to have a similar ^{56}Ni mass as SN 1998bw. Both numerical simulations and analytical models produce $M_{\text{Ni}} \approx 0.4 M_{\odot}$ for SN 1998bw (Mazzali et al., 2006; Cano, 2013).

The discrepancy in ejecta mass and kinetic energy is caused mainly by different opacity assumptions. Mazzali et al. (2006) assumed an opacity, $\kappa = 0.5 Y_e \text{ cm}^2 \text{ g}^{-1}$, where Y_e is the number of electrons per baryon. We assume the authors used $Y_e = 0.46$ for iron and recalculate our Arnett-Valenti fit. With an opacity of $\kappa = 0.02 \text{ cm}^2 \text{ g}^{-1}$, we report $M_{\text{ej}} = 9.2 \pm 0.2 M_{\odot}$ and $E_{\text{K}} = (2.5 \pm 0.1) \times 10^{52} \text{ erg}$. We also note that from our fit of SN 1998bw in §2.4.2, we can see that the light-curve evolution of SN 1998bw does not match that of SN 2013dx well (see Figure 2.6); hence, the different values of M_{ej} and E_{K} are not unexpected.

We note that opacity greatly affects M_{ej} and E_{K} , but does not affect M_{Ni} . Wheeler et al. (2015) found that a conflict exists when comparing properties determined by fitting the peak (using Arnett-Valenti methods) to those determined from fitting the late-time tail (using methods from Clocchiatti & Wheeler 1997). This conflict is partially resolved by using a mean opacity determined from both peak and late-time tail parameters. Wheeler et al. (2015) find that in general, the opacity is often overestimated in the literature and the typical mean opacity is $\kappa \approx 0.01 \text{ cm}^2 \text{ g}^{-1}$. In view of this potential discrepancy, we report values

for $\kappa = 0.01 \text{ cm}^2 \text{ g}^{-1}$ ($M_{\text{ej}} \approx 21 M_{\odot}$, $E_{\text{K}} \approx 6 \times 10^{52} \text{ erg}$) and $\kappa = 0.1 \text{ cm}^2 \text{ g}^{-1}$ ($M_{\text{ej}} \approx 2 M_{\odot}$, $E_{\text{K}} \approx 6 \times 10^{51} \text{ erg}$) to draw attention to the spread in M_{ej} and E_{K} from this variable.

We also caution that numerical simulations of jet-driven SNe (e.g., González-Casanova et al. 2014; Mazzali et al. 2013; Umeda & Nomoto 2008) imply that the distribution of ^{56}Ni is likely to be highly asymmetric. The derived ejecta mass may therefore be biased by line-of-sight effects, and not representative of the total mass ejected in the explosion.

2.7 Discussion and Summary

We present extensive optical and NIR photometry of GRB 130702A/SN 2013dx spanning 1–63 d after the gamma-ray trigger, and optical spectra covering 1–33 d after the trigger. At $z = 0.145$, GRB 130702A/SN 2013dx is sufficiently close to clearly detect and model the underlying SN component that emerged a week after the burst.

We isolate the SN component and present multi-band light curves, a quasi-bolometric ($g'r'i'z'yJ$) light curve, and spectra of SN 2013dx. Detection of the broad Si II $\lambda 6355$ absorption line at velocities approaching $3 \times 10^4 \text{ km s}^{-1}$, combined with the absence of H and He features, indicates that SN 2013dx is a broad-lined SN Ic. We estimate the SN explosion parameters using the Arnett-Valenti analytical relation and infer $M_{\text{Ni}} = 0.37 \pm 0.01 M_{\odot}$, $M_{\text{ej}} = 3.1 \pm 0.1 M_{\odot}$, and $E_{\text{K}} = (8.2 \pm 0.4) \times 10^{51} \text{ erg}$.

Our analysis allows us to compare SN 2013dx with other GRB-SNe, as well as other core-collapse SNe (those of identical spectral type and not). This is of particular interest because GRB 130702A is of intermediate $E_{\gamma,\text{iso}}$, between low-luminosity and cosmological GRBs. There seems to be no clear relation between M_{Ni} , M_{ej} , or E_{K} with GRB isotropic energy (Figure 2.10), even when considering beaming corrections. The SN appears to not be imprinted with any information about the formation of the relativistic jet aside from the high photospheric velocity and lack of H and He that allows us to classify all GRB-SNe as Type Ic-BL. This is somewhat puzzling, given the predictions of a correlation between the degree of asymmetry and mass of synthesized ^{56}Ni for jet-driven explosions. We caution that the Arnett-Valenti relations we use to derive M_{Ni} assume spherical symmetry and this assumption may account for some but not all of the scatter in Figure 2.10. On the other hand, our observations do provide support for predictions that M_{Ni} should be strongly correlated with the kinetic energy of the SN itself.

Spectroscopically, SN 2013dx resembles both other GRB-SNe like SN 2006aj and SN 1998bw, as well as non-GRB SNe Ic-BL such as SN 1997ef, SN 2007I, and SN 2010ah. In terms of light curves, SN 2013dx most closely matches the evolution of SN 2012bz, associated with an intermediate GRB, but has a similar peak luminosity as SN 1998bw, associated with a low-luminosity GRB. Direct comparison of the light-curve evolution between SN 2013dx and SN 1998bw indicates that SN 2013dx has a quicker rise time than SN 1998bw. The faster rise time may suggest that SN 2013dx has a steeper distribution of ^{56}Ni in the outer layers of the star (i.e., less mixing) than SN 1998bw (Piro & Nakar 2013, Dessart et al. 2012).

Late-time observations several months after the burst can test asymmetry effectively both in photometry (Wheeler et al., 2015) and spectroscopy (Mazzali et al., 2005; Maeda et al., 2002; Milisavljevic et al., 2015). We do not have enough late-time observations of SN 2013dx to conduct these effective asymmetry tests, but we strongly encourage late-time follow-up data for GRB-SNe when possible.

Finally, we suggest two potential avenues for future study, especially with respect to GRB 130702A / SN 2013dx. Detailed numerical modeling of the SN ejecta (e.g., Mazzali et al. 2006 for SN 1998bw), specifically tailored to the light curves and spectra of SN 2013dx (instead of simply scaling results from previous simulations), should help to improve the accuracy of estimates of the fundamental SN explosions parameters. In addition, a broadband study of the afterglow emission, in particular incorporating radio wavelengths, would enable a much-improved estimate of the properties of the fastest-moving ejecta. This would greatly assist in placing GRB 130702A in the context of other relativistic explosions, specifically how the explosion energy is partitioned with respect to ejecta velocity (e.g., Margutti et al. 2014b).

Table 2.7: Observing Log

Filter	Epoch (days)	Telescope	Exp (s)	AB mag
<i>u'</i>	330.49	Keck/LRIS	203	24.50 ± 0.14
<i>g'</i>	1.17	P60	120	18.80 ± 0.04
<i>g'</i>	1.26	P60	120	18.86 ± 0.04
<i>g'</i>	2.21	P60	270	19.52 ± 0.04
<i>g'</i>	3.23	P60	450	20.02 ± 0.05
<i>g'</i>	4.19	P60	1260	20.22 ± 0.04
<i>g'</i>	5.27	P60	540	20.35 ± 0.04
<i>g'</i>	6.28	P60	540	20.31 ± 0.04
<i>g'</i>	7.20	P60	720	20.32 ± 0.04
<i>g'</i>	9.87	Liverpool	130	20.35 ± 0.33
<i>g'</i>	10.87	Liverpool	130	20.39 ± 0.35
<i>g'</i>	11.26	P60	720	20.22 ± 0.05
<i>g'</i>	11.87	Liverpool	130	20.06 ± 0.21
<i>g'</i>	12.18	P60	660	20.23 ± 0.03
<i>g'</i>	12.86	Liverpool	130	20.00 ± 0.23
<i>g'</i>	13.86	Liverpool	130	20.39 ± 0.34
<i>g'</i>	14.18	P60	720	20.31 ± 0.06
<i>g'</i>	15.18	P60	720	20.43 ± 0.07
<i>g'</i>	16.18	P60	720	20.36 ± 0.13
<i>g'</i>	17.87	Liverpool	150	20.32 ± 0.13
<i>g'</i>	19.87	Liverpool	150	20.78 ± 0.19
<i>g'</i>	21.87	Liverpool	150	20.98 ± 0.15
<i>g'</i>	23.87	Liverpool	150	21.25 ± 0.30
<i>g'</i>	27.92	Liverpool	150	21.53 ± 0.07
<i>g'</i>	29.21	P60	540	21.62 ± 0.12
<i>g'</i>	30.19	P60	1080	21.72 ± 0.09
<i>g'</i>	34.17	P60	1080	21.84 ± 0.08
<i>g'</i>	37.89	Liverpool	450	22.06 ± 0.08
<i>g'</i>	39.88	Liverpool	450	22.11 ± 0.09
<i>g'</i>	45.88	Liverpool	450	22.64 ± 0.34
<i>g'</i>	53.88	Liverpool	150	22.42 ± 0.07
<i>g'</i>	58.88	Liverpool	150	22.56 ± 0.06
<i>g'</i>	62.87	Liverpool	150	22.60 ± 0.09
<i>g'</i>	330.48	Keck/LRIS	203	23.51 ± 0.03
<i>g'</i>	632.37	DCT	1200	23.66 ± 0.04
<i>r'</i>	0.18	P48	60	17.38 ± 0.04
<i>r'</i>	0.21	P48	60	17.52 ± 0.04
<i>r'</i>	1.26	P60	360	18.66 ± 0.05
<i>r'</i>	2.16	RATIR	7600	19.23 ± 0.06
<i>r'</i>	2.21	P60	420	19.32 ± 0.04
<i>r'</i>	3.21	RATIR	5040	19.67 ± 0.04
<i>r'</i>	3.25	P60	120	19.70 ± 0.08
<i>r'</i>	4.18	P60	1320	19.97 ± 0.04
<i>r'</i>	4.21	RATIR	5360	19.88 ± 0.05
<i>r'</i>	5.21	RATIR	4960	19.95 ± 0.05
<i>r'</i>	5.27	P60	540	20.00 ± 0.04
<i>r'</i>	6.20	RATIR	4880	19.94 ± 0.05
<i>r'</i>	6.27	P60	540	20.04 ± 0.04
<i>r'</i>	7.19	RATIR	2640	19.90 ± 0.05
<i>r'</i>	7.19	P60	720	20.06 ± 0.04
<i>r'</i>	8.22	RATIR	3920	19.82 ± 0.05
<i>r'</i>	9.87	Liverpool	130	19.86 ± 0.07
<i>r'</i>	10.87	Liverpool	130	19.69 ± 0.07
<i>r'</i>	11.25	P60	660	19.82 ± 0.02
<i>r'</i>	11.87	Liverpool	130	19.73 ± 0.07
<i>r'</i>	12.18	P60	660	19.78 ± 0.04
<i>r'</i>	12.22	RATIR	2880	19.70 ± 0.04
<i>r'</i>	12.87	Liverpool	130	19.74 ± 0.08
<i>r'</i>	13.16	RATIR	1280	19.68 ± 0.05
<i>r'</i>	13.87	Liverpool	130	19.68 ± 0.10
<i>r'</i>	14.18	P60	660	19.70 ± 0.04
<i>r'</i>	14.18	RATIR	3760	19.68 ± 0.07
<i>r'</i>	15.16	RATIR	5280	19.70 ± 0.05

AB magnitudes, not corrected for Galactic extinction.

Table 2.7 – Continued

Filter	Epoch (days)	Telescope	Exp (s)	AB mag
<i>r'</i>	15.17	P60	660	19.64 ± 0.04
<i>r'</i>	15.87	Liverpool	150	19.80 ± 0.07
<i>r'</i>	16.17	P60	660	19.76 ± 0.08
<i>r'</i>	17.87	Liverpool	150	19.83 ± 0.03
<i>r'</i>	19.87	Liverpool	150	19.92 ± 0.04
<i>r'</i>	21.88	Liverpool	150	20.00 ± 0.03
<i>r'</i>	23.87	Liverpool	150	20.20 ± 0.02
<i>r'</i>	25.17	RATIR	4560	20.16 ± 0.07
<i>r'</i>	26.15	RATIR	2160	20.22 ± 0.05
<i>r'</i>	27.15	RATIR	5200	20.31 ± 0.05
<i>r'</i>	27.91	Liverpool	150	20.42 ± 0.03
<i>r'</i>	28.16	RATIR	5120	20.38 ± 0.05
<i>r'</i>	29.15	RATIR	5200	20.52 ± 0.06
<i>r'</i>	29.19	P60	540	20.49 ± 0.05
<i>r'</i>	30.18	P60	540	20.54 ± 0.06
<i>r'</i>	30.19	RATIR	3120	20.63 ± 0.06
<i>r'</i>	31.15	RATIR	3920	20.62 ± 0.15
<i>r'</i>	32.15	RATIR	4960	20.73 ± 0.06
<i>r'</i>	34.16	P60	540	20.87 ± 0.07
<i>r'</i>	35.17	RATIR	3680	20.96 ± 0.06
<i>r'</i>	37.88	Liverpool	150	21.22 ± 0.04
<i>r'</i>	39.88	Liverpool	150	21.27 ± 0.06
<i>r'</i>	41.16	RATIR	3840	21.25 ± 0.08
<i>r'</i>	45.15	RATIR	2080	21.33 ± 0.12
<i>r'</i>	45.87	Liverpool	150	21.46 ± 0.14
<i>r'</i>	46.15	RATIR	3120	21.36 ± 0.11
<i>r'</i>	47.88	Liverpool	150	21.42 ± 0.15
<i>r'</i>	53.87	Liverpool	150	21.75 ± 0.06
<i>r'</i>	58.87	Liverpool	150	21.81 ± 0.06
<i>r'</i>	62.86	Liverpool	150	21.80 ± 0.10
<i>R</i>	330.48	Keck/LRIS	200	23.26 ± 0.06
<i>r'</i>	632.39	DCT	1200	23.15 ± 0.04
<i>i'</i>	1.17	P60	120	18.42 ± 0.04
<i>i'</i>	1.26	P60	120	18.56 ± 0.06
<i>i'</i>	2.16	RATIR	7600	19.09 ± 0.07
<i>i'</i>	2.21	P60	420	19.12 ± 0.04
<i>i'</i>	3.21	RATIR	5040	19.59 ± 0.06
<i>i'</i>	3.24	P60	450	19.64 ± 0.05
<i>i'</i>	4.17	P60	1320	19.97 ± 0.06
<i>i'</i>	4.21	RATIR	5360	19.93 ± 0.06
<i>i'</i>	5.21	RATIR	4960	20.05 ± 0.12
<i>i'</i>	5.26	P60	540	20.13 ± 0.05
<i>i'</i>	6.20	RATIR	4880	20.13 ± 0.09
<i>i'</i>	6.27	P60	660	20.09 ± 0.05
<i>i'</i>	7.18	P60	660	20.17 ± 0.05
<i>i'</i>	7.19	RATIR	3280	20.07 ± 0.17
<i>i'</i>	8.22	RATIR	3920	20.10 ± 0.07
<i>i'</i>	9.87	Liverpool	130	19.93 ± 0.13
<i>i'</i>	10.87	Liverpool	130	19.86 ± 0.16
<i>i'</i>	11.17	P60	180	19.88 ± 0.11
<i>i'</i>	11.87	Liverpool	130	19.87 ± 0.15
<i>i'</i>	12.19	P60	660	19.94 ± 0.04
<i>i'</i>	12.22	RATIR	2880	19.91 ± 0.05
<i>i'</i>	12.87	Liverpool	130	19.94 ± 0.14
<i>i'</i>	13.16	RATIR	1280	19.86 ± 0.05
<i>i'</i>	13.87	Liverpool	130	20.01 ± 0.21
<i>i'</i>	14.18	RATIR	3760	19.84 ± 0.05
<i>i'</i>	14.19	P60	660	19.86 ± 0.06
<i>i'</i>	15.16	RATIR	5280	19.83 ± 0.05
<i>i'</i>	15.19	P60	660	19.77 ± 0.06
<i>i'</i>	15.87	Liverpool	150	19.91 ± 0.10
<i>i'</i>	16.19	P60	660	20.02 ± 0.10
<i>i'</i>	17.87	Liverpool	150	19.94 ± 0.07
<i>i'</i>	19.87	Liverpool	150	19.88 ± 0.05

AB magnitudes, not corrected for Galactic extinction.

Table 2.7 – Continued

Filter	Epoch (days)	Telescope	Exp (s)	AB mag
<i>i'</i>	21.87	Liverpool	150	19.97 ± 0.04
<i>i'</i>	23.87	Liverpool	150	20.09 ± 0.05
<i>i'</i>	25.17	RATIR	4560	20.04 ± 0.06
<i>i'</i>	26.15	RATIR	2160	20.09 ± 0.05
<i>i'</i>	27.15	RATIR	5200	20.15 ± 0.06
<i>i'</i>	27.91	Liverpool	150	20.18 ± 0.02
<i>i'</i>	28.16	RATIR	5120	20.21 ± 0.05
<i>i'</i>	29.15	RATIR	5200	20.30 ± 0.07
<i>i'</i>	29.22	P60	540	20.31 ± 0.06
<i>i'</i>	30.19	RATIR	3120	20.41 ± 0.07
<i>i'</i>	30.20	P60	540	20.44 ± 0.08
<i>i'</i>	31.15	RATIR	4000	20.43 ± 0.14
<i>i'</i>	32.15	RATIR	5440	20.52 ± 0.07
<i>i'</i>	34.18	P60	540	20.67 ± 0.07
<i>i'</i>	35.17	RATIR	3680	20.68 ± 0.07
<i>i'</i>	37.88	Liverpool	150	21.01 ± 0.05
<i>i'</i>	39.87	Liverpool	150	21.03 ± 0.08
<i>i'</i>	41.16	RATIR	3840	20.88 ± 0.08
<i>i'</i>	45.15	RATIR	2080	21.05 ± 0.11
<i>i'</i>	45.87	Liverpool	150	21.16 ± 0.10
<i>i'</i>	46.15	RATIR	3120	21.12 ± 0.10
<i>i'</i>	47.88	Liverpool	150	21.14 ± 0.13
<i>i'</i>	53.86	Liverpool	150	21.56 ± 0.09
<i>i'</i>	58.86	Liverpool	150	21.65 ± 0.09
<i>i'</i>	62.86	Liverpool	150	21.53 ± 0.12
<i>i'</i>	632.39	DCT	1200	23.03 ± 0.06
<i>z'</i>	2.16	RATIR	5700	18.91 ± 0.09
<i>z'</i>	2.21	P60	870	19.02 ± 0.08
<i>z'</i>	3.21	RATIR	3780	19.36 ± 0.07
<i>z'</i>	3.24	P60	840	19.43 ± 0.09
<i>z'</i>	4.19	P60	1320	19.53 ± 0.10
<i>z'</i>	4.21	RATIR	4020	19.72 ± 0.12
<i>z'</i>	5.20	P60	1020	19.84 ± 0.12
<i>z'</i>	5.21	RATIR	3720	19.84 ± 0.08
<i>z'</i>	6.20	RATIR	3660	19.94 ± 0.11
<i>z'</i>	6.26	P60	540	19.95 ± 0.12
<i>z'</i>	7.18	P60	540	20.04 ± 0.11
<i>z'</i>	7.19	RATIR	2820	19.71 ± 0.35
<i>z'</i>	8.22	RATIR	2940	19.98 ± 0.13
<i>z'</i>	9.87	Liverpool	150	20.11 ± 0.12
<i>z'</i>	10.87	Liverpool	150	19.99 ± 0.12
<i>z'</i>	11.87	Liverpool	150	20.13 ± 0.11
<i>z'</i>	12.22	RATIR	2160	19.94 ± 0.13
<i>z'</i>	12.87	Liverpool	150	20.02 ± 0.11
<i>z'</i>	13.16	RATIR	960	20.02 ± 0.12
<i>z'</i>	13.87	Liverpool	150	19.82 ± 0.13
<i>z'</i>	14.18	RATIR	2820	19.87 ± 0.12
<i>z'</i>	15.16	RATIR	3960	20.01 ± 0.10
<i>z'</i>	15.87	Liverpool	150	20.21 ± 0.20
<i>z'</i>	17.88	Liverpool	150	20.10 ± 0.08
<i>z'</i>	19.88	Liverpool	150	20.08 ± 0.05
<i>z'</i>	21.88	Liverpool	150	20.19 ± 0.06
<i>z'</i>	23.88	Liverpool	150	20.27 ± 0.04
<i>z'</i>	25.17	RATIR	3300	20.46 ± 0.14
<i>z'</i>	26.15	RATIR	1560	20.06 ± 0.13
<i>z'</i>	27.15	RATIR	3900	20.30 ± 0.09
<i>z'</i>	27.90	Liverpool	150	20.33 ± 0.07
<i>z'</i>	28.16	RATIR	3780	20.23 ± 0.09
<i>z'</i>	29.15	RATIR	3900	20.49 ± 0.10
<i>z'</i>	30.19	RATIR	2340	20.44 ± 0.15
<i>z'</i>	31.15	RATIR	2940	20.45 ± 0.11
<i>z'</i>	32.15	RATIR	4080	20.81 ± 0.15
<i>z'</i>	34.15	RATIR	3660	20.87 ± 0.12
<i>z'</i>	35.17	RATIR	2820	20.96 ± 0.14

AB magnitudes, not corrected for Galactic extinction.

Table 2.7 – Continued

Filter	Epoch (days)	Telescope	Exp (s)	AB mag
<i>z'</i>	37.87	Liverpool	150	21.15 ± 0.15
<i>z'</i>	39.87	Liverpool	150	21.33 ± 0.20
<i>z'</i>	45.86	Liverpool	150	21.41 ± 0.30
<i>z'</i>	53.85	Liverpool	150	21.27 ± 0.13
<i>z'</i>	58.85	Liverpool	150	21.60 ± 0.20
<i>z'</i>	62.85	Liverpool	150	21.85 ± 0.29
<i>z'</i>	632.41	DCT	1200	23.02 ± 0.12
<i>y</i>	2.16	RATIR	5700	18.78 ± 0.08
<i>y</i>	3.21	RATIR	3780	19.23 ± 0.08
<i>y</i>	4.21	RATIR	4020	19.53 ± 0.09
<i>y</i>	5.21	RATIR	3720	19.70 ± 0.09
<i>y</i>	6.20	RATIR	3660	19.79 ± 0.07
<i>y</i>	12.22	RATIR	2160	19.49 ± 0.10
<i>y</i>	13.16	RATIR	960	19.70 ± 0.13
<i>y</i>	14.18	RATIR	2820	19.75 ± 0.09
<i>y</i>	15.16	RATIR	3960	19.73 ± 0.11
<i>y</i>	22.16	RATIR	2340	19.85 ± 0.13
<i>y</i>	25.17	RATIR	3300	19.69 ± 0.14
<i>y</i>	26.15	RATIR	1560	20.00 ± 0.13
<i>y</i>	27.15	RATIR	3900	20.05 ± 0.09
<i>y</i>	28.16	RATIR	3780	20.01 ± 0.09
<i>y</i>	29.15	RATIR	3900	20.03 ± 0.10
<i>y</i>	30.19	RATIR	2340	20.04 ± 0.11
<i>y</i>	31.15	RATIR	2940	20.28 ± 0.12
<i>y</i>	32.15	RATIR	4080	20.00 ± 0.11
<i>y</i>	34.15	RATIR	3660	20.49 ± 0.14
<i>y</i>	35.17	RATIR	2820	20.51 ± 0.14
<i>J</i>	2.16	RATIR	6380	18.75 ± 0.09
<i>J</i>	3.21	RATIR	4230	19.22 ± 0.07
<i>J</i>	4.21	RATIR	4500	19.65 ± 0.09
<i>J</i>	5.21	RATIR	4160	19.64 ± 0.10
<i>J</i>	6.20	RATIR	4090	19.85 ± 0.10
<i>J</i>	14.18	RATIR	3150	20.07 ± 0.12
<i>J</i>	15.16	RATIR	4430	19.86 ± 0.11
<i>J</i>	27.15	RATIR	4360	19.92 ± 0.13
<i>J</i>	28.16	RATIR	4230	20.05 ± 0.12
<i>J</i>	29.15	RATIR	4360	20.23 ± 0.13
<i>J</i>	349.45	Keck/MOSFIRE	132	23.18 ± 0.32
<i>H</i>	2.16	RATIR	6380	18.60 ± 0.09
<i>H</i>	3.21	RATIR	4230	18.96 ± 0.08
<i>H</i>	4.21	RATIR	4500	19.37 ± 0.11
<i>H</i>	5.21	RATIR	4160	19.83 ± 0.12
<i>H</i>	6.20	RATIR	4090	19.89 ± 0.13
<i>K_s</i>	349.44	Keck/MOSFIRE	79	> 22.29

AB magnitudes, not corrected for Galactic extinction.

Chapter 3: GRB-DLA host counterparts

3.1 Introduction

There are several successful methods to identify galaxies in the early Universe. For example, Lyman-break galaxies (LBGs; Steidel et al. 1996) are found using the photometric drop-out technique around the Lyman-limit and have provided the first sample of $z \gtrsim 8$ galaxies (e.g. Bouwens et al. 2010; Oesch et al. 2012). Lyman- α emitters (LAE), in which hydrogen recombines after ionization by young stars, are identified at the highest redshifts with deep near-infrared observing campaigns ($z \sim 7.7$; Hiben et al. 2010; Tilvi et al. 2010; Krug et al. 2012). Because the Lyman- α ($\text{Ly}\alpha$) line is less sensitive to the overall stellar continuum, LAEs are generally lower mass systems with negligible dust (Gawiser et al., 2007; Guaita et al., 2011). Additionally, mm/sub-mm observations have opened a promising way to study galaxies at $z \gtrsim 1$ through CO molecular emission at high redshift (e.g. Daddi et al., 2009). These methods mainly probe the bright end of the luminosity function, at least at the highest redshifts, due to their strong stellar UV continuum.

Another method to identify high-redshift galaxies, while also characterizing their chemical enrichment, utilizes bright background objects like high-redshift quasars (QSO), gamma-ray burst (GRB) afterglows, or, even more recently, extended back-

ground galaxies (Cooke & O’Meara, 2015; Mawatari et al., 2016) to identify absorption-line systems. These detections depend only on the gas cross-section and therefore are less sensitive to the luminosity of the associated object (an observing bias that affects every high-redshift galaxy survey). Specifically, diffuse gaseous clouds in the Universe are primarily described by their neutral hydrogen column density (N_{HI}). Recent surveys have demonstrated that Damped Lyman- α systems (DLAs, see Wolfe et al. 2005), characterized by $N_{\text{HI}} \geq 2 \times 10^{20} \text{cm}^{-2}$, contain $\geq 80\%$ of the neutral gas available for star formation (P  roux et al., 2003; Prochaska et al., 2005; Prochaska & Wolfe, 2009; Noterdaeme et al., 2009, 2012a; Zafar et al., 2013). At $z = 2 - 3$, they contain enough gas to account for a significant fraction (20-50%) of stellar mass in all galaxies (Storrie-Lombardi & Wolfe, 2000; Wolfire et al., 2003; O’Meara et al., 2007). Most importantly, they provide a powerful independent check on sophisticated models of galaxy formation which also include the effects of stellar and supernovae feedback (e.g. Bird et al., 2014; Rahmati et al., 2015).

Some suggested scenarios to explain the nature of high-redshift DLA galaxies include rapidly-rotating proto-galactic disks (Prochaska & Wolfe, 1997; Wolfe & Prochaska, 1998; Genzel et al., 2006; F  rster Schreiber et al., 2009), low surface brightness galaxies (Jimenez et al., 1999), faint and small gas-rich dwarf galaxies (Tyson, 1988), compact galaxies (Nagamine et al., 2007), dwarf irregulars (Dessauges-Zavadsky et al., 2007), or gaseous haloes of Lyman break galaxies (Fynbo et al., 1999; M  ller et al., 2002). There is a general consensus that the major contribution to the DLA population at $z \sim 3$ comes from haloes with virial masses of $10^{10-12} M_{\odot}$ (Cooke et al., 2006; Barnes & Haehnelt, 2009; Font-Ribera et al., 2012). Also, Rahmati &

Schaye (2014) found that most DLAs at those redshifts are hosted by haloes with masses around or less than $10^{10}M_{\odot}$ (see top-right panel of Figure 6 in that paper) and, more recently, Srianand et al. (2016) suggested a predominant contribution, at high-redshift, of DLAs that are more compact than modern disk galaxies.

To understand both the nature and evolution of the DLA population it becomes critical to identify and characterize the galaxies associated with DLAs, e.g. measuring their stellar mass, metallicity, size, and star-formation. Understanding the types of galaxies DLAs represent will allow us to constrain which models better describe the DLA population. There are thousands of DLAs identified from absorption-line studies, thanks to the Sloan Digital Sky Survey (Eisenstein et al., 2011) and the BOSS surveys (Dawson et al., 2013). We can measure the neutral gas and metal content from absorption-lines, however, finding the DLA host galaxies that actually produced the identified features has been difficult, particularly at high redshift and/or at small impact parameters.

Thus far there have only been 13 QSO-DLA confirmed galaxy counterparts. This small sample spans redshifts of $z \sim 0.9 - 3.4$ and impact parameters of $\sim 1 - 25$ kpc (Møller & Warren, 1993; Møller et al., 2002; Weatherley et al., 2005; Fynbo et al., 2011; Noterdaeme et al., 2012b; Péroux et al., 2012; Krogager et al., 2012; Bouché et al., 2013; Jorgenson & Wolfe, 2014; Péroux et al., 2016). The majority of these DLA galaxies were found by taking spectra with multiple slit overlays. This method has been successful but suffers from a strong bias towards small impact parameters as this is where most of the slits overlap. Moreover, the bright QSO precludes exploration at very small impact parameters. It is difficult to quantify

selection biases with this method as non-detection statistics are not reported. Another interesting possibility is to use the Atacama Large Millimeter/submillimeter Array (ALMA) to map out CO in QSO-DLAs. Neeleman et al. (2016) successfully detected molecular emission from a galaxy along the projected background of a quasar with ALMA.

An independent method to identify host galaxies is the double-DLA method where a second DLA system along the line-of-sight of the QSO-DLA acts as a blue filter for the QSO (O’Meara et al., 2006). This method has been successful in placing limits on star formation rates (SFRs) but has so far yielded few detections (Fumagalli et al., 2015).

Finally, one can target DLAs that are identified *within GRB host galaxies* (GRB-DLAs): GRBs are extremely bright sources and can be seen up to $z \sim 9$ (Tanvir et al., 2009; Salvaterra et al., 2009; Cucchiara et al., 2011). Their bright afterglows enable the identification of the Ly α profile (which provides accurate H I column density measurement) as well as metal lines at the same redshift of the GRB host (different with respect to QSOs, where the DLA is usually at lower-redshift). There are three key advantages of using GRB- DLAs: 1) GRBs are very bright sources, providing exquisite high S/N spectra even at the highest redshifts; 2) the simple power-law continuum of the afterglow emission simplifies line identification and line profile fitting with respect to the more complex QSO underlying emission; 3) the afterglow emission fades away after a few days of the explosion, enabling *direct* imaging galaxies at small impact parameters ($\lesssim 1 - 3$ kpc, as shown by Blanchard et al., 2016) which are often identified as the GRB host galaxies. Schulze et al.

(2012) demonstrated this method with a dedicated campaign to identify the galaxy counterparts for GRB-DLAs and sub-DLAs at $z = 2 - 3.6$. The authors successfully detected a GRB-DLA counterpart for GRB 070721B.

The main drawback with this method is that the transient nature of GRBs often makes it difficult to obtain spectra before the GRB afterglow has faded. Consequently, it is challenging to assemble a large sample of GRB-DLAs; however, Cucchiara et al. (2015) has reported a sample of 76 confirmed GRB-DLAs and GRB sub-DLAs (for which $\log N_{\text{HI}} < 20.3$). In the following sections we will use this sample as a starting point to identify and characterize the galaxy counterparts of these DLAs and sub-DLAs. Our compilation represents a factor of $\gtrsim 3$ increase in the number of identified DLA galaxies to date.

The paper is divided as follows: in §3.2 we describe the GRB-DLA sample and how it compares to other GRB hosts or QSO-DLA samples, in §3.3.1 we report star formation rates and stellar masses from our GRB-DLA counterparts and investigate if there is any correlation between SFR and either redshift or HI column density, in §3.3.2 we examine the relationship between star formation rate surface density and HI gas surface density to try to understand how star formation efficiency changes with redshift and metallicity and we compare our star formation efficiencies with galaxies in the local Universe, in §3.4 we report enrichment times to understand how metals are formed in these counterparts, and in §3.5 we summarize our results.

Throughout this paper we assume a Λ CDM model with $H_0 = 69.6 \text{ km s}^{-1} \text{ Mpc}^{-1}$, $\Omega_m = 0.286$, and $\Omega_\Lambda = 0.714$ (Bennett et al., 2014). All magnitudes are in the AB system (Oke & Gunn, 1983) and quoted uncertainties are 1σ (68%) confidence in-

tervals unless otherwise noted.

3.2 Sample and data reduction

3.2.1 Sample

We use the GRB-DLA sample described in Cucchiara et al. (2015) as a starting point for our search for GRB-DLA counterparts. This sample is comprised of 76 GRB host galaxies: 59 confirmed GRB-DLAs and the remaining 17 objects are either GRB sub-DLAs or they only have either upper or lower limits on N_{HI} (the latter are likely sub-DLAs or Lyman limit systems). We conduct a literature search for photometric observations of each associated GRB host galaxy (see Table 3.1 for individual observation references) and supplement these observations with data from the Large Monolithic Imager (LMI) on the Discovery Channel Telescope (DCT). All of the magnitudes are converted to AB magnitudes using Blanton & Roweis (2007) and are corrected for Galactic extinction using the dust map from Schlafly & Finkbeiner (2011). The photometry of the host galaxies is taken weeks after the GRB trigger to ensure that the GRB afterglow contribution is negligible. The majority of our sample is too faint to detect spectral emission lines, however, Blanchard et al. (2016) performed a statistical analysis of 105 long GRBs with deep *HST* imaging with 1'' positioning and found that 90% of long GRBs have physical offsets of $\lesssim 5$ kpc which makes chance associations of our sample improbable. Additionally, one expects $\lesssim 0.5$ DLA (Noterdaeme et al., 2012a; Crighton et al., 2015) and ~ 1 Lyman limit system (Prochaska et al., 2010; Ribaldo et al., 2011; O’Meara

et al., 2013; Fumagalli et al., 2013) per line-of-sight at $z = 3$ which suggests that these are not interloping DLA or Lyman limit systems.

Out of 59 GRB-DLAs, 45 have GRB host galaxy photometric detections in at least one band or we are able to measure photometric limits in the rest-frame ultraviolet (UV) which directly traces star-formation. We do not use any photometry that is below the Lyman limit in the host galaxy rest-frame and our SED modeling accounts for IGM absorption (described in detail in §3.3.1.1) for the three GRB-DLA and one GRB sub-DLA host galaxies that have photometric detections in the rest-frame Ly α forest. Throughout our paper we refer to these 45 GRB-DLAs as our sample (Table 3.1). Our sample has a median $z = 3.2$ and $\log N_{\text{HI}} = 21.6$.

For completeness we also include 12 sub-DLAs in Table 3.2.

3.2.2 LMI data reduction

We use LMI to add 5 upper limits and 1 detection of DLA galaxy counterparts. The LMI data were detrended with a custom IRAF¹ pipeline. Individual frames were astrometrically aligned with **Scamp** (Bertin, 2006) and coadded using **SWarp** (Bertin et al., 2002). We performed aperture photometry on the resulting coadded images using **SExtractor** (Bertin & Arnouts, 1996) with a static 5 pixel (1.2") radius aperture, which is typical of the average seeing. The resulting magnitudes were calibrated against the Sloan Digital Sky Survey (SDSS; Aihara et al. 2011) fields.

¹IRAF is distributed by the National Optical Astronomy Observatories, which are operated by the Association of Universities for Research in Astronomy, Inc., under cooperative agreement with the National Science Foundation.

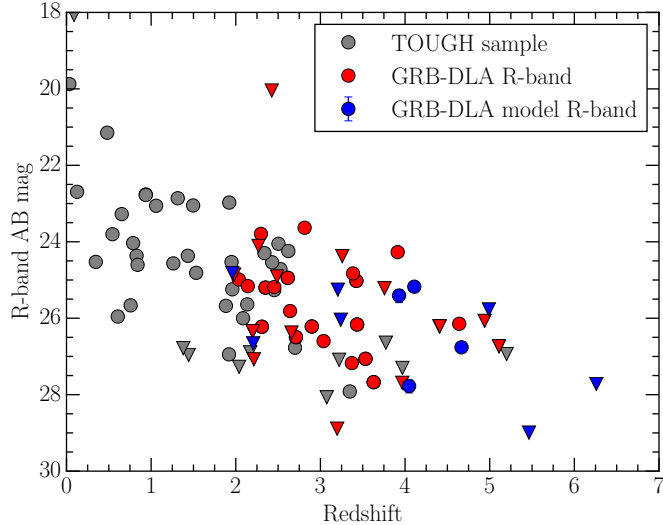


Figure 3.1 Distribution of R-band observations of GRB host galaxies with redshift; all data have been corrected for Galactic extinction. Downward triangles are upper limits and circles are detections. Red points are from R, r' , F606W observations, using a flat SED to calculate R-band AB magnitude. Blue points are from using scaled SEDs from MAGPHYS (§3.3.1.1) to determine R-band AB magnitudes (see text for details).

3.2.3 Comparison to other samples

We compare the observer frame R-band and redshift distribution of our sample with The Optically Unbiased Gamma-ray burst Host (TOUGH) survey (Hjorth et al., 2012, see Figure 3.1). Our DLA sample covers the $z \sim 2 - 6.3$ redshift range and a similar R-band luminosity distribution (which is usually a good proxy for the host rest-frame UV luminosity) as TOUGH. In the cases where R-band is not available but we have r' or F606W observations, we convert to R-band assuming a flat SED between these three filters. Additionally, 11 GRB-DLAs do not have R-band, r' -band, or F606W observations (either detections or limits). For these GRB-DLAs we scale the modeled SEDs (see §3.3.1.1) from our small sample of eight GRB-DLA counterparts with extensive photometric coverage to the observed

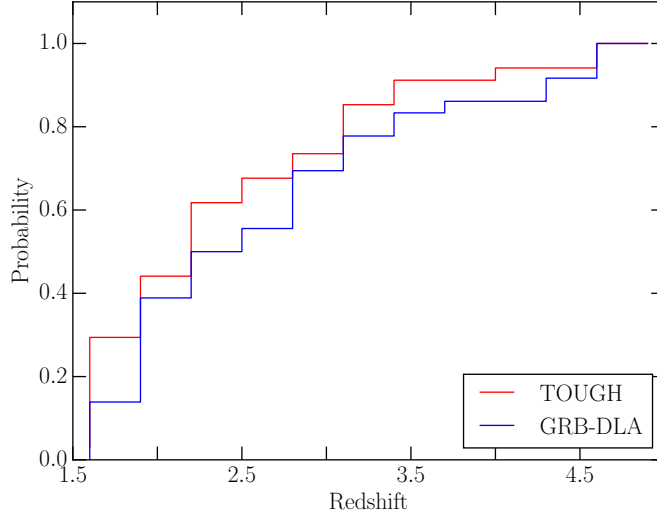


Figure 3.2 Cumulative redshift distribution of our GRB-DLAs compared with that of the TOUGH sample. 2-sample Kolmogorov-Smirnov tests show that our sample is consistent with being drawn from the same redshift distribution as TOUGH.

magnitude and present the median scaled R-band value of those eight SEDs in Figure 3.1. Note that if the standard deviation of the R-band value from those eight SEDs was larger than the median we report it as an upper limit. Also, at $z \gtrsim 4$ the R-band traces flux emerging at or below the Ly α line (1216 Å rest-frame), therefore these values are more uncertain since they are subject to additional absorption.

After we remove objects from our sample that are in the TOUGH survey, we run a 2-sample Kolmogorov-Smirnov test on the redshift distribution (see Figure 3.2) over the overlapping redshift range of $z \sim 2-5$. The p -value of 0.78 is consistent with our GRB-DLA counterpart sample and the TOUGH survey being drawn from the same GRB host population. To the extent that TOUGH is a representative sample of the overall GRB host population, this means that the GRB-DLAs hosts are also representative of the overall GRB host population.

We also compare our sample throughout this paper to the Fumagalli et al.

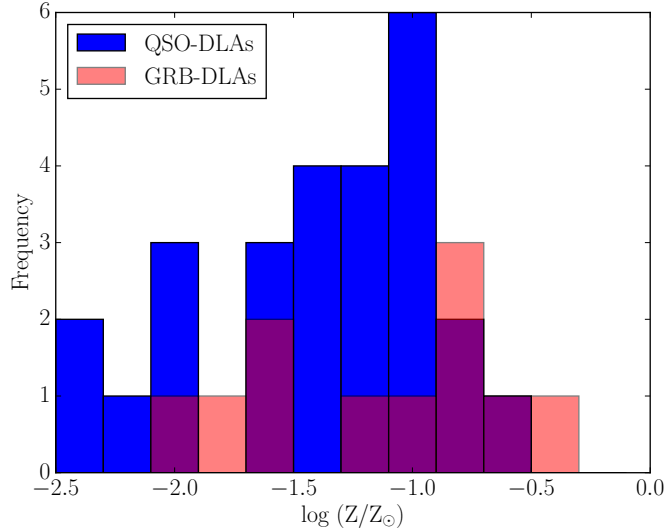


Figure 3.3 The metallicity distribution of our sample compared with the Fumagalli et al. (2014) double-DLA sample. The majority of our absorption-line metallicity measurements are lower limits which we do not include in this histogram.

(2010) sample of QSO-DLAs studied with the double-DLA technique which has no selection bias towards large impact parameters. Our sample (which covers the $N_{\text{HI}} = 10^{20.4-22.7} \text{cm}^{-2}$ range) represents an extension of the work by Fumagalli et al. (2015), which probes mainly lower column densities ($N_{\text{HI}} = 10^{20.2-21.2} \text{cm}^{-2}$), providing further insights on the nature of the overall DLA counterpart population (see Prochaska et al., 2007). We perform a Kolmogorov-Smirnov test on the column density distribution over the overlapping column density range of $N_{\text{HI}} = 10^{20.2-21.2} \text{cm}^{-2}$ and the p -value of 0.74 is consistent with our GRB-DLA counterpart sample and the QSO-DLA sample being drawn from the same DLA population for that range of column densities. However, we caution that these samples may not be from the same population for reasons discussed throughout the paper and because this p -value suffers from problems associated with small number statistics.

Unfortunately, it is difficult to compare our GRB-DLA metallicities with other

samples because the majority of our metallicities are lower limits. Instead we only plot a histogram of our 11 GRB-DLA metallicity detections compared to the double-DLA sample (Figure 3.3); our sample covers a similar spread in metallicity as the double-DLA sample with the exception of a handful of metal rich systems above $\log(Z/Z_{\odot}) > -1$. For more detailed analysis of our sample’s metallicity distribution and a direct comparison with the largest compilation of QSO-DLAs to date we direct the reader to the extensive published work by Cucchiara et al. (2015), Rafelski et al. (2012), and Rafelski et al. (2014).

3.3 Star Formation

Star formation is correlated with the neutral gas content in a galaxy, but it is not completely clear which phase has a stronger causal connection with star formation: atomic, molecular, or total hydrogen (Schmidt, 1959; Kennicutt, 1998; Krumholz et al., 2009; Rafelski et al., 2011; Elmegreen, 2015; Rafelski et al., 2016). Here we use atomic neutral hydrogen column densities measured from the damped Lyman- α absorption feature and assume that the molecular hydrogen has a negligible contribution. This is supported by the small ($\sim 1\%$) molecular hydrogen detection rate in a blind and uniformly selected DLA survey (Jorgenson et al., 2013, 2014) and by targeted surveys (Noterdaeme et al., 2008).

Additionally, it is rare to detect molecular absorption features in GRB afterglow spectra (supported by the few H_2 measurement along few GRB lines of sights, e.g., Prochaska et al. 2009; Krühler et al. 2013; D’Elia et al. 2014; Stanway et al.

2015) due to the unavailability of the required high-resolution instruments and blue spectral coverage.

We caution that the GRB afterglow line-of-sight is probing a much smaller area (\sim parsec scale) of the much larger galaxy (\sim kiloparsec scale); however, if GRBs occur in star-forming regions we expect them to encounter molecular hydrogen whereas the QSO may be outside of the star-forming region.

We calculate star formation rates (SFRs) from rest-frame UV luminosities (see Section §3.3.1) and investigate if there is any correlation with redshift or the ISM metallicities (as determined by the absorption features). We then calculate star formation rate surface densities and HI surface densities to explore star formation efficiencies (Section §3.3.2), and finally we examine possible redshift and absorption metallicity trends in comparison with the Kennicutt-Schmidt relation at both local, $z = 0$, and at higher redshifts (from cosmological simulations).

3.3.1 Star Formation Rates

We calculate SFRs using three methods. The first and preferred method is SED modeling using MAGPHYS described in §3.3.1.1. We limit the use of SED modeling to GRB-DLA counterparts that have photometric detections in at least three separate bands which is the minimum for MAGPHYS to converge to a reasonable SED fit (although with large parameter errorbars in cases with few photometric points). The second method is using single band detections corresponding to rest-frame UV bandpass to calculate rest-frame UV SFR (see §3.3.1.2). For consistency

we compare SFRs based on the first two methods: SFR values from these two methods reasonable agree with each other usually within a factor of two, but in rare cases may vary by a factor of five most likely due to different accounting of dust extinction. Generally the single band SFRs are in agreement or are slightly lower than those derived from SED modeling with MAGPHYS.

If we are unable to use either of the first two methods and we have at least one detection in another filter, we scale the SEDs from the DLA counterparts that were fit with the first method to match the detected host galaxy flux. We then use the scaled SEDs to estimate the rest-frame UV flux and use the median and standard deviation of the scaled SEDs to calculate the rest-frame UV SFR. Finally, if there are no detections in any band but there are upper limits in the rest-frame UV band, we calculate SFR upper limits using the second method.

Photometric measurement were made using aperture photometry technique, using the Hubble Space Telescope (HST) point spread function (PSF) for GRB-DLA counterparts with HST data and the DCT 1.2" PSF for the ground-based data (corresponding to ~ 2 and ~ 17 kpc diameter apertures respectively). The large difference in apertures comes from the fact that HST is able to resolve the host galaxy. We assume that the light from unresolved sources is solely from the host galaxy and background sky.

All SFRs are calculated from dust-corrected observations unless otherwise stated. The host extinction, A_V , is taken either from SED models or from GRB afterglow measurements using a Small Magellanic Cloud (SMC)- like extinction law which has been shown to best depict the GRB explosion environment (e.g. Schady

et al., 2012).

We assume the host extinction is the same as the GRB line-of-sight extinction which Perley et al. (2013) has shown is fairly consistent within a factor of 2-3. If the host extinction is an upper limit, we use that value in all dust-corrected calculations and report SFR upper limits. In Table 3.1 we report these GRB-DLAs with SFR error estimates but treat these as SFRs upper limits in all plots using dust-corrected SFRs. Our host extinction is in general higher than the $A_V \lesssim 0.1$ reported for DLAs in the SDSS survey for our sample’s column densities (Murphy & Bernet, 2016). This may likely be because GRB-DLAs are found at smaller impact parameter of $\lesssim 5$ kpc (Blanchard et al., 2016) than the general DLA population of 1 – 25 kpc (Fumagalli et al., 2015) or more simply because our DLA sample traces in general metal rich, and likely dust rich, systems (for example, see correlation between $E(B - V)$ and metal lines equivalent widths in Murphy & Bernet, 2016).

3.3.1.1 SED fitting Star Formation Rate

We use MAGPHYS with the HIGHZ extension (da Cunha et al., 2008, 2015), to model the host galaxy SEDs from photometry. MAGPHYS models templates to the data and returns a SED with fitted parameters which include SFR, stellar mass (M_*), dust mass (M_{dust}), and A_V . This particular package is well suited for $z > 1$ galaxies and takes into account bursty star formation which is appropriate for GRB host galaxies as suggested by Hunt et al. (2014). MAGPHYS uses a continuous model of star formation with superimposed random bursts that happen at equal

probability at all times up to the age of the galaxy. The probability is set such that 50% of the galaxies within the library have had a burst of star formation within the past 2 Gyr with bursts lasting $\sim 10^7 - 10^8$ years. MAGPHYS also accounts for IGM absorption and uses a Gaussian distribution centered around the mean IGM effective absorption from Madau (1995) for each model template.

We only select objects that have at least three photometric detections in order to break some parameter degeneracy and then include, if available, upper limits. We have nine GRB-DLAs that fit this criterion; however, GRB 080607 returns an unconstrained SFR and M_* . This particular host galaxy has an extremely high host extinction and HI column density that is atypical of the majority of galaxies (Wang et al., 2012; Perley et al., 2011; Chen et al., 2010; Prochaska et al., 2009).

3.3.1.2 Single band UV Star Formation Rate

We use the relations for UV luminosities from Savaglio et al. (2009) to determine SFR from a single photometric band:

$$\text{SFR}_{1500} = 1.62 \times 10^{-40} \frac{L_{1500,\text{corr}}}{\text{ergs}^{-1}\text{\AA}^{-1}} \text{M}_{\odot}\text{yr}^{-1} \quad (3.1)$$

$$\text{SFR}_{2800} = 4.33 \times 10^{-40} \frac{L_{2800,\text{corr}}}{\text{ergs}^{-1}\text{\AA}^{-1}} \text{M}_{\odot}\text{yr}^{-1} \quad (3.2)$$

$$\text{SFR}_{3600} = 5.47 \times 10^{-40} \frac{L_{3600,\text{corr}}}{\text{ergs}^{-1}\text{\AA}^{-1}} \text{M}_{\odot}\text{yr}^{-1} \quad (3.3)$$

Equations 3.1-3.3 were derived from samples with simultaneous H α and UV detection suitable for GRB host galaxies and are for dust-corrected rest-frame UV luminosities. In Figure 3.4 we present only dust-uncorrected rest-frame UV luminosities to directly compare with Fumagalli et al. (2015), but in all other figures and tables we present dust-corrected rest-frame UV SFRs. We note that other objects that we compare with in this paper use H- α to SFR conversions from Kennicutt (1998) (e.g. Fumagalli et al. 2015 and Rafelski et al. 2016): direct comparison to Savaglio et al. (2009) can result in a difference of a factor of $\lesssim 2$ in SFRs (which includes factors for different initial mass functions).

To determine rest-frame UV SFR, we consider observations redward of the rest-frame Ly α line and from filters that have rest-frame effective wavelengths within 250Å of 1500Å, 2800Å, or 3600Å when we use these relations. We have 12 GRB-DLAs with rest-frame UV detections (four of which have A_V upper limits so we list the SFRs as upper limits) and 12 GRB-DLAs with rest-frame UV limits.

Additionally, we have another 12 GRB-DLAs that have detections redder than the rest-frame UV (one of which has an A_V upper limit so we list the SFR as an upper limit). We use the scaled SEDs from the eight GRB-DLAs fit with MAGPHYS (we do not include GRB 080607 in this fit for reasons described in §3.3.1.1) and calculate the SFR using Eq. 3.1-3.3 for the closest wavelength to our rest-frame observed effective wavelength. We report the median and standard deviation SFR of these eight scaled SED in Table 3.1. We also find that our SFR measurements are in good agreement with literature values (e.g. SHOALS sample; Perley et al. 2013).

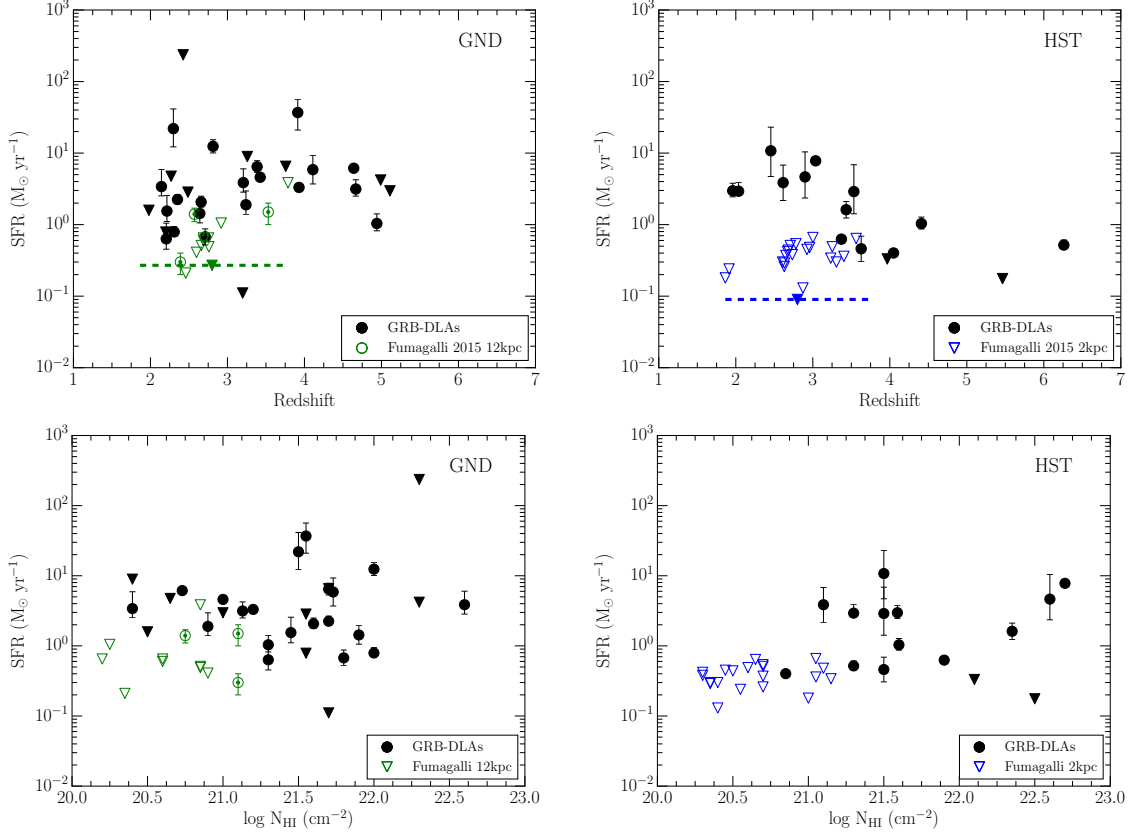


Figure 3.4 Comparing SFRs in our sample (black points) with Fumagalli et al. (2015) double-DLA SFRs (green/blue unfilled points) for both ground-based and *HST* data. Both datasets are uncorrected for dust for direct comparison. Triangles represent upper limits. Our sample uses the DCT $1.2''$ PSF (~ 17 kpc diameter) apertures for ground-based data and the *HST* PSF (~ 2 kpc diameter) apertures for *HST* data. (*top left*) Ground-based SFRs vs. redshift. There are three double-DLA detections, but one may be contaminated by the QSO (see Fumagalli et al. 2015 for details). The dashed green line is a deep limit from a composite image. (*top right*) *HST* SFRs vs. redshift. The dashed blue line is a deep limit from a composite image. (*bottom left*) Ground-based SFRs vs. HI column density. (*bottom right*) *HST* SFRs vs. HI column density.

3.3.1.3 DLA host Star Formation Rates

In Figure 3.4 we compare the dust-uncorrected SFRs with the dust-uncorrected SFR detections and limits derived by Fumagalli et al. (2015). Similar to this study, we also take full advantage of our large dataset and probe *in situ* DLA counterpart

SFRs within compact (~ 2 kpc using *HST* data) and more extended regions (~ 17 kpc using our ground-based observations). The majority of our sample has generally higher SFRs than the double-DLA limits, however, in some cases we obtain SFRs similar to the double-DLA limits both from ground-based and *HST* observations (downward triangles). This result displays the effectiveness of targeting GRB-DLA counterparts: not only is our DLA detection rate higher than Fumagalli et al. (2015), but our DLAs (when we combine ground and HST data) span a larger range of both redshift and column densities and trace intrinsic SFR over four orders of magnitude ($10^{-1} - 10^2 M_{\odot}/\text{yr}$).

Nevertheless, some DLA counterparts identified along QSOs have measured SFRs with $1 - 30 M_{\odot}\text{yr}^{-1}$ (see Fumagalli et al. 2015 and references within). It may be that it is more difficult to detect these high SFR DLAs along QSOs using an unbiased impact parameter survey as we mentioned in §3.1 or they may be from an entirely different counterpart population.

We caution that SFRs of DLAs within GRB hosts may be skewed towards higher values than the general DLA population because our sample is taken from long-duration GRBs which are known to be associated with the evolution of massive stars (see Woosley & Bloom (2006) for review) and are therefore associated with galaxies which have higher specific SFRs (Japelj et al., 2016).

Recent work by Perley et al. (2016b) has shown that the $z \gtrsim 2$ GRB host population seems to be consistent with the general cosmic star-formation rate, strengthening the idea that our DLA sample may be an important complement to our current understanding of the nature of DLAs.

Also, DLA counterpart SFRs have been predicted to be higher for higher column densities and higher metallicities (Krumholz et al., 2009; Gnedin & Kravtsov, 2010; Rafelski et al., 2011; Noterdaeme et al., 2014; Rahmati & Schaye, 2014; Rafelski et al., 2016). Our SFRs appear to be independent of column density in Figure 3.4: the 5 detections (including both ground and HST data) with $N_{\text{HI}} \leq 10^{21} \text{cm}^{-2}$ have similar SFRs of those with high HI column densities and Rahmati & Schaye (2014) simulations show that only 5% of galaxies with $N_{\text{HI}} = 10^{20-21} \text{cm}^{-2}$ have SFRs $> 10 M_{\odot} \text{yr}^{-1}$. Again, we caution that SFR is a global measurement of the host counterpart whereas HI column density is measured along the line-of-sight of the GRB afterglow and there may be some scatter in the line-of-sight measurement compared to the average DLA HI column density. Since the majority of our metallicity measurements are lower limits it is difficult to determine if metallicity plays an important role, if any at all, as presented in some cosmological simulations (Rahmati et al., 2016).

We compare our distribution of SFRs within $z = 2-4$ and $N_{\text{HI}} = 10^{21.5-22} \text{cm}^{-2}$ to simulation results from Rahmati & Schaye (2014) at $z = 3$ with the same N_{HI} range. Our sample has a total of 15 objects that meet these criteria and $33\% \pm 8\%$ of them have SFRs $< 1 M_{\odot} \text{yr}^{-1}$ where we assume the error is primarily poissonian. This number is slightly lower than the predicted 45% by Rahmati & Schaye (2014). While the number of GRB-DLAs in this comparison is still small, future and more complete GRB-DLAs surveys (like the SHOALS survey) will provide more accurate tests for cosmological simulations and the conversion of neutral gas into stars (e.g. stellar mass).

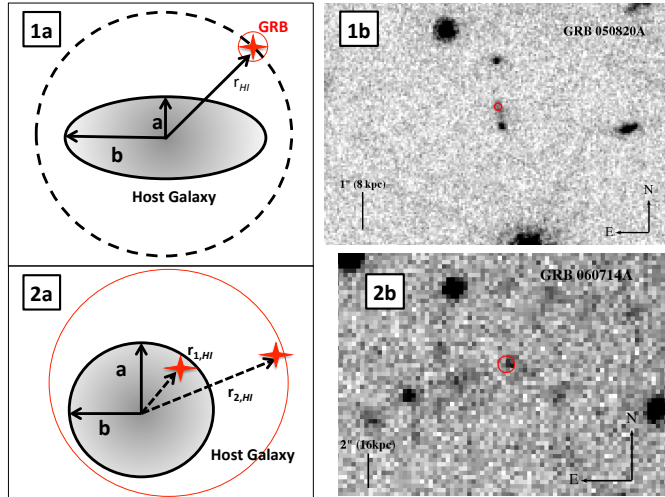


Figure 3.5 (*top left, 1a*) Ideal case where the GRB, and therefore the HI gas, is extremely well localized (red circle is localization error) and can be identified relative to the host galaxy. (*top right, 1b*) An observed case, GRB 050820A, close to the top-left idealized configuration. The GRB-DLA is localized to sub-arcsec precision (red circle) from rapid follow-up of the afterglow with *HST* and the DLA galaxy has been resolved using *HST*. (*bottom left, 2a*) Realistic case where the GRB, and therefore the HI gas, has a large error circle (red circle) that can place the GRB within the host galaxy or on the outskirts. (*bottom right, 2b*) An observed example, GRB 060714A, close to the bottom-left realistic configuration. The GRB is localized to $\lesssim 1''$ (red circle) and, although observed with Keck, the host galaxy is unresolved.

It is also evident from our results that the DLA counterpart SFRs appear to be independent of redshift and our detections are all above the double-DLA upper limits for both the ground-based and the *HST* observed GRB-DLAs, although the higher SFRs measured in the ground data may be affected by unresolved part of the GRB hosts (especially at high- z). In fact, as pointed out by Fumagalli et al. (2015), resolving the exact location of the emission of the DLA counterparts plays a critical role in our understanding of the DLA properties (see Figure 3.5), and only more *HST* data, in combination with more accurate GRB afterglow localization will enable precise DLAs *in situ* SFR measurements. We note, for our current sample, that the probability of chance association with *HST* are typically $\lesssim 0.05$ so it is very

unlikely that these are interloping galaxies (Blanchard et al., 2016), but are indeed region of star-formation within the GRB host (Figure 3.5, panels 1a and 1b).

3.3.2 Kennicutt-Schmidt relation

The Kennicutt-Schmidt relation (KS-relation) connects the available neutral hydrogen gas surface density to form stars (Σ_{HI}) to the actual measured star formation rate surface density (Σ_{SFR}). The KS-relation has been extensively studied in the local Universe (Bigiel et al., 2008, 2010; Bolatto et al., 2011; Elmegreen, 2015). As we mentioned previously we only consider the atomic hydrogen gas content since the molecular hydrogen gas has a negligible contribution at these HI column densities. This scenario may change with redshift, metallicity, or the actual regions in which the SFR is measured - core vs. outskirts of galaxies (e.g. Glover & Clark, 2012; Krumholz, 2012, 2013; Rafelski et al., 2016).

3.3.2.1 Surface Density Estimates

In order to measure Σ_{HI} , which is estimated *along the line-of-sight of the GRB*, we assume that the neutral gas is equally distributed across the entire PSF used for determining our SFR density. Figure 3.5 shows the idealized case (panel 1a) where the GRB is well localized and the host galaxy is resolved. We include an observed example of this idealized case (panel 1b) for the DLA galaxy identified in the *HST* image of GRB 050820A (cigar shaped with bright nucleus to the south; see Blanchard et al. 2016 for compilation of GRB host galaxy morphologies): the

GRB location is identified with sub-arcsec precision due to rapid follow-up of the afterglow with *HST* (red circle in 1a and 1b panels), and is in the outskirts of the host galaxy (at radius r_{HI}). Moreover, the N_{HI} column is measured through the same environment (which may vary at smaller impact parameters).

However, in general, due to the high-redshift nature and the quality of our data, we encounter a less ideal scenario, as shown in Figure 3.5 panels 2a and 2b. The uncertainty in the GRB localization, despite being often $\lesssim 1''$ ($1''$ is $\sim 6-9$ kpc for $z = 2-6$), combined with the unresolved host morphology do not allow us to accurately measure Σ_{HI} and Σ_{SFR} . In particular, as evident in panel 2a, the uncertainty in the GRB localization (red circle) makes it difficult to determine the actual neutral hydrogen line-of-sight ($r_{1,HI}$ and $r_{2,HI}$ are equally viable, but clearly probe two very different environments).

In order to be consistent with the local observed KS-relation and the higher- z theoretical models, we calculate Σ_{SFR} using our dust-corrected SFR calculated in §3.3.1 and the area covered by the unresolved ground-based aperture ($1.2''$ radius aperture) around the GRB location, which correspond to a circular area of ~ 17 kpc diameter for $z = 2 - 6$ (astropy's FlatLambdaCDM; Astropy Collaboration et al. 2013), for all the objects in our sample. While this area decreases the Σ_{SFR} for our resolved *HST* objects by a factor of ~ 70 , this allows us to be consistent when we compare both our resolved and unresolved observations to other samples and models.

Furthermore, in this context we derive the atomic gas (HI) surface density, Σ_{HI} , directly from the DLA line-of-sight neutral hydrogen column density as shown

by Lanzetta et al. (2002) and Hopkins et al. (2005) even though Σ_{HI} and Σ_{SFR} are measured over different scales, the KS-relation is, on average, still valid (see also, e.g., Zwaan & Prochaska, 2006; Wolfe & Chen, 2006; Rafelski et al., 2011, for the limitations of such approximation). This is clearly an oversimplification, but it is consistent with the analyses from other SF laws and cosmological simulations. Note that we do not include GRB-DLAs that have no A_V measurements as the dust-corrected SFR measurements are usually lower limits.

3.3.2.2 Comparison with star formation laws & simulations

With these caveats in mind, and in order to be consistent with previous works, we overplot the local Kennicutt-Schmidt relation of $\Sigma_{\text{SFR}} = K(\frac{\Sigma_{\text{HI}}}{\Sigma_0})^\beta$ with $K = (2.5 \pm 0.7) \times 10^{-4} \text{M}_\odot \text{yr}^{-1} \text{kpc}^{-2}$, $\beta = 1.40 \pm 0.15$, and $\Sigma_0 = 1 \text{M}_\odot \text{pc}^{-2}$ (Kennicutt, 1998) in Figure 3.6 along with a dynamical star formation law for spiral and irregular galaxies (Elmegreen, 2015) and a star formation law at $z \sim 3$ from cosmological simulations (Gnedin & Kravtsov, 2010). Note that the Gnedin & Kravtsov (2010) SFR surface density is shown for the total neutral hydrogen gas (dash blue line), only molecular hydrogen gas (dotted-dash blue line), and only atomic hydrogen gas (solid blue line). We also, in the two panels, color code our points based on GRB afterglow absorption-line metallicity (left) and redshift (right). The interpretation of this plot is clearly non-trivial: a large fraction ($\sim 50\%$) of our detected DLA counterpart falls in the predicted local K-S relation (shaded area), while some very low metallicity systems are below. Moreover, the presence of our upper limits seem

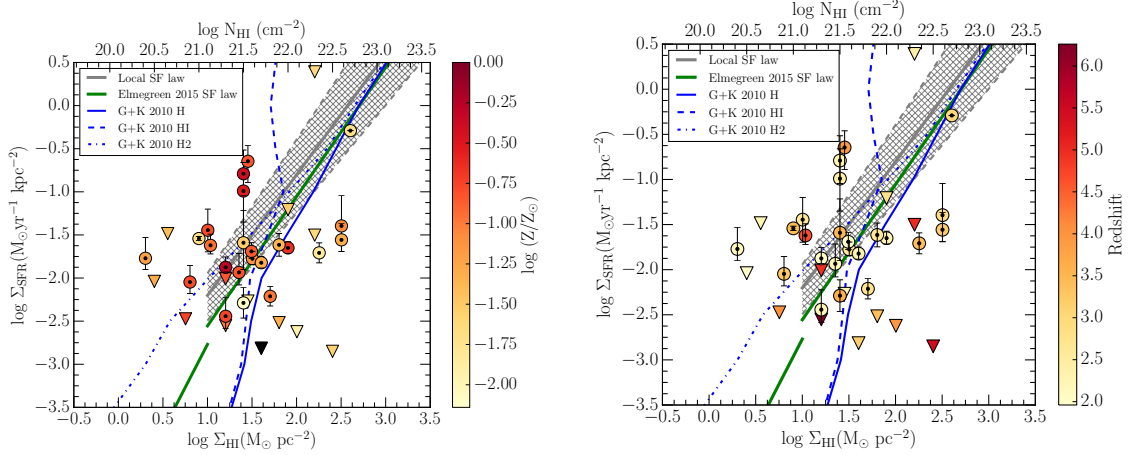


Figure 3.6 Dust corrected SFR surface densities vs. HI gas surface densities of our GRB-DLA counterpart sample. We do not include GRB-DLAs that do not have host dust extinction measurements. Upper limits are shown as triangles as are GRB-DLAs with host extinction upper limits. We overplot the local Kennicutt-Schmidt relation with errors (gray and gray hash; Schmidt 1959; Kennicutt 1998), the local SF law from Elmegreen (2015) (green), and $z \sim 3$ Gnedin & Kravtsov (2010) simulations for total hydrogen, atomic, and molecular gas (blue solid, dashed, and dotted respectively). The *total* neutral gas from Gnedin & Kravtsov (2010) SF laws should be shifted to the right since we are plotting against the *atomic* hydrogen gas content. Additionally the *molecular* hydrogen gas should be shifted to the left since we expect there to be more *atomic* hydrogen gas than *molecular* hydrogen gas. (*Left*) SFR surface densities vs. HI gas surface density color coded with metallicity; black points have no metallicity measurements from absorption lines. (*Right*) SFR surface densities vs. HI gas surface density color coded with redshift.

to indicate a very low Σ_{SFR} for the amount of measured Σ_{HI} . These discrepancies can be due to different factors: GRB afterglow measured metallicities may be lower than the average DLA-host metallicity or the distribution of neutral hydrogen may be poorly approximated (Lanzetta et al., 2002; Hopkins et al., 2005). Finally, while we emphasize here that most of our metallicity estimates are lower limits, the $z \sim 3$ theoretical predictions seem to better predict some of the low metallicity and high metallicity systems.

In Figure 3.7 we overlay our DLA counterparts onto results from Krumholz

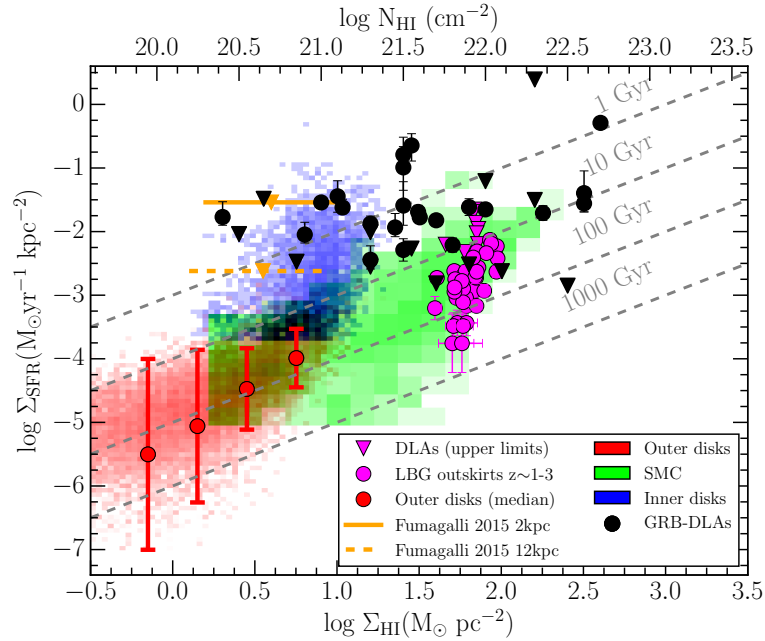


Figure 3.7 Dust-corrected SFR surface densities vs. HI gas surface densities from our GRB-DLAs (black) on top of the compilation of observed SFR surface density vs. gas surface density from Krumholz (2014). The purple points are Lyman break galaxies outskirts at $z \sim 1 - 3$ (uncorrected for dust) from Rafelski et al. (2011, 2016), the purple triangles are DLA limits from Wolfe & Chen (2006), the orange triangles with error bars are composite image limits from dust-uncorrected double-DLAs from Fumagalli et al. (2015). The red pixels are from lines-of-sight through the outer disks of local spiral and dwarf galaxies (Bigiel et al., 2010). The red circles are the median and $1 - \sigma$ scatter. The blue pixels are from the inner parts of local galaxies (Bigiel et al., 2008). The green pixels are from the SMC (Bolatto et al., 2011). Note the SMC, LBG outskirts, and DLA limits are actually plotted for the SFR surface densities vs. the *total* neutral hydrogen gas surface densities, not the *atomic* hydrogen gas surface density. We expect that adjusting these measurements to the HI gas surface densities will move the points to the left. The gray dashed lines mark constant depletion times ($t_{\text{dep}} = M_{\text{gas}}/\text{SFR}$).

(2014) showing the star formation efficiencies in LBG outskirts (Rafelski et al., 2011, 2016), previous DLA upper limits (Wolfe & Chen, 2006), double-DLA composite image limits (Fumagalli et al., 2015), the outer disks of local spiral and dwarf galaxies using 21cm emission to measure HI (Bigiel et al., 2010), the inner disks of the local using 21cm emission to measure HI (Bigiel et al., 2008), and the Small Magellanic Cloud (SMC; Bolatto et al. 2011). Rafelski et al. (2011, 2016) report dust-uncorrected Σ_{SFR} and use a different SFR conversion (see §3.3.1.2) which may partially explain our higher Σ_{SFR} for GRB-DLA hosts (although some discrepancies may still remain). We note that Krumholz (2014) originally plotted the SFR surface density against *total* neutral hydrogen gas surface density not the *atomic* hydrogen gas surface density. We expect that adjusting these measurements to HI gas surface densities will shift the magenta points to the left in the plot.

We also overplot lines of constant depletion times, $t_{\text{dep}} = M_{\text{gas}}/\text{SFR}$. Depletion time represents how long it would take to completely use up the neutral gas (in this case, HI) with a constant SFR. Our sample covers a large range of depletion times, some of which are longer than the age of the Universe as seen by the galaxy at the DLA redshift. This indicates that some of these systems have not reached equilibrium yet and that we are measuring a phase of lower star-formation than in earlier times.

Our GRB-DLA counterparts seem to show no overlap with local outer disk galaxies and seem to have similar depletion times as inner galaxy disks, the SMC, and LBG outskirts (in a few cases). This is consistent with the observational evidence that GRB hosts are compact, SMC type, star-forming galaxies (see also Noterdaeme

et al. 2012b). However, we would caution the reader that GRB-DLAs may sample higher SFRs than QSO-DLAs because GRBs are associated with massive stars that are typically in galaxies with higher specific SFRs. From the DLA counterpart perspective this shows that our sample traces DLAs with shorter depletion times than other DLAs or LBG outskirts (magenta dots; note that these points are dust-uncorrected SFRs), and that its higher metallicity, typically 1%-20% the solar value, can be the cause of this offset (see Krumholz, 2014). For the same reason, most of the magenta points in Figure 3.7 have much longer depletion times at fixed gas surface density than most local spirals.

3.4 Enrichment time

Star formation is only process responsible for metal production. Supernova feedback and stellar winds, on the other hand, contribute to the dispersion of metals towards the outer regions or even outside the galaxy’s potential well. The enrichment time is used to determine if the current star formation rate can solely account for the current measured metallicity and the metal build up of these systems. We assume a very simple scenario where the star formation rate is constant and the metal mass is calculated from the absorption-line metallicity measured from GRB afterglow spectra (“closed box” model).

We calculate the mass in metals:

$$M_{z,\text{obs}} = 10^{[X/H]} Z_{\odot} m_p N_{\text{HI}} \pi r^2 \quad (3.4)$$

where $[X/H]$ is the metallicity measured from absorption listed in Table 3.1, assuming $Z_{\odot} = 0.0181$ (Asplund et al., 2009) and r is the radius that we take to be $1.2''$ across all redshifts. We then assume that the observed mass in metals is solely due to star formation and we can calculate the enrichment time, Δt_z , from

$$M_{z,\text{SFR}} = y_z \dot{\psi} \Delta t_z \quad (3.5)$$

where we assume a metal yield of $y_z = 1/42$ (Madau et al., 1996) and use SFRs ($\dot{\psi}$) from Table 3.1. Note that Eq. 3.4 may overestimate the mass of metals particularly because the metals could be not fully mixed and absorption features typically arise in highly enriched gas. This may lead to inflated enrichment times.

We plot enrichment time against metallicity (Figure 3.8) and overplot the time since $z = 10$ to $z = 2$ and $z = 6$ (where most of our DLAs are found). Some of our DLA counterparts have enrichment times shorter than the age of their host galaxy. This indicates that these galaxies have an underabundance of metals if the metals were formed from a constant SFR. Therefore, it suggests that these systems could have gone through episodic star formation or that feedback expelled metals from the galaxy (stellar or supernova feedback; Davé & Oppenheimer 2007; Rahmati et al. 2016). On the other hand, other DLA hosts have enrichment times longer than the age of the galaxy. This means there is an overabundance of metals if the metals were formed from a constant SFR. This may be evidence of either episodic or exponentially declining star formation, poor mixing between the metals within the DLA and the rest of the host galaxy, or another source of metal enrichment such

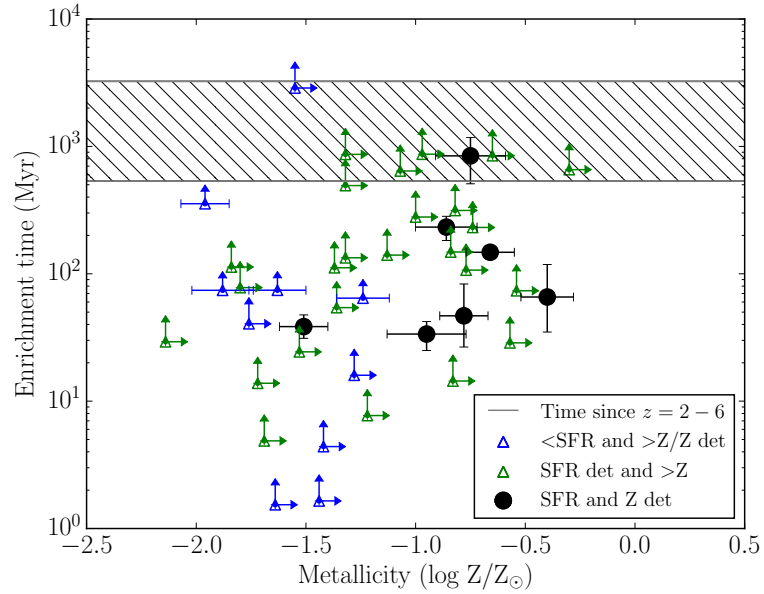


Figure 3.8 Enrichment time assuming that the galaxy has maintained a constant SFR and that the observed absorption-line metallicity is the same as the galaxy-wide metallicity which is purely determined by internal star formation activity. We only have lower limits or detections for metallicity and upper limits and detections for SFRs. Limits are plotted with triangles and the colors represent detected SFRs (green) or upper limit SFRs (blue). Black circles have measured metallicity and measured SFR. The hatched gray area is the time from $z=10$ to our DLA redshifts of 2-6.

as an influx of metal-enriched gas from galaxy mergers. The former have been also invoked by Hunt et al. (2014), which has shown that a significant amount of the total stellar mass ($\geq 10\%$) of some GRB host galaxies can be created in very short ($\sim 50\text{Myr}$) star formation episodes.

3.5 Summary and Conclusions

We present a sample of 45 DLA galaxy counterparts from photometric follow-up of the GRB host locations. We use a sample of spectroscopically confirmed GRB-DLAs identified in Cucchiara et al. (2015) and collect all the publically available GRB host galaxy photometry. We supplement these observations with DCT-LMI photometric follow-up. We present 33 DLA galaxy counterpart detections (though 5 only have A_V upper limits) and 12 upper limits. This quadruples the number of detected DLA counterparts known to date (previously 13, all of which are QSO-DLAs). These GRB-DLAs have a wider range of HI column densities than QSO-DLAs because they are likely located at much smaller impact parameters than QSO-DLA host galaxies.

Our rest-frame UV SFRs are usually higher than QSO-DLA *in situ* identified using the double-DLA technique (Fumagalli et al., 2015) and, while long GRBs come from high SFR areas within their galaxies, we still have upper limits that are consistent with the double-DLA sample as well as other DLA surveys (see Table 2 in Fumagalli et al., 2015). From our sample, the SFR does not seem to be correlated with either redshift or column density, and we cannot determine if SFR correlates

with DLA metallicity due to the effect of line saturation and blending in GRB afterglow spectra.

We investigate how our sample relates to the Kennicutt-Schmidt relation by looking at the relationship between star formation surface density and HI column density. Our GRB-DLA galaxy counterpart sample spans both high and lower efficiency of star formation compared to a variety of star formation laws (local Kennicutt-Schmidt relation; Schmidt 1959; Kennicutt 1998, Elmegreen 2015 SF laws, and Gnedin & Kravtsov 2010 simulations at $z \sim 3$). We also compare our sample to objects in the local Universe and find that our sample is not consistent with the star formation efficiencies of local spiral and dwarf galaxies. Instead, we find similar efficiencies to local Universe inner disks, SMC, and LBG outskirts, complementing what has been currently observed from QSO-DLA counterparts. We caution the reader that our SFRs represent a measurement performed over the integrated host galaxies light while the HI column densities are measured locally along the line-of-sight of the GRB afterglows and may be subject to observational biases (metal rich, star-forming environments) compared to the average HI column density of the DLAs.

We also examine the depletion times of our systems. Depletion time is a measure of how long it would take to completely deplete the DLA gas, HI gas in our case, assuming that the current SFR remains constant. Our sample spans a large range of depletion times (1-100 Gyr). Some of the our sample's depletion times are longer than the current age of the Universe as seen by the galaxy which indicates that these systems have not reached equilibrium yet.

Finally, we investigate the enrichment time of our DLA host counterparts. Enrichment time is the measure of how long it would take to form all the current metals assuming they were solely formed from star formation at the current constant SFR. Some DLA counterparts have enrichment times that are much shorter than the age of the galaxy which indicates that the galaxy underwent episodic star formation. Some DLA counterparts have enrichment times that are longer than the age of the galaxy which indicate an overabundance of metals assuming a constant SFR. This suggests that these galaxies may have had episodic star formation histories, there may be other sources of metal enrichment such as galaxy mergers, or that there is poor metal mixing between the metals in the DLA and the rest of the host galaxy.

The higher detection rate of GRB-DLA host galaxies and their properties (e.g. SFR, metallicity) may indicate that QSO-DLAs are an entirely different population than GRB-DLAs. While investigation of this issue is beyond the scope of this study, we note that such a difference may be due to an intrinsic bias in the GRB-DLA sample such that they represent actively star-forming regions with special conditions correlated with the likelihood of GRB appearance (e.g. trace different physical regions of galaxy). Additionally, metallicity may affect the GRB environment differently than QSO-DLAs.

GRB-DLAs are unique objects that have good localization and can later be followed up with photometry and spectroscopy. These are key advantages with respect to the identification of DLAs along QSOs. However, it is unclear if these objects are from the same DLA population. Our sample, complementary to the QSO-DLAs, is the largest collection of DLA galaxy counterparts available to date

bringing the total number of detected DLA counterparts from 13 to 58. Future deep, multi-band, follow-up observations of the remaining GRB-DLAs, in particular with *HST* and large aperture telescopes, will increase the sample size for comparisons with cosmological simulations. Furthermore, we showed the importance of accurate identification (sub-arcsecond or better) of GRB afterglows in precisely pinpointing the DLA location within their host, especially in lieu of more powerful, parsec scale, simulations. Finally, it will be important to investigate the morphology of DLA hosts, in particular using GRB host galaxies, which seem to show signs of pair interaction (Cooke in prep, private communication) and may open new insights on the nature of DLAs and the *in situ* star-formation.

Table 3.1. GRB-DLA Host Galaxy Sample

GRB-DLA	Redshift ^a	log N _{HI} (cm ⁻²)	log Z/Z _⊙	A _V	SFR ^b (M _⊙ yr ⁻¹)	log M _* (M _⊙)	log M _{dust} (M _⊙)	Ref.
000926	2.03621	21.30 ± 0.25	> -0.30	0.038	3.03 ^{+0.97} _{-0.36}	9.90 ^{+0.16} _{-0.22}	6.00 ^{+0.55} _{-0.00}	(1)
011211	2.1427	20.40 ± 0.20	> -1.22	0.138	3.86 ^{+2.85} _{-1.00}	8.94 ^{+0.18} _{-0.28}	6.19 ^{+0.70} _{-0.19}	(2)
020124	3.198	21.70 ± 0.20	...	0.280 ± 0.330 ^c	< 0.35	(3),(4)
030226	1.98	20.50 ± 0.30	> -1.28	0.060 ± 0.060 ^c	< 2.08	(4),(5)
030323	3.3714	21.90 ± 0.07	> -1.32	< 0.020 ^c	< 0.69	(3),(4)
030429	2.658	21.60 ± 0.20	> -1.13	0.400 ± 0.100 ^c	3.82 ^{+0.79} _{-0.56} ^d	(3),(4)
050319	3.24	20.90 ± 0.20	> -0.77	0.050 ± 0.060 ^c	2.05 ^{+1.14} _{-0.54} ^d	(6),(7)
050401	2.899	22.60 ± 0.30	> -1.07	0.738	9.16 ^{+11.35} _{-4.52}	9.56 ^{+0.23} _{-0.21}	7.00 ^{+0.64} _{-0.63}	(3),(6),(8),(9)
050730	3.96723	22.10 ± 0.10	-1.96 ± 0.11	0.120 ± 0.020 ^c	< 0.54	(9),(10)
050820A	2.6145	21.10 ± 0.10	-0.78 ± 0.11	0.813	8.17 ^{+6.19} _{-3.57}	9.16 ^{+0.17} _{-0.17}	6.94 ^{+0.60} _{-0.59}	(3),(6),(8),(9)
050904	6.26	21.30 ± 0.20	> -1.00	< 0.050 ^c	< 0.64 ^d	(11),(12)
050922C	2.1996	21.55 ± 0.10	-1.88 ± 0.14	0.090 ± 0.030 ^c	< 1.23	(3),(13)
060115	3.533	21.50 ± 0.10	> -1.53	0.763	5.85 ^{+8.02} _{-2.98}	9.33 ^{+0.20} _{-0.28}	6.81 ^{+0.64} _{-0.65}	(6),(8),(9)
060206	4.048	20.85 ± 0.10	> -0.74	< 0.170 ^c	< 0.77	(9),(13)
060210	3.913	21.55 ± 0.15	> -0.83	0.363	51.52 ^{+27.36} _{-22.21}	9.99 ^{+0.15} _{-0.12}	7.52 ^{+0.61} _{-0.65}	(6),(14)
060223A	4.41	21.60 ± 0.10	> -1.80	...	1.03 ^{+0.24} _{-0.16} ^d	(9)

Table 3.1 (cont'd)

GRB-DLA	Redshift ^a	log N _{HII} (cm ⁻²)	log Z/Z _⊙	A _V	SFR ^b (M _⊙ yr ⁻¹)	log M _* (M _⊙)	log M _{dust} (M _⊙)	Ref.
060510B	4.94	21.30 ± 0.10	> -0.84	< 0.500 ^c	< 2.23 ^d	(6),(14)
060522	5.11	21.00 ± 0.30	< 2.96	(15)
060707	3.425	21.00 ± 0.20	> -1.69	0.080 ± 0.020 ^c	6.54 ^{+0.37} _{-0.35}	(8),(10)
060714	2.711	21.80 ± 0.10	> -0.97	0.210 ± 0.020 ^c	1.40 ^{+0.41} _{-0.32}	(8),(10)
060926	3.206	22.60 ± 0.15	> -1.32	0.320 ± 0.020 ^c	6.31 ^{+3.52} _{-1.67} ^d	(10),(16)
060927	5.464	22.50 ± 0.15	> -1.55	< 0.170 ^c	< 0.32	(9),(13)
061110B	3.433	22.35 ± 0.10	> -1.84	0.230 ± 0.030 ^c	4.46 ^{+1.37} _{-1.05} ^d	(8),(10)
070110	2.351	21.70 ± 0.10	> -1.32	0.100 ± 0.100 ^c	3.43 ^{+0.63} _{-0.46} ^d	(8),(10)
070506	2.308	22.00 ± 0.30	> -0.65	0.440 ± 0.050 ^c	5.09 ^{+0.98} _{-0.71} ^d	(8),(10)
070721B	3.628	21.50 ± 0.20	> -2.14	0.200 ± 0.020 ^c	1.17 ^{+0.59} _{-0.39}	(8),(10)
070802	2.455	21.50 ± 0.20	> -0.54	0.838	23.28 ^{+26.49} _{-13.12}	9.71 ^{+0.11} _{-0.11}	7.33 ^{+0.65} _{-0.67}	(8),(9),(17),(18)
080210	2.641	21.90 ± 0.10	> -1.37	0.330 ± 0.030 ^c	5.53 ^{+1.96} _{-1.45}	(5),(10)
080607	3.037	22.70 ± 0.15	> -1.72	2.938	116.68 ^{+0.00} _{-0.00}	10.13 ^{+0.00} _{-0.00}	8.36 ^{+0.49} _{-0.52}	(6),(9),(17)
080804	2.20542	21.30 ± 0.10	-0.75 ± 0.16	0.170 ± 0.110 ^c	0.82 ^{+0.54} _{-0.23} ^d	(6),(13)
081008	1.96	21.59 ± 0.10	-0.86 ± 0.14	0.290 ± 0.070 ^c	4.64 ^{+1.27} _{-0.82} ^d	(7),(9)
090205	4.64	20.73 ± 0.05	> -0.57	...	6.14 ^{+0.59} _{-0.54}	(19)

Table 3.1 (cont'd)

GRB-DLA	Redshift ^a	$\log N_{\text{HI}}$ (cm^{-2})	$\log Z/Z_{\odot}$	A_V	SFR ^b ($M_{\odot} \text{ yr}^{-1}$)	$\log M_{*}$ (M_{\odot})	$\log M_{\text{dust}}$ (M_{\odot})	Ref.
090516	4.109	21.73 ± 0.10	> -1.36	...	$5.87^{+3.43}_{-2.17}$	(20)
090812	2.425	22.30 ± 0.10	> -1.64	0.230 ± 0.080^c	< 561.26	(5),(13)
100219A	4.667	21.13 ± 0.12	-0.95 ± 0.18	0.130 ± 0.050^c	$5.45^{+1.89}_{-1.12}^d$	(21)
110205A	2.214	21.45 ± 0.20	> -0.82	0.350 ± 0.060^c	$2.65^{+1.74}_{-0.75}^d$	(6),(13)
111008A	4.98968	22.30 ± 0.06	-1.63 ± 0.13	0.110 ± 0.040^c	< 7.16	(22)
120327A	2.813	22.01 ± 0.09	-1.51 ± 0.11	$< 0.030^c$	< 14.16	(23)
120716A	2.487	21.55 ± 0.15	> -1.76	...	< 2.84	(5)
120909A	3.9293	21.20 ± 0.10	-0.66 ± 0.11	...	$3.31^{+0.39}_{-0.35}$	(20)
121024A	2.2977	21.50 ± 0.10	-0.40 ± 0.12	0.563	$36.90^{+32.60}_{-16.39}$	$10.15^{+0.16}_{-0.17}$	$7.54^{+0.60}_{-0.60}$	(24)
121201A	3.385	21.70 ± 0.20	$6.45^{+1.38}_{-1.13}$	(20)
130408A	3.757	21.70 ± 0.10	-1.24 ± 0.12	...	< 6.54	(20)
130505A	2.2687	20.65 ± 0.10	> -1.42	$< 0.128^c$	< 7.47	(5),(25)
140423A	3.258	20.45 ± 0.20	> -1.44	...	< 8.95	(5)

Note. — ^aSignificant digits of redshift reflect accuracy of measurement. ^bDust-corrected (except those without A_V measurements). ^cHost extinction from GRB afterglow measurements. ^dCalculates SFR from MAGPHYS SED scaling of photometric detection. (1) Castro et al. 2003, (2) Fynbo et al. 2003, (3) Chen et al. 2009, (4) Kann et al. 2006, (5) This work, (6) Perley et al. 2016b, (7) Schady et al. 2012, (8) Hjorth et al. 2012, (9) Blanchard et al. 2016, (10) Zafar et al. 2011, (11) McGuire et al. 2015, (12) Zafar et al. 2010, (13) Covino et al. 2013, (14) Perley et al. 2009, (15) Basa et al. 2012, (16) Laskar et al. 2011, (17) Perley et al. 2013, (18) Krühler et al. 2011, (19) D’Avanzo et al. 2010, (20) Greiner et al. 2015b, (21) Thöne et al. 2013, (22) Sparre et al. 2014, (23) D’Elia et al. 2014, (24) Friis et al. 2015, (25) Cannizzo et al. 2013

Table 3.2. GRB sub-DLA Host Galaxy Sample

GRB sub-DLA	Redshift ^a	$\log N_{\text{HI}}$ (cm^{-2})	$\log Z/Z_{\odot}$	A_V	SFR ^b ($M_{\odot} \text{ yr}^{-1}$)	$\log M_{\star}$ (M_{\odot})	$\log M_{\text{dust}}$ (M_{\odot})	Ref.
021004	2.3289	19.00 ± 0.20	...	0.038	$7.19^{+0.17}_{-1.21}$	$9.29^{+0.06}_{-0.32}$	$9.29^{+0.06}_{-0.32}$	(1),(2)
050908	3.344	19.40 ± 0.20	...	$< 0.550^c$	$3.21^{+1.65}_{-1.09}$	(3),(4)
060124	2.3	18.50 ± 0.50	...	0.170 ± 0.030^c	$0.46^{+0.10}_{-0.07}{}^d$	(5),(6)
060526	3.221	19.90 ± 0.15	...	0.700 ± 0.180^c	$1.63^{+0.91}_{-0.43}{}^d$	(6),(7)
060605	3.773	18.90 ± 0.40	$0.40^{+0.06}_{-0.05}$	(5)
060607A	3.075	16.95 ± 0.03	...	0.080 ± 0.040^c	< 0.29	(3),(8)
080310	2.427	18.70 ± 0.10	...	0.100 ± 0.020^c	$1.82^{+1.14}_{-0.51}{}^d$	(4),(7)
080810	3.35	17.50 ± 0.15	$27.33^{+15.99}_{-10.09}$	(9)
080913	6.69	< 19.84	...	0.120 ± 0.030^c	< 1.51	(10),(11)
090323	3.5778	> 19.90	$9.72^{+1.75}_{-1.49}$	(12)
090426	2.609	19.10 ± 0.15	...	0.088	$3.03^{+0.00}_{-0.00}$	$8.48^{+0.00}_{-0.00}$	$8.48^{+0.00}_{-0.00}$	(13)
130606A	5.9134	19.93 ± 0.20	$1.63^{+0.37}_{-0.25}{}^d$	(14)

Note. — ^aSignificant digits of redshift reflect accuracy of measurement. ^bDust-corrected (except those without A_V measurements). ^cHost extinction from GRB afterglow measurements. ^dCalculates SFR from MAGPHYS SED scaling of photometric detection. (1) Fynbo et al. 2005, (2) de Ugarte Postigo et al. 2005, (3) Hjorth et al. 2012, (4) Perley et al. 2009, (5) Blanchard et al. 2016, (6) Kann et al. 2010, (7) Perley et al. 2016b, (8) Schady et al. 2012, (9) Greiner et al. 2015b, (10) Basa et al. 2012, (11) Zafar et al. 2011, (12) McBreen et al. 2010, (13) Thöne et al. 2011, (14) McGuire et al. 2015

Chapter 4: RIMAS: Hardware

The Rapid infrared IMAger-Spectrometer (RIMAS) has been designed to quickly follow-up dusty or high-redshift ($z \gtrsim 7$) GRB afterglows in the near-infrared with photometry and spectroscopy. This chapter describes the instrument hardware, in particular, an overview of the instrument and the RIMAS detectors and detector driver systems.

4.1 RIMAS Overview

RIMAS is a near-infrared (0.97-2.39 μm) instrument that can operate in three observing modes: photometric imaging, low-resolution ($R \sim 30$) spectroscopy, and high-resolution ($R \sim 4000$) spectroscopy. RIMAS is a fully cryogenic instrument that operates in a vacuum nominally at $\sim 60\text{K}$.

4.1.1 Discovery Channel Telescope

RIMAS will be permanently installed on the instrument cube at the f/6.1 position of the 4.3-meter Discovery Channel Telescope (DCT; Figure 4.1) near Happy Jack, Arizona. RIMAS will share the telescope with four other instruments mounted on the DCT instrument cube. The DCT can rapidly switch between instruments by

placing either a folding mirror or dichroic beamsplitter in the center of the instrument cube. When RIMAS is in use, a dichroic beamsplitter inside the instrument cube will allow simultaneous use of RIMAS and an optical imager, the Large Monolithic Imager (LMI), that has a $12.5' \times 12.5'$ field-of-view. The DCT was declared fully operational with its first light instrument, LMI, at the beginning of 2015.



Figure 4.1 The 4.3-meter Discovery Channel Telescope in the stowed position. The instruments sit behind the primary mirror at the base of the telescope in an instrument cube that moves with the telescope. The image was retrieved from <http://www.bu.edu>.

4.1.2 RIMAS design

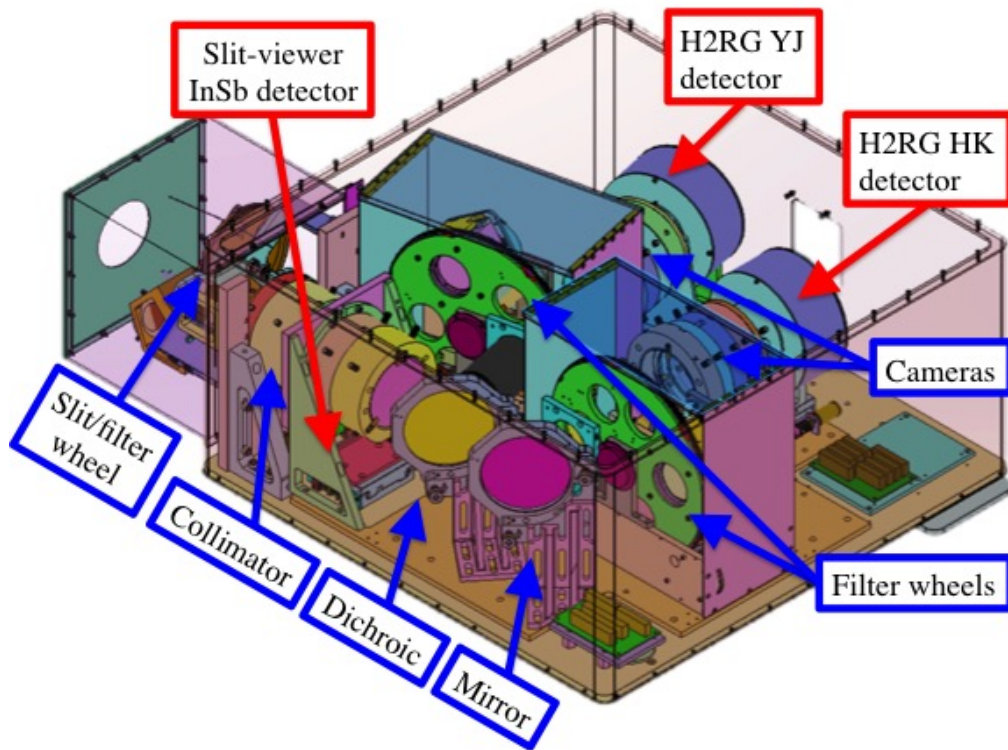


Figure 4.2 CAD model of RIMAS showing the main dewar with the front dewar assembly attached in the upper left hand corner. The main components of the instrument are labeled, components labeled in red are a significant part of this thesis work and will be covered in more detail in §4.2.

RIMAS consists of a main dewar that includes all the main optics and detectors and a front dewar assembly that includes a slit wheel (with an open position), a filter wheel for custom filters that can be changed throughout the lifetime of the instrument, and slit-viewer optics that allow guiding on the slit in spectroscopic modes by using mirrored surfaces around the slits. Both the main dewar and front

dewar assembly are shown in a computer-aided design (CAD) model in Figure 4.2 and the components of the front dewar assembly are shown in a more detail in Figure 4.3. Figure 4.4 shows the instrument during the integration phase.

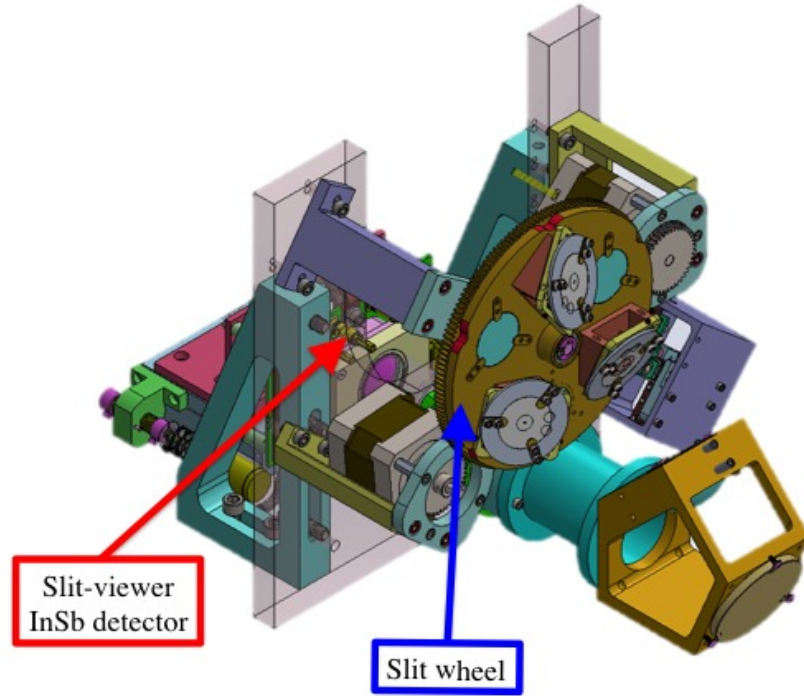


Figure 4.3 CAD model of the interior of the front dewar assembly where the translucent gray part demarks the border between the main dewar and the front dewar assembly. Light is reflected off the mirrored surface of the slit into the slit-viewer optics that sit below the slit wheel and is directed into the slit-viewer InSb detector.

In the main dewar, RIMAS has two optical arms (YJ and HK) split by a dichroic beamsplitter which allows for simultaneous imaging or spectroscopy in two separate bandpasses. For a detailed description of the RIMAS optical design see Capone (2016). In addition to the slit wheel and filter wheel in the front dewar assembly, each optical arm has a filter wheel with two filters, transmission spec-

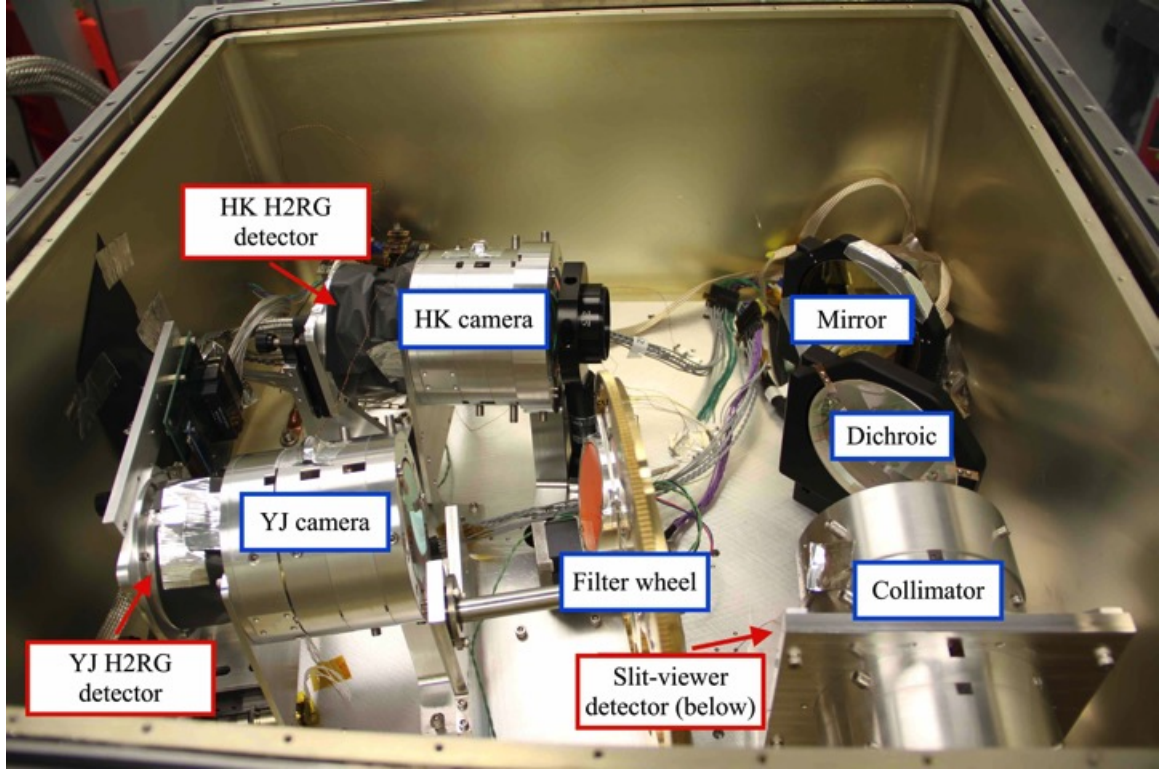


Figure 4.4 The RIMAS main dewar during the integration phase. Components labeled in red are a significant part of this thesis work and will be covered in more detail in §4.2.

troscopic elements, and an open and closed position. RIMAS can switch between observing modes in less than a minute using these filter and slit wheels.

RIMAS has three detectors that sit on focusing stages: each optical arm camera has a Teledyne HgCdTe Astronomy Wide Area Infrared Imager with 2K x 2K, Reference Pixels and Guide Mode (H2RG) science detector and a slit-viewer *Spitzer* Legacy Indium-Antimonide (InSb) detector sits below the collimator. The detectors and detector electronics are described in detail in §4.2.

RIMAS has a $3' \times 3'$ field-of-view and the slit-viewer has $80'' \times 80''$ field-of-view. Both the main optics and slit-viewer optics have a plate scale of $0.35''/\text{pixel}$. The instrument is held in vacuum $< 10^{-8}$ Torr using a turbopump and is cooled with

a two stage cryo-cooler that cools the optics, mechanical components, and science detectors to $\sim 65\text{K}$ and the InSb detector is cooled to $\sim 15\text{K}$.

4.2 RIMAS Detectors

The majority of this thesis work has focused on operating, characterizing, and analyzing the RIMAS detectors. RIMAS uses three hybrid detectors: two science Teledyne HgCdTe Astronomy Wide Area Infrared Imager with $2\text{K} \times 2\text{K}$, Reference Pixels and Guide Mode (H2RG) detectors (Figure 4.5) and one *Spitzer* Legacy Indium-Antimonide (InSb) slit-viewer detector (Figure 4.6). We have characterized multiple detectors for this thesis but here we only present the detector characterization of the final RIMAS detectors.

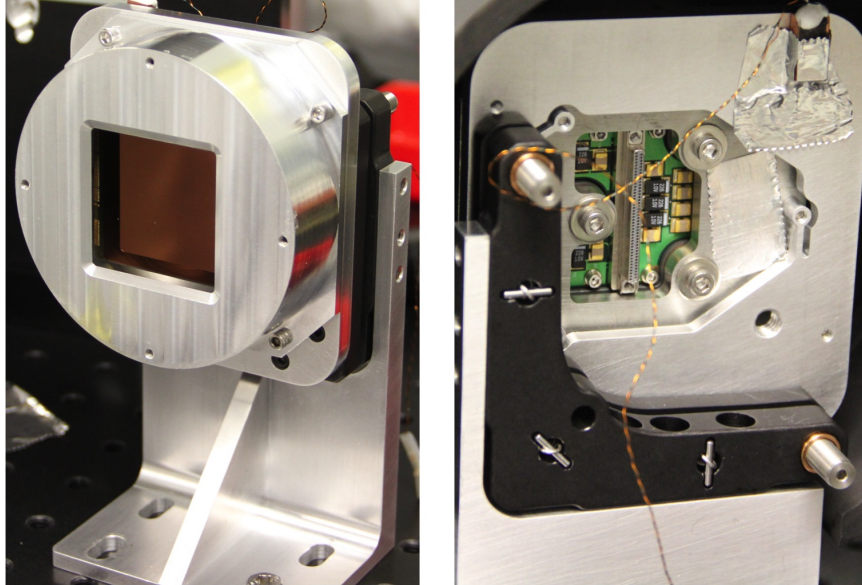


Figure 4.5 RIMAS science $2\text{k} \times 2\text{k}$ pixel H2RG detector. Both detectors have the same readout circuitry. (*left*) Front of the mounted detector array. (*right*) Back of the mounted detector array. A harness connects to the back of the array to deliver clocks and biases to the detector and return the detector signal to the detector acquisition system.



Figure 4.6 RIMAS slit-viewer 256 x 256 pixel InSb detector. Three harnesses connect to the circuit board to deliver clocks and biases to the detector and return the detector signal to the detector acquisition system.

4.2.1 Detector Introduction

4.2.1.1 Semiconductors

Semiconductors either have free electrons or free “holes”. Unlike insulators or conductors, semiconductors have a small but non-negligible separation between the valence band (where electrons are tightly bonded) and conduction band (where electrons are free flowing) which is called a band gap with energy E_g . If a photon with $E > E_g$ strikes the semiconductor it can free an electron, effectively turning a photon into an electron. The band gap energy can be altered by adding impurities to the semiconductor material; this process is called doping.

There are two types of semiconductors, N-type and P-type, which are created with different types of impurities. A N-type semiconductor has free electrons when bound in a lattice, whereas a P-type semiconductor has holes when bound in a lattice

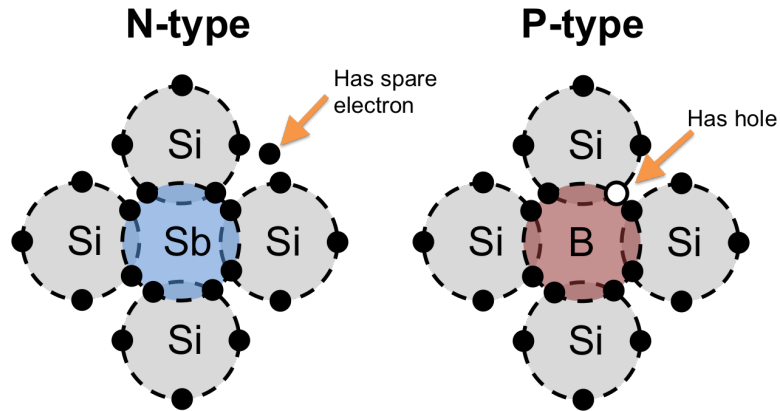


Figure 4.7 Examples of N-type and P-Type semiconductors. A N-type semiconductor has extra electrons that are not tightly bound, whereas a P-type semiconductor has extra holes that will accept free electrons.

(Figure 4.7). When a P-type and N-type semiconductor are joined, the region where they touch is called the PN junction. At this junction holes and electrons combine to create a depletion zone which acts as an insulator and allows current to flow in only one direction when an electric potential difference is applied, effectively acting as a diode (Figure 4.8). When a photon with energy above the band gap energy strikes the PN semiconductor, the potential sweeps the electron or hole through the junction and current can flow through the system; effectively creating a photodiode or detector.

4.2.1.2 Semiconductor Material

Optical detectors are typically made of silicon because silicon has band gap energies that are well matched to optical wavelengths, silicon is a readily available material, and the technology to process silicon is well developed and therefore cost effective. Arsenic doped silicon (Si:As) can also be used for the mid-infrared but

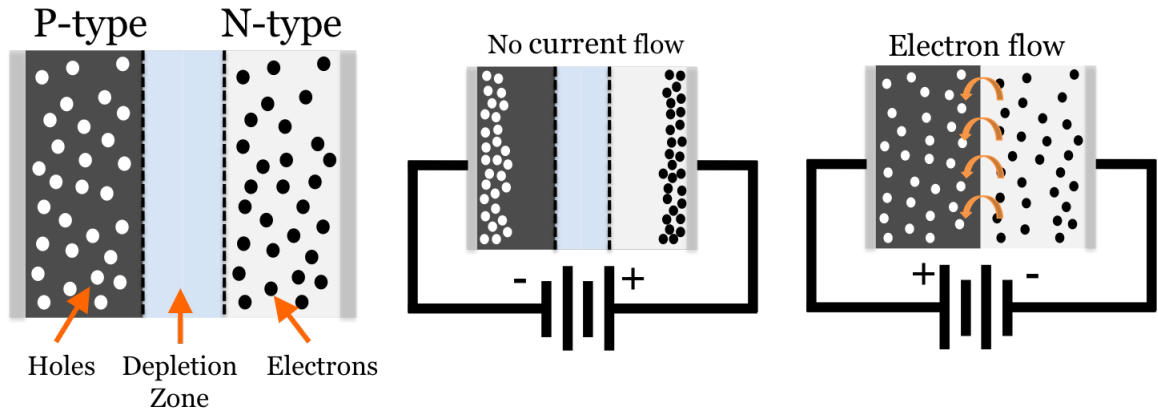


Figure 4.8 (*left*) When a P-type and a N-type semiconductor are joined they create a PN junction called the depletion zone where holes and electrons have combined to create a small insulation barrier. (*middle*) No current can flow when the system is configuration in this way. (*right*) Electrons or holes can flow when the electrical potential direction is switched. The combined material still maintains its semiconductor properties but now also acts like a diode. Figure adapted from <http://www.imagesco.com/articles/photovoltaic/photovoltaic-pg3.html>

the most common semiconductor materials in the near-infrared are mercury cadmium telluride (HgCdTe), indium antimonide (InSb), and indium gallium arsenic (InGaAs). RIMAS detectors are made of HgCdTe and InSb.

4.2.1.3 Detector Types

The most common type of near-infrared detector is a hybrid array. Hybrid arrays are made using photodiode material tuned for the near-infrared band gap, but the readout circuitry is made of silicon which has much more developed manufacturing technology (Figure 4.9). The photodiode material is joined to the silicon readout circuitry by bump bonding the two materials with electrical conductors (usually indium) and filling the gaps with epoxy to ensure the array is rigid. The readout circuitry uses multiplexed metal-oxide semiconductor field-effect transistors

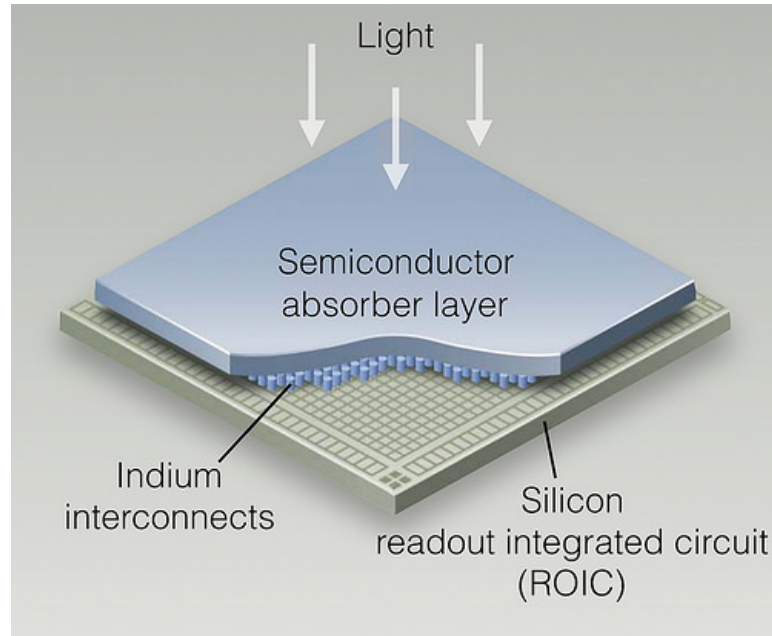


Figure 4.9 An example of the components in a hybrid array. The incoming light interacts with a semiconductor absorber layer (in RIMAS's case this is either HgCdTe or InSb depending on the detector) and the array is read with silicon readout circuitry. The two layers are connected with electrical conductors (usually indium) and the gaps are filled with epoxy to ensure that the array remains rigid. Image from <http://jwst.nasa.gov/infrared.html>.

(MOSFETs).

MOSFETs have a metal electrode and semiconductor material that sandwich an oxide/insulator (Figure 4.10). The metal electrode is commonly referred to as a gate and when voltage is applied to the gate it creates a pile-up of electrons at the barrier between the semiconductor and insulator. The amount of electrons that can roll into that potential well is called the well depth of the detector. The semiconductor part of the MOSFET has either two N-type (or P-type) semiconductor terminals separated and surrounded by P-type (or N-type) semiconductors (Figure 4.11). One of these terminals is called the source and the other is called a drain. The drain is typically attached to ground and the source is attached to a positive

voltage. Current is unable to flow when there is no voltage applied to the gate. However, when voltage is applied to the gate, charge on the gate creates an inverted channel between the source and drain and allows current to flow. A small voltage applied on the gate can create a large amount of current through the transistor and the amount of voltage on the gate is proportional to the amount of current. Since hybrid arrays have MOSFETs for each pixel that means each pixel can be read out separately.

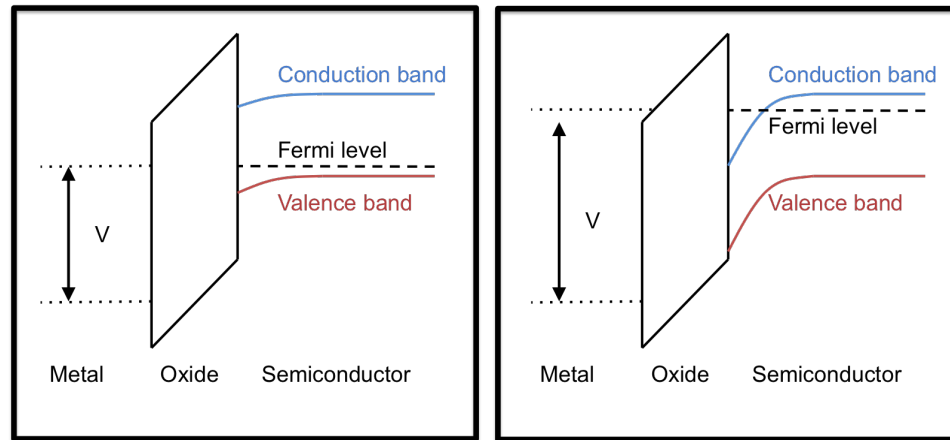


Figure 4.10 Energy diagram of a MOSFET. The semiconductor has a conduction band and valence band and the Fermi level is the typical energy of an electron. (*left*) MOSFET with a small voltage applied to the metal electrode. The voltage bends the conduction and valence bands a little towards lower energies, but the Fermi level is still below the conduction band so most electrons stay bound. (*right*) MOSFET with a large voltage applied to the metal electrode. The voltage bends the conduction and valence bands a lot towards lower energies and the Fermi level is above part of the conduction band allowing free electrons to fill the energy well.

Hybrid arrays typically have more noise than charge coupled devices (CCDs) because each pixel must have additional circuitry for multiplexing, however, hybrid arrays are able to run in non-destructive read mode. This means the charge accumulated on each pixel's gate will not be destroyed when the pixel is read and the pixel can be read multiple times throughout an acquisition unlike a CCD. Multiplexed

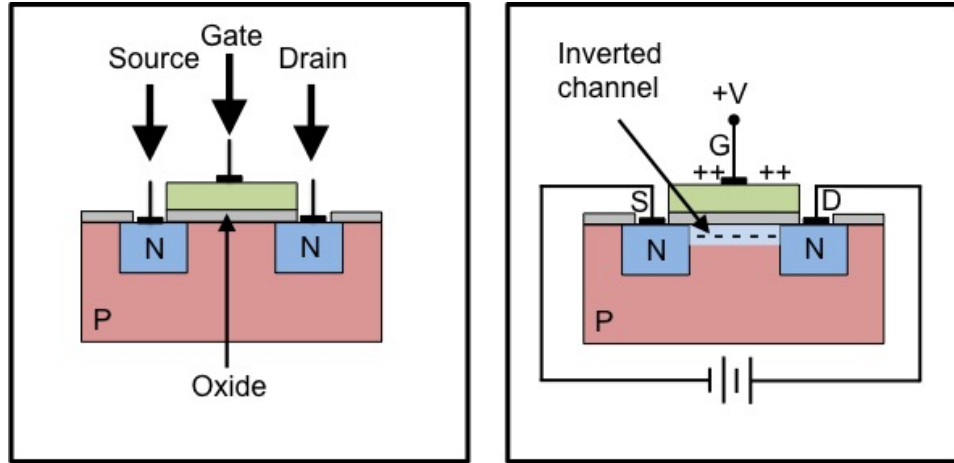


Figure 4.11 An example of a N-channel MOSFET. (*left*) MOSFET with unconnected electrodes. Charge cannot flow between the P-type and N-type semiconductors when there is no electric potential. (*right*) MOSFET with the source and drain connected to a battery or voltage source and voltage applied to the gate. In the N-channel MOSFET the positive voltage pushes electrons into the P-type semiconductor which allows current to flow between the source and drain. Figure adapted from <http://www.allaboutcircuits.com/textbook/semiconductors/chpt-2/insulated-gate-field-effect-transistors-mosfet/>.

arrays can also run in windowing mode which means a user can choose to read a small portion of the detector to greatly reduce the readout time.

4.2.2 Operating hybrid detectors

While each pixel in a hybrid detector can be read individually, it is impractical to read every pixel simultaneously, particularly for larger arrays. For instance RIMAS's H2RGs have over four million pixels. To read four million pixels simultaneously the system would require four million wires running to four million analog-to-digital converters (ADCs). That would result in a very complex and difficult system to debug. Instead, hybrid detectors often have multiple readout channels ranging from $\sim 1-64$ to decrease the total readout time without drastically increas-

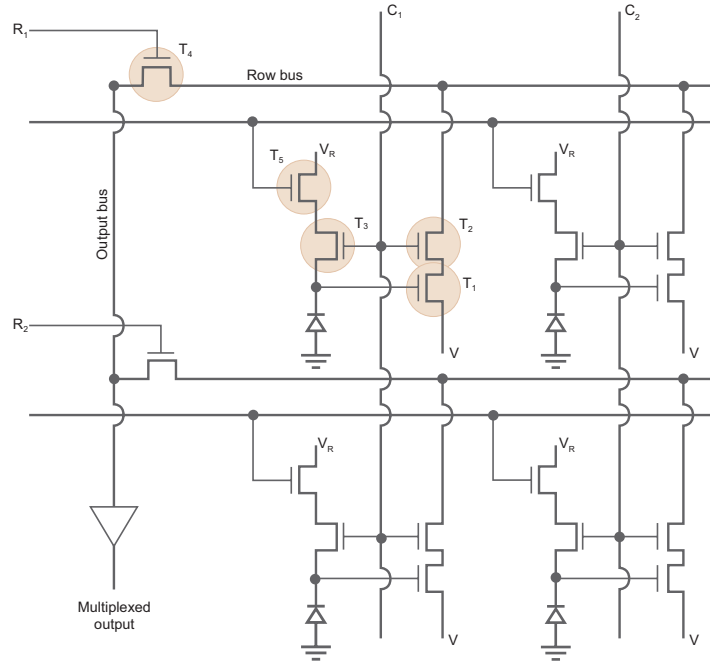


Figure 4.12 An example ROIC diagram from Rieke (2007). The gate of transistor T_1 collects charge from the photodiode (a single pixel). In order to measure the signal on the pixel, power has to be applied to both R_1 and C_1 (row and column drivers respectively) simultaneously which will subsequently be read out by external circuitry. If the pixel is not being read out it will accumulate charge. Power is cycled to other row and column drivers to read other pixels. To reset the pixel, the reset line attached to T_5 is powered (while R_1 and C_1 are powered) and sets the gate of T_1 to voltage V_R effectively clearing the charge accumulated from the pixel.

ing the complexity of the system. In order to cycle through the detector and read four million pixels with tens of readout channels, each pixel has multiple transistors attached to it that allow us to cycle through the detector in a controlled manner and reset each pixel (Figure 4.12). This circuitry is called the Readout Integrated Circuit (ROIC) and is controlled with bias and timing boards. The bias boards set the voltage levels on the transistors and can affect the sensitivity of the detector. The optimal voltages are typically determined empirically.

The timing board sends a repeating set of digital signals called clocks that the detector ROIC interprets into reading particular pixels. There are often 10 or

more clocking signals sent to the detector ROIC simultaneously. The most common clocking signals are (1) row clocks - a high value means to move to the next row, commonly the rows are the “slow” clocks, (2) column clocks - a high value means to move to the next column, commonly the columns are the “fast” clocks stepping through each column within a row, (3) frame clock - a high value means the frame is being read, (4) reset clock - a low value means to reset pixels, often while the reset clock is active the column and row clocks go high very quickly to reset the detector rapidly, and (5) read clock - a high value means to read the current pixel value. The rail voltages of digital signals are called transistor-transistor logic (TTL) levels and these must be within a certain range set by the ROIC.

When a detector is read it converts accumulated charge into voltage and the signal is amplified and sent to an external readout circuitry with analog-to-digital converters (ADC). Once the detector signal is digitized it is sent to a computer. The digital signals combined with knowledge of the read, row, and column clock patterns allows us to reconstruct the detector image from our multiple channel readout. The ADC biases must be adjusted so the detector signal is within range of the ADC.

We refer to the combination of bias board, timing board, ADC boards, and the software behind it as the detector driver system. RIMAS uses two types of detector driver systems. Both H2RGs are controlled using Leach/Astrocam Research Camera, Inc. (Leach/ARC) hardware and the InSb detector is controlled using custom hardware controlled by a Labview compact Real-time Input Output (cRIO).

4.2.2.1 Multiplexer sampling modes

Since multiplexed hybrid arrays have non-destructive reads there are several different ways to sample the data: correlated double sampling (CDS), up-the-ramp (UTR) sampling, Fowler sampling (also known as multiple frame CDS), and multiple frame UTR sampling. In each mode the detector is reset at the beginning of a frame by connecting transistors that allow the charge to drain. After the detector is reset, the detector is immediately sampled before photoelectrons have accumulated. Figure 4.13 shows an example of each type of sampling mode.

CDS consists of reading an initial frame (pedestal) immediately after a reset, followed by an exposure time, then reading one final frame (signal). The pedestal frame is subtracted from the signal frame to reduce fixed pattern noise (noise from a certain location from the underlying structure of the array) and reset noise. Fowler sampling is an extension of CDS where the pedestal and signal consist of multiple frames instead of just a single frame each both the pedestal and signal. Fowler sampling has the same number of frames in the pedestal and signal sets. The median of each pixel in the set of pedestal frames is subtracted from the median of each pixel in the set of signal frames. This reduces the read noise by a factor of \sqrt{N} where N is the number frames in the pedestal or signal sets (Fowler & Gatley, 1990). Traditionally N is chosen to be a power of two.

UTR sampling consists of reading one frame followed by an exposure time, then repeating the process multiple times without removing the charge accumulated on the pixels. Each read is separated by an exposure time of the same length and the

acquisition ends on a read frame. This mode was introduced as a way for space missions to identify when cosmic ray events occurred. A best-fit straight line can be applied to the data to get the mean flux rate. This readout mode also reduces read, fixed pattern, and reset noise. Multiple frame UTR sampling consists of UTR sampling with multiple frames taken for each read and is a combination of Fowler and UTR sampling.

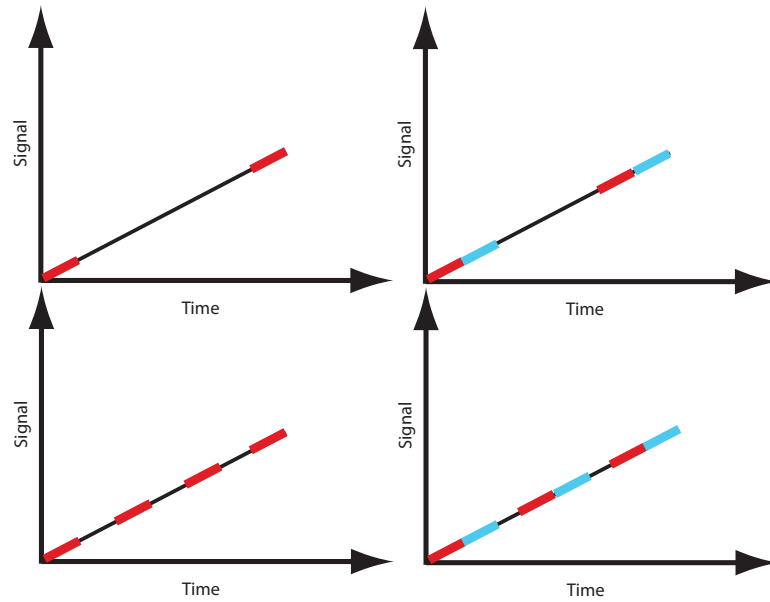


Figure 4.13 Examples of different readout modes used with hybrid detectors, see text for description. In all four cases the detector is only reset once and is read in non-destructive read mode. (it top left) Correlated double sampling. (it top right) Fowler sampling or multiple frame correlated double sampling. Example with $N=2$. (it bottom left) Up the ramp sampling. (*bottom right*) Multiple frame up the ramp sampling with $N=2$.

4.2.3 RIMAS detector drivers

4.2.3.1 Leach/ARC detector driver

We use two sets of identical ARC controllers (Leach & Low, 2000) to operate RIMAS's two H2RG science detectors. Each set includes a PCI card - ARC-64, timing board - ARC-22, clock driver - ARC-32, and four video boards that output biases to the detector and digitize the analog signals coming from the detector - ARC-46 (see Figure 4.14). We run the H2RG detectors in 100 kHz 32-channel mode and acquire images in UTR sampling mode or multiple UTR sampling mode. Typical acquisition times are ~ 2 seconds for each frame.

We have three layers of software that control the ARC hardware. The first layer is assembly code written for a Motorola DSP56300 that set the clocks, biases, and acquisition mode. The second layer is the ARC Application Programming Interface (API) written in C++ which allows the user to acquire multiple images from the detector. The first two layers are the standard software for ARC components (although the DSP code is alterable and can be configured for different detectors). The third and last layer of our software is a custom C++ wrapper developed in our laboratory that can run both of our H2RG detectors either simultaneously or separately on different PCI cards.

We run the software on a Linux computer that can be accessed remotely and is fully dedicated to driving the detectors to avoid timing delays. The Linux computer will communicate over fiber optic cables to the Labview-based RIMAS instrument

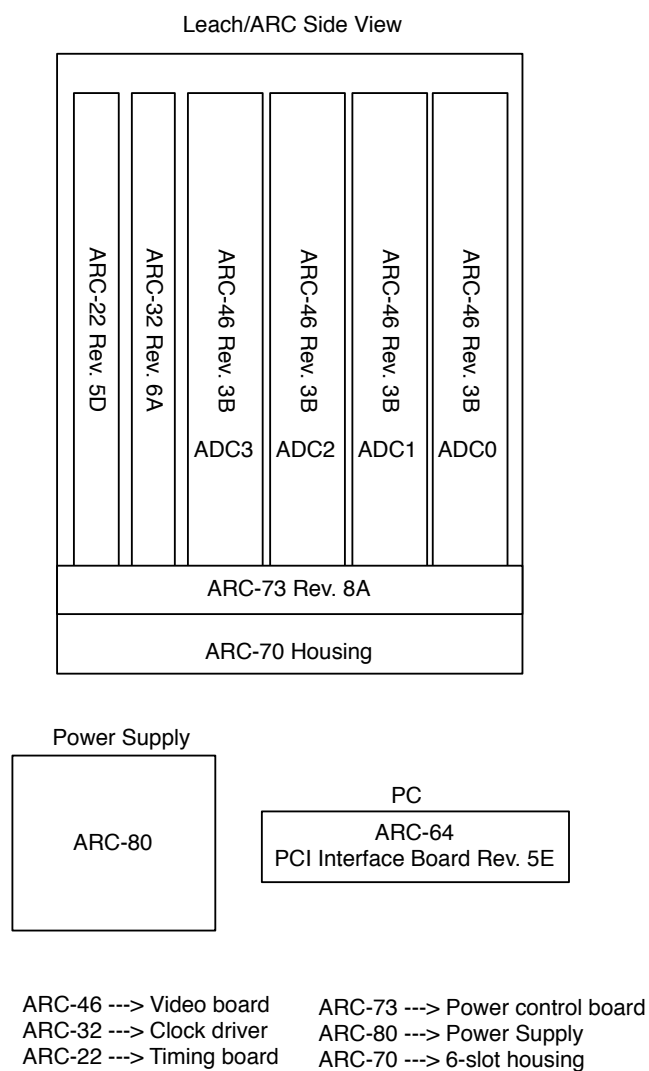


Figure 4.14 Leach/ARC hardware layout that we use to run RIMAS's H2RG detectors. Note that we use two identical sets of hardware, one for each H2RG detector. We have two ARC-64 PCI Interface boards installed in our Linux computer so we can run the detectors separately or simultaneously.

control system.

4.2.3.2 Labview detector driver

We have developed and built our InSb detector driver system based on National Instruments Compact-RIO (cRIO) controller. Our cRIO-9074 utilizes four modules: a high-speed digital I/O - NI-9401, a custom optoisolator, a digital I/O - NI-9403, and an analog-to-digital converter - NI-9223. The cRIO is controlled by a Labview program and acts as both the detector driver and acquisition system (Figure 4.15) in conjunction with three external boards: voltage level setter, programmable bias, and amplifier. We have developed a custom set of Labview programs that are alterable and user-friendly.

This system is very versatile, robust, and can be made using commercial off-the-shelf products. The cRIO-9074 has eight module slots which allows us to use two additional modules to monitor temperature diodes and run a heater in our testbed system. We acquire images from the InSb detector in 4-channel Fowler sampling mode. The cRIO-9074 is a dedicated detector driver and acquisition system that interfaces with the control computer over ethernet.

The clocking patterns are written in an easily alterable ASCII file that are parsed to our cRIO FPGA and transmitted to an external voltage level-setter board via the NI-9401 and optoisolator. The cRIO also generates commands to an external programmable bias board through the NI-9403. Finally, the NI-9223 converts differential analog signals from the InSb detector after they have passed through an

external amplifier. While it has been developed for the 256x256 InSb detector, this set of hardware/software can be modified for other systems due to its modifiable clocks and biases.

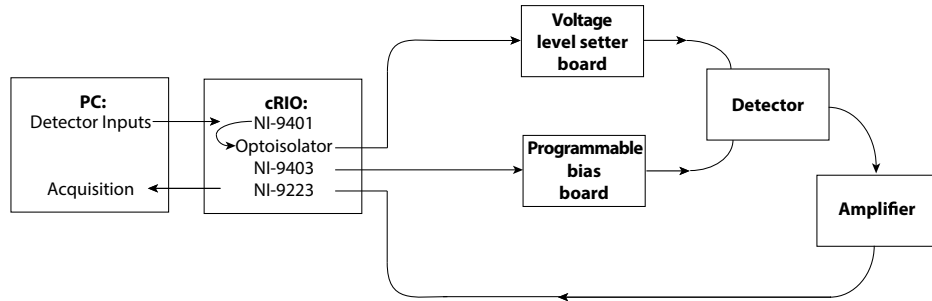


Figure 4.15 Hardware layout of the cRIO and custom bias and level setter boards that we use to run RIMAS's InSb slit-viewer detector.

4.2.4 Detector characterization parameters

Here we describe several important detector characterization parameters that we use to both characterize our detectors and correct our raw readout.

4.2.4.1 Quantum efficiency

The quantum efficiency (QE) of a detector is defined as the ratio of electrons produced for each incident photon on the detector. A perfect detector will convert one photon to one electron and have a 100% QE. However, most detectors have a lower efficiency of 60-80% due to impurities within the substrate which cause imperfect electron-hole recombination and reflection of light. The quantum efficiency is determined by using the detector to measure a well-calibrated source (typically a National Institute of Standards and Technology calibrated source) and compare the

flux of the source with the output of the detector.

4.2.4.2 Conversion gain

In order to detect small signals we use electronic amplifiers for each pixel to amplify the voltage before digitization. The conversion gain indicates how many electrons are in an analog-to-digital unit (ADU) or voltage. The conversion gain combined with quantum efficiency allows us to calculate the flux from a digital number. The conversion gain is typically calculated using the photon transfer method.

The photon transfer method uses the fact that a signal has two main noise sources: photon and readout noise. These sources are independent and random and therefore add in quadrature:

$$\sigma_{e^-}^2 = p_{e^-}^2 + r_{e^-}^2 \quad (4.1)$$

where the subscripts represent the units of the variables (electrons), σ is the total noise, p is the photon noise multiplied by some quantum efficiency, and r is the readout noise.

Assuming the photon noise follows Poisson statistics and the read noise is independent of photon flux, $p_{e^-}^2 = n_{e^-}$ and $S_{mV} = \frac{n_{e^-}}{g}$, where g is a conversion gain, n_{e^-} is the number of detected electrons, and S_{mV} is the mean signal. We can convert from units of electrons to mV by dividing g^2 and rewrite this as:

$$\sigma_{mV}^2 = \left(\frac{S_{mV}}{g} \right) + r_{mV}^2 \quad (4.2)$$

Therefore, we can measure the slope of the signal variance against the median signal to determine the conversion gain. This is the photon transfer technique and it can be used for measurements in voltage or ADUs.

4.2.4.3 Read noise

Read noise or readout noise comes from the non-zero noise from the readout electronics. The main sources of read noise are shot noise, Johnson noise (thermal noise), and $1/f$ noise. Typically the ultimate floor of the total noise in the system is the read noise. In order to reduce read noise we employ different sampling modes described in §4.2.2.1 to reduce random noise.

4.2.4.4 Dark current

Dark current is the small amount of electric current that flows into a detector when there are no photons present. Dark current is dependent on the detector temperature and is caused by Poissonian thermal fluctuations in the substrate releasing electrons and holes in the detector's depletion zone that are then swept away by the electric field to create a current. For bright sources and short exposures this is not a significant source of noise, but can contribute a large amount of photons especially for spectroscopy frames where the number of incoming source photons is small and the exposure time is long.

4.2.4.5 Linearity

If we have a linear detector we can measure a source and then measure a source with 10 times the signal and we should get 10 times the number ADUs. Most detectors are linear to a certain point and then become non-linear as they approach saturation. Each pixel behaves slightly differently, therefore, we need to characterize the linearity of each pixel. If a pixel reads a completely flat number of ADUs with increasing flux we called it a bad pixel; it is unresponsive to light. If a pixel is extremely non-linear and quickly saturates we call it a hot pixel. Hot pixels can often still be used as long as they stay below their saturation point. We can use each pixel's linearity curves to create both a bad pixel map and a hot pixel map as well as correct the signal for linearity differences.

4.2.4.6 Saturation

Saturation occurs when adding more photons does not increase the number of ADUs read out. At this point the potential well is full and the amount of current does not change with increasing photons. Beyond saturation we cannot accurately measure the flux of a source.

4.2.4.7 Dynamic range

Dynamic range is the range between the signal floor (e.g. the read noise) and the signal ceiling (e.g. saturation or point of nonlinearity) that we can measure. This is the range that the detector can measure flux and sources and exposure times

should be chosen to fit within this range.

4.2.4.8 Persistence

Persistence is when charge is trapped after the detector is exposed to a very bright source. This signal persists after the bright source is out of the field of view and even after the detector array is reset. Persistence is caused by traps within the active diode regions which eventually allow electrons or holes to tunnel back to the photosensitive material to create afterimages. Persistence is typically measured both as a measure of time and exposure signal.

4.2.5 RIMAS H2RG Detectors Characterization

We report the laboratory characterization of the RIMAS detectors at cryogenic temperatures: conversion gain, linearity, saturation, read noise, dynamic range, and dark current. We did not have enough time to measure the quantum efficiency or persistence. The results are summarized in Table 4.1 and the analysis is explained in detail in the remainder of this section. We note that we have received a replacement detector for the YJ detector due to a large ramp in the dark current described in this section. The replacement detector is in the process of being fully characterized. To avoid confusion we refer to the original YJ detector as “YJ Detector A” and the replacement detector as “YJ Detector B”. We report the available characterization data for YJ Detector B.

Table 4.1 RIMAS H2RG Detector Characteristics

Characteristics	YJ Detector A	YJ Detector B	HK Detector
Conversion gain (e^-/ADU)	4.00 ± 0.06	...	4.40 ± 0.03
^a Read noise (e^-)	8.73 ± 0.15	...	7.67 ± 0.05
Saturation (ADU)	37,725	...	32,467
Dynamic range (dB)	42.5	...	42.7
Dark Current ^b (ADU/s)	$5e-2^c$	$3e-4$	$2e-4$

^aRead noise reported for Fowler 16 and error from conversion gain.

^bTested at $\sim 80\text{K}$.

^cWas tested before baffles installed so likely dominated by light leak.

4.2.5.1 H2RG Detectors: Conversion Gain

We measure the conversion gain with an LED source outside the dewar window with diffusers to create a uniform source of illumination. We take six datasets with UTR 128 and exposure time of 500ms between each frame with filters in front of the detectors.

We first subtract the first frame from all subsequent frames in each dataset, then subtract another dataset frame-by-frame; this removes any large source variation. Note that there are still low levels of non-uniformity because the source is not perfectly uniform. In order to mitigate this effect, we only use a small 100x100 pixel box near the center of the detector to calculate the conversion gain.

We use the photon transfer technique to measure the conversion gain. We calculate the variance in the difference frame (corrected for a factor of two due to

the increase in noise from subtracting the other dataset) and mean signal and plot in Figure 4.16. Note that in Figure 4.16 the conversion gain (inverse of the slope) starts to drift at larger median signals. This is likely due to the non-uniformity of the source becoming more significant with larger signal; however, the deviation is $< 7\%$ which indicates this is a minor non-uniformity. We mitigate this effect by only using the first five points (where the slope is linear). We perform a linear regression over five difference datasets and report the conversion gain in Table 4.1.

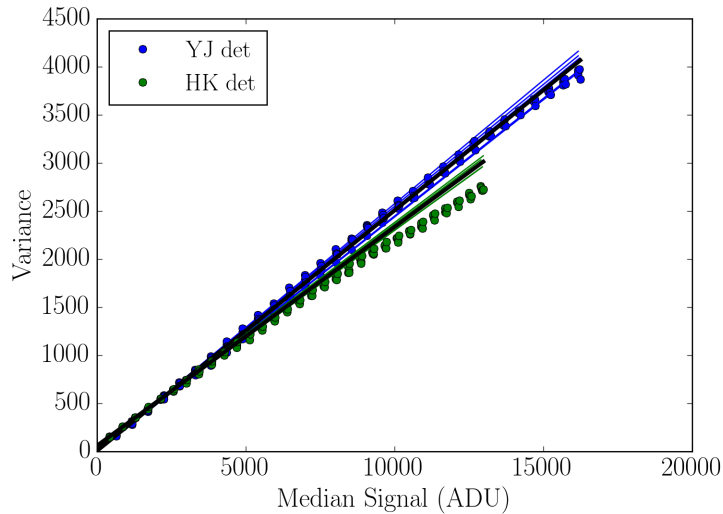


Figure 4.16 Conversion gain for YJ detector A and HK detector from 100x100 pixel boxes near the center of the detectors. Note the drift from linearity at higher signals is likely due to small non-uniformity in the signal becoming more significant with more signal. The largest deviation in the gain is $< 7\%$, but we only calculate the conversion gain from the lower signal region (first five datapoints) and fit all five difference datasets to avoid this non-uniformity.

4.2.5.2 H2RG Detectors: Linearity and Saturation

In order to measure the linearity and saturation of our detectors, we place an LED source outside the dewar window with diffusers to create a uniform source of

illumination. We use the same data as the conversion gain calculation (see §4.2.5.1). Large scale variations are removed by subtracting the first frame from all subsequent frames of each dataset. Our analysis is limited to a 500x500 pixel box near the center of the detector to reduce signal variation. We perform a linear regression for the first two datapoints on each pixel within the box to determine the bias voltage and offset each pixel by this amount to effectively force each pixel to start at 0 ADUs. We then perform a second linear regression for the first six datapoints (this is within the linear regime for most pixels). The middle pixel of the 500x500 pixel box acts as a reference pixel and we scale the slopes of all other pixels to match this reference pixel; this corrects for different scaling factors between pixels. We plot the median signal in both ADUs and electrons (using the conversion gain in §4.2.5.1) for both detectors in Figure 4.17. The detectors start to deviate from linearity around $\sim 20,000$ ADU.

For strong signals, the detectors become extremely non-linear. The saturation point is different for each pixel so we take the last frame of a single UTR 128 dataset and subtract the first frame. We only look at the 500x500 pixel box we defined for our linearity measurements and fit a Gaussian function to a histogram of the signal in ADUs (see Figure 4.17). We report the saturation from the mean of the Gaussian fit in Table 4.1. We note that we see an increase in the saturation point at lower temperatures.

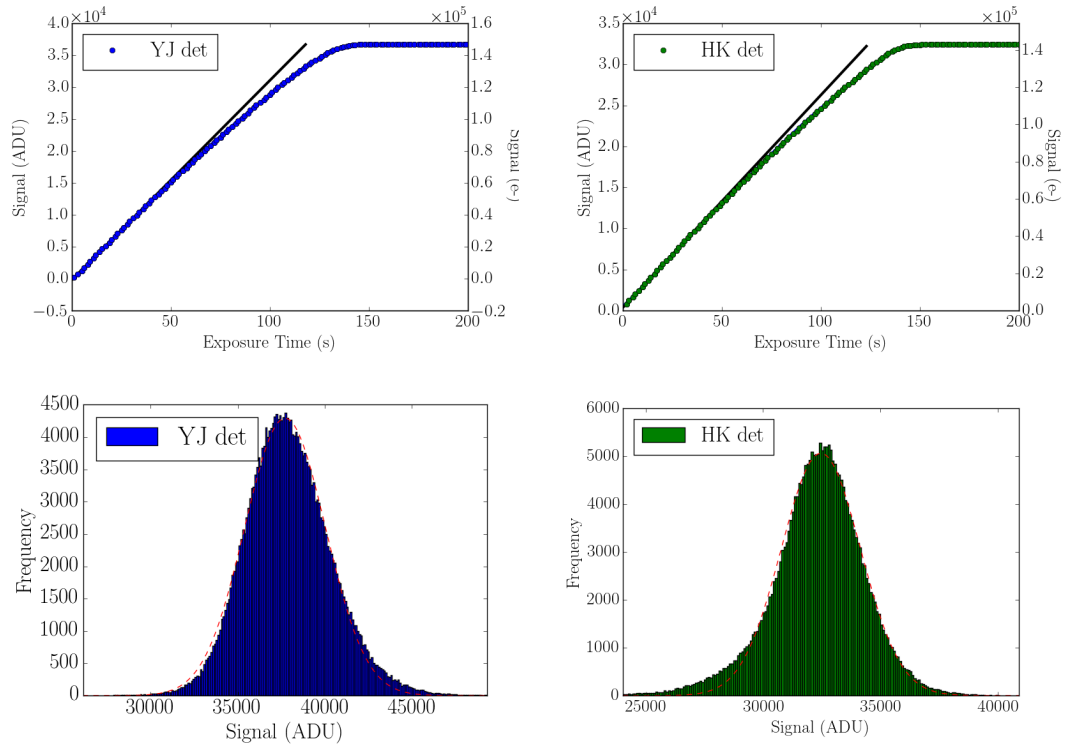


Figure 4.17 (*top*) Linearity of median of 500x500 pixel box for YJ detector A and HK detector. Pixels have been corrected for bias voltages and different scaling factors between pixels. Black lines are linear fits to the first six frames. Detector starts to behave non-linearly around $\sim 20,000$ ADU. (*bottom*) Saturation point of last frame for the 500x500 pixel box of the detector. We fit a Gaussian distribution (red) to get an estimate of the saturation point of the detectors.

4.2.5.3 H2RG Detectors: Read noise

We calculate the read noise from two identical datasets with UTR 255 and exposure times of 500ms between each frame while the detector is cold and dark. We make a pseudo-Fowler set by breaking the UTR 255 frames into Fowler sets using the first and last 2, 4, 8, 16, 32, and 64 frames for Fowler sets of 1, 2, 4, 8, 16, and 32 respectively. We do this because read noise is commonly reported by Fowler number. In order to calculate the read noise we calculate the variance of each pixel as a function of Fowler number. This is done by first subtracting the median of the pedestal frame per pixel and from the median in the signal frame per pixel. We perform a $3\text{-}\sigma$ clip on the data and calculate the variance across the difference frame, correcting the variance by a factor of two due to the increase of variance from subtracting two datasets. We report our H2RG detector read noise in Figure 4.18 and the read noise for Fowler 16 in Table 4.1. The increase in read noise for Fowler 64 and 128 is from the source noise dominating over the read noise.

4.2.5.4 H2RG Detectors: Dynamic Range

The dynamic range of a detector is set at the low end by the read noise and at the high end by the saturation. We report the dynamic range of both our detectors in Table 4.1 using our reported conversion gain.

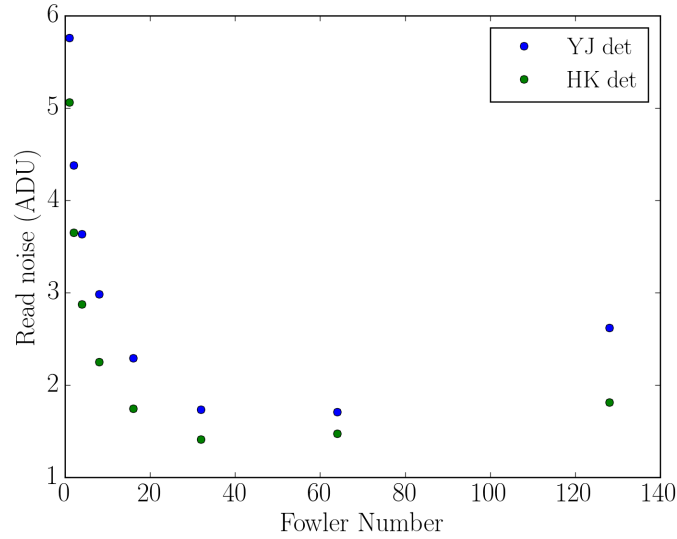


Figure 4.18 Read noise for YJ detector A and HK detector. The increase in read noise for Fowler 64 and 128 is from the source noise dominating over the read noise.

4.2.5.5 H2RG Detectors: Dark Current

We measure the dark current while the detector is cold ($\sim 80\text{K}$) and dark with UTR 255 with exposure times of 200s between frames. This is a total integration time of ~ 14 hours. We perform a linear regression on the reference pixels along the columns and subtract the fit from the entire array. This corrects for slowly varying electrical noise in time and across the detector. We subtract the first frame from all subsequent frames to remove fixed pattern noise. The dark current is shown in Figure 4.19 and Table 4.1. Typically dark current is reported in e^-/s but we report it here in ADU/s because the YJ detector B conversion gain has not yet been measured.

Our measurements of YJ detector A dark current were taken prior to installed baffles around the detectors and are likely dominated by a light leak, however, we

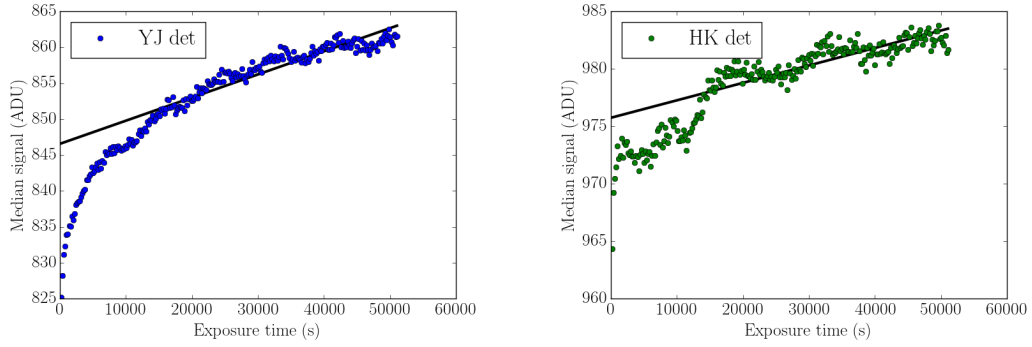


Figure 4.19 (*top*) Dark current for YJ detector B (left) and HK detector (right). There are dark current ramps in both detectors from ADC biases settling after the initial start up. The ramp can be reduced by waiting an hour after initializing the detectors before acquiring data. The HK detector has additional noise on top of the dark current likely originating from the detector driver electronics or thermal fluctuations.

plan on replacing YJ detector A because there was evidence of a persistent non-linear ramp that is associated with a known problem with the barrier layer of this batch of detectors. However, despite the ramp and noisy signal, the dark current measurements on the YJ detector B and HK detector are consistent with similar H2RG detectors measurements of $\sim 0.005 \text{ e}^-/\text{s}$ measured at 100K; our dark current is lower which is expected since our detectors are measured at a lower temperature of $\sim 80\text{K}$.

For the YJ detector B and HK detector, there is a “ramp” in the dark current in Figure 4.19 that is likely due to a non-trivial settling time of the ADC bias levels with the Leach/ARC electronics. This “ramp” can be reduced both in time and in amplitude by adding a long delay time (~ 60 minutes) after initializing the detectors to allow time for the ADC biases to settle. There is an additional noise on the HK detector dark current. The noise level is quite small (~ 2 ADU) primarily due to noise on the detector driver electronics or thermal fluctuations.

Table 4.2 RIMAS InSb Slit-viewer Detector Characteristics

Characteristics	InSb slit-viewer detector
Conversion gain (e^-/mV)	48.77
^a Read noise (e^-)	14.71
^b Saturation (mV)	3,264
Dynamic range (dB)	40.35

^aRead noise reported for Fowler 16.

^bReported for 10% deviation from linearity.

4.2.6 RIMAS InSb Detector Characterization

We report the laboratory characterization of the RIMAS InSb slit-viewer detector at cryogenic temperatures. The InSb detector is used for guiding on the slit and only needs to identify bright objects, therefore, we only characterize conversion gain, linearity, saturation, read noise, and dynamic range. We did not have time to perform quantum efficiency and persistence measurements. The results are summarized in Table 4.2 and the analysis is explained in detail in the remainder of this section.

4.2.6.1 InSb Detector: Conversion gain

We measure the conversion gain using room lights with a diffuser in front of our dewar window for our uniform source. The five datasets are taken with Fowler 16 for 11 different exposure times (0.1s, 2s, 10s, 20s, 50s, 70s, 100s, 110s, 125s, 150s,

200s). The exposure times were chosen so we could see the detector saturate.

We use the photon transfer technique to measure the conversion gain and remove pixel-to-pixel variation by subtracting two datasets with the same exposure time. Despite flat fielding the image, there is still non-uniformity because some hot or dead pixels do not subtract out perfectly. We exclude these pixels by visually examining the image and selecting a smaller area (50x50 pixels) that is visually uniform. We plot the mean signal vs. variance in Figure 4.20 and report the conversion gain in Table 4.2. The variance is corrected for a factor of two from the increase in noise due to subtracting two datasets.

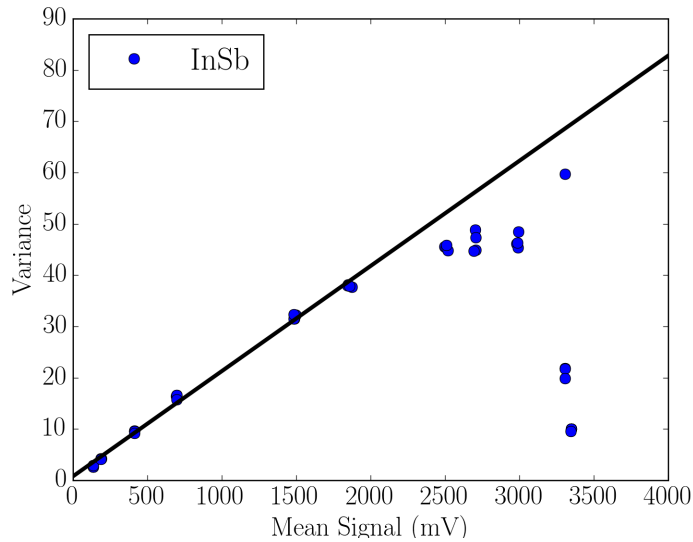


Figure 4.20 Conversion gain for InSb slit-viewer detector for 50x50 pixel box. Non-linear behavior starts at ~ 2500 mV and completely saturates at ~ 3300 mV.

4.2.6.2 InSb Detector: Linearity and saturation

In order to measure the linearity and saturation of our detector, we place a light bulb with a diffuser to create a uniform source of illumination. We acquire a

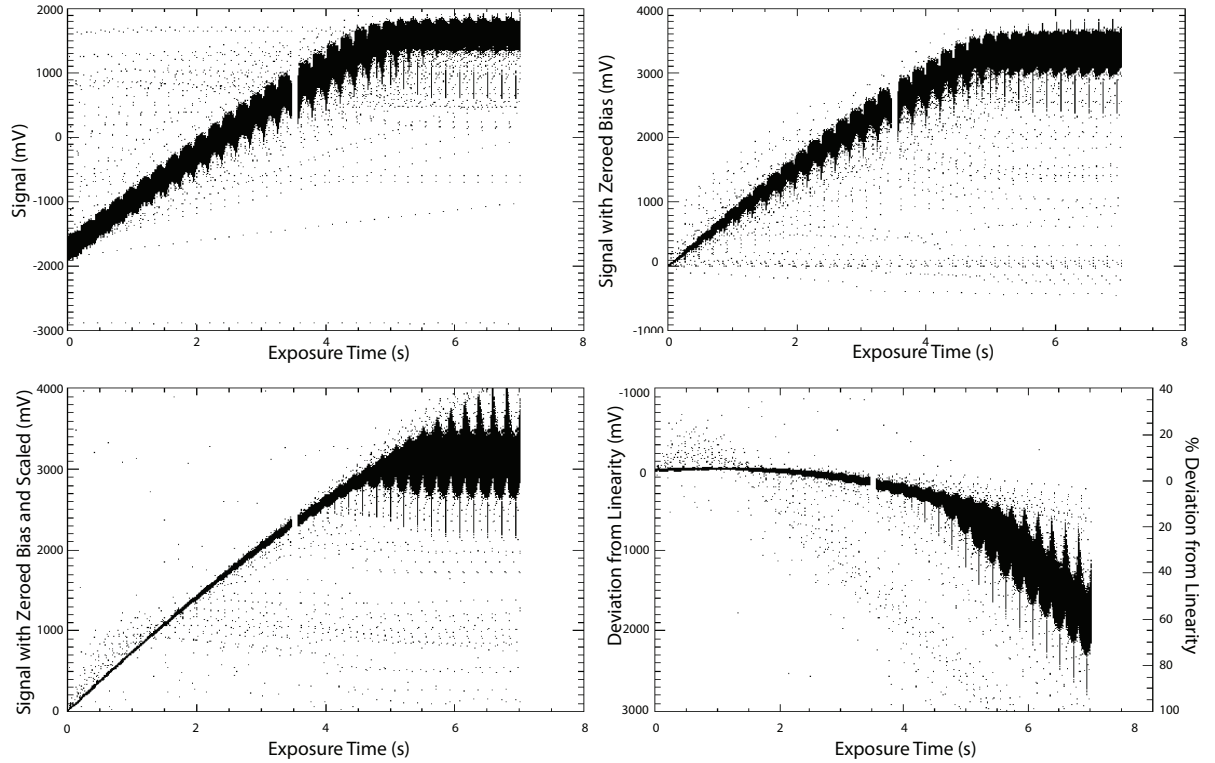


Figure 4.21 Linearity from Fowler 16 acquisition. Each black dot represents a pixel for the 32 frames taken, the gap in data at ~ 3.7 s is a 0.1s exposure time for the Fowler sampling. (*upper left*) The raw data. (*upper right*) The data with the signal offset removed. (*bottom left*) The data scaled to the linear fit of the first pixel in the array. (*bottom right*) The deviation from linearity in mV and percent. If we ignore the outliers, we can see that there is a large spread in the well depth.

dataset with Fowler 16 and a short integration time of ~ 0.1 seconds. We plot the exposure time against the measured signal for each pixel for the 32 images from a Fowler 16 acquisition in Figure 4.21. In order to remove each pixel's bias, each pixel is fit with a linear regression for the first two datapoints and is forced to start at 0V. This removes effects from the non-uniformity of the source and the readout circuitry variation between pixels. Each pixel has a different gain, so each pixel's gain is scaled by the slope of the first pixel in the array.

The data in Figure 4.21 are tightly bunched for early exposure times but have

a wide spread at saturation (~ 1000 mV) because while the pixels appear to be well fit to the first pixel in the linear regime, the pixels strongly deviate in the non-linear regime. This allows us to measure the pixels' deviation from linearity. We call the point where the detector deviates 10% from linearity the saturation point. This is reported in Table 4.2.

4.2.6.3 InSb Detector: Read Noise

We calculate the read noise by measuring the variance of the detector as a function of Fowler number while the detector is cold and dark. We use 10 bias frames for each Fowler number (1, 2, 4, 8, 16). We only use a small area of the detector (20x50 pixels) which has low levels of illumination. We subtract the pedestal and signal frames and calculate the standard deviation from a mean subtracted frame of the 10 bias frames. The variation has been corrected by a factor of two due the increased noise from subtracting the mean signal.

The read noise for each Fowler number is shown in Figure 4.22. We also report the read noise for Fowler 16 in Table 4.2. Note that the increase in read noise at Fowler 16 is because the signal noise starts to become more significant with the long exposure times associated with higher Fowler numbers. Note that the read noise does not decrease as a function of \sqrt{N} which is expected for white noise dominated read noise. This discrepancy can be attributed to periodic pickup noise and higher Fowler frames starting to pick up signal due to longer acquisition times. However, this detector will primarily be used to identify bright objects and will not be read

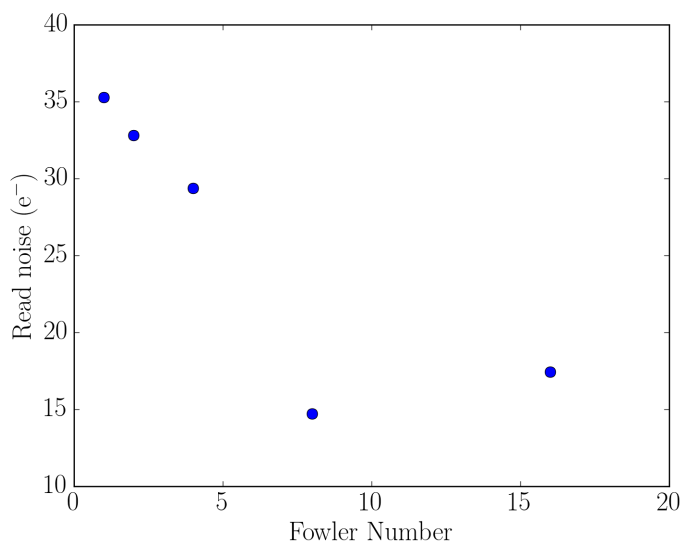


Figure 4.22 Read noise drops off with larger Fowler number. Can decrease the readout noise by taking more frames with a tradeoff in acquisition speed. Note that for Fowler 16 there is an increase in read noise, this is due to the long acquisition times for higher frames starting to pick up signal.

noise limited.

4.2.6.4 InSb Detector: Dynamic Range

The dynamic range of a detector is set at the low end by the read noise and at the high end by the saturation. We report the dynamic range of our slit-viewer detector in Table 4.2 using our reported conversion gain.

4.2.7 Troubleshooting near-infrared hybrid detectors

In this section we outline some techniques to troubleshoot near-infrared hybrid detectors. Hybrid detectors are complex and can be difficult to debug because NIR detectors must be run at cryogenic detectors due to thermal noise. However, there are some straightforward tests to run both at room temperature and at cryogenic

temperatures to ensure that the detector is operating properly.

4.2.7.1 Testing detector driver systems

The first step is to perform a thorough safe-to-mate: attach all harnesses to the detector driver systems without the detector and verify both the biases and clocks on the harness the detector will be attached to. The most important checks during a safe-to-mate are that the bias levels match the voltage level set in the detector configuration files and that the clocks have the correct logic voltage levels. These should also be referenced against the detector manuals which specify the range of acceptable bias and clock logic levels. If the bias and clock signals are unacceptable, methodically work backward from the cable that connects to the detector all the way to the computer running the detector driver system. In particular, harnesses should be checked for shorts and miswiring and the detector configuration file modes should be set properly. For example, the detector may be hardwired for a particular configuration which must be specified in the configuration file or the detector will not properly read out. Once the biases and clocks are verified, attach the detector. The detector should never be attached without first doing a safe-to-mate check.

4.2.7.2 Testing detectors at room temperature

The next step is to attach the detector and run at room temperature. Figure 4.23 shows two raw detector frames. These are uncorrected other than de-interlacing the detector readout. The most obvious sign that the detector is reading properly

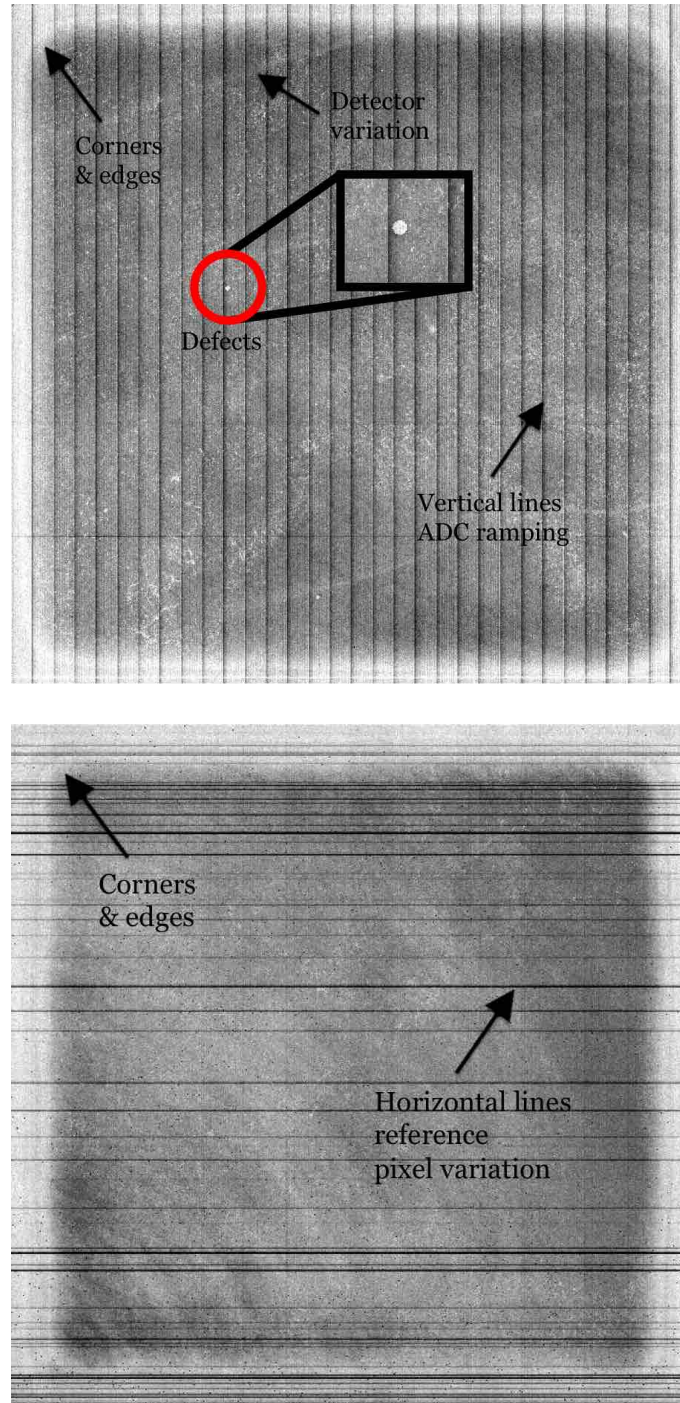


Figure 4.23 Two raw hybrid detector frame examples at room temperature. The picture frame pattern around corners and edges of the detector is highlighted in both frames. There is also large scale variation across both detectors frames from differences in crystal growth. In the red circle and inset is an example of a detector defect. Any of these features can be used to identify if a detector is operating properly at room temperature. Additionally, the black horizontal and vertical lines are caused by reference pixel variation and ADC ramping respectively. These lines are not necessarily useful in determining detector operability and can be removed with flat-fielding.

is that the corners and edges of the detector array have a “picture frame” pattern on the raw frame readout. This pattern comes from the edges of the detector substrate not adhering as well to the ROIC away from the center of the detector. The detector will also show signs of wide scale variation which comes from the way the crystal structure grows on the detector substrate. Detector variation is different for each detector but is an obvious indicator that the detector is being read out properly because the patterns stretch over large areas of the detector. Another indicator that the detector is being properly readout are signs of obvious defects on the detector. Not all detectors will have large defects, but it can often be a way to identify a specific detector from raw images. Figure 4.24 is an example of an unconnected detector. In this case, the readout columns are all flat and featureless. This type of image can occur if the detector is not attached properly to the harness or if the detector configuration files do not match the hardwired configuration on the detector.

We see some features in our own system that can easily be removed with flat-fielding. For example, in the top image in Figure 4.23 there are vertical lines at the beginning of each readout channel. This comes from ADC ramping and can be minimized by waiting for the ADCs to settle. Additionally, the randomly dispersed horizontal lines in the bottom image in Figure 4.23 can be removed with flat-fielding. This may be specific to our system because we set the ADC bias levels based on the vertical reference pixels. If those reference pixels are at slightly different levels than each other they will cause horizontal lines through the detector image. Both of these problems can be mitigated with flat-fielding or just simply subtracting the

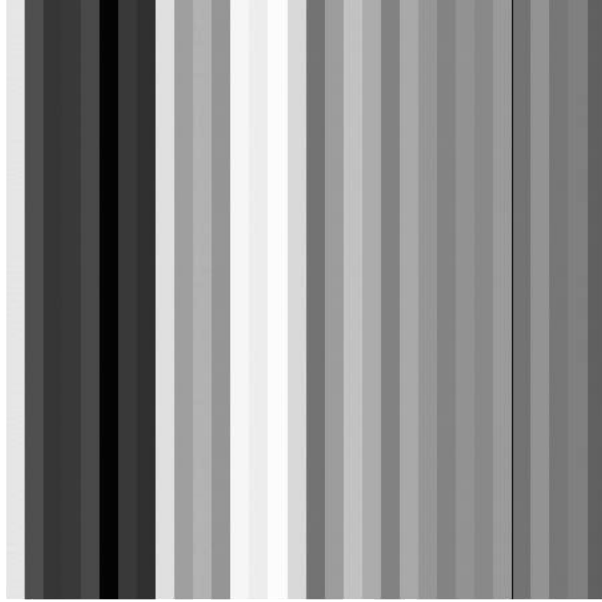


Figure 4.24 An example of an unconnected detector. Note that while the readout columns vary between each readout channel, the columns are all flat and featureless. This type of raw frame indicates that the detector is not connected or the detector driver has not been configured properly for a specific detector.

pedestal frame of the dataset.

Next, we have discovered that our NIR detectors respond to very bright sources even at room temperature. We move the source across the detector at room temperature to ensure that the detector is reading out properly. We have used this to aid in aligning optics at room temperature and debug problems with the detector. For instance we had a persistent problem where readout channels would appear as a superposition of multiple readout channels (see Figure 4.25). We were able to quickly debug the problem once we discovered we could test at room temperature. The problem was crosstalk in one particular harness, once this harness was rewired the problem went away.

At room temperature we saw two prevalent problems. One was a ramping signal over all readout channels at the beginning of a frame (Figure 4.26). This was due

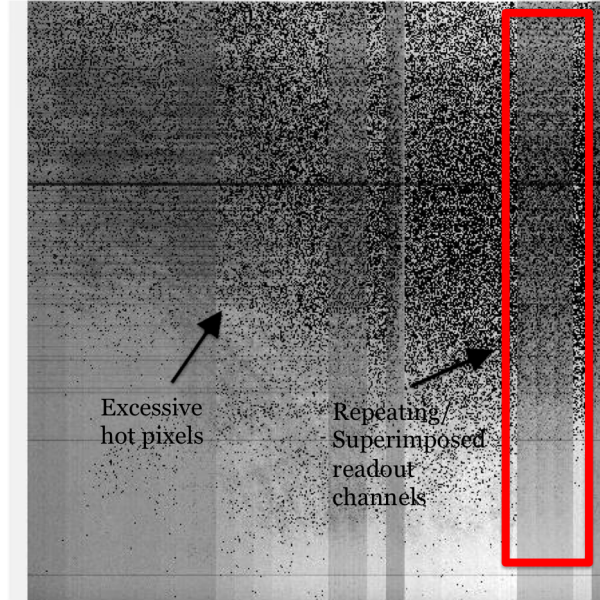


Figure 4.25 Example of a degraded detector at ~ 65 K. There are a large number of hot pixels. This frame also suffers from a superposition of readout channels caused from crosstalk within a harness (shown in red). A typical detector readout should not show these features.

to ADC levels taking a non-negligible time to settle after changing ADC bias levels. Originally when we ran the acquisition system we would turn the detector driver on, set the ADC biases, acquire, and then turn the detector driver off. The first frame would show this prominent ramp, but placing a delay between setting the ADC biases and acquiring a frame completely removed the ramp. We suggest allowing settling time every time the ADC biases are altered significantly and additionally suggest waiting at least 60 minutes to acquire an image after turning on the detector driver systems in order to allow the entire system to settle (this is particularly true for the Leach/ARC systems). The other problem we saw at room temperature was that some readout channels sporadically jumped values in the middle of an image (Figure 4.27). This ended up being a small problem in the ADC board software that has been corrected.

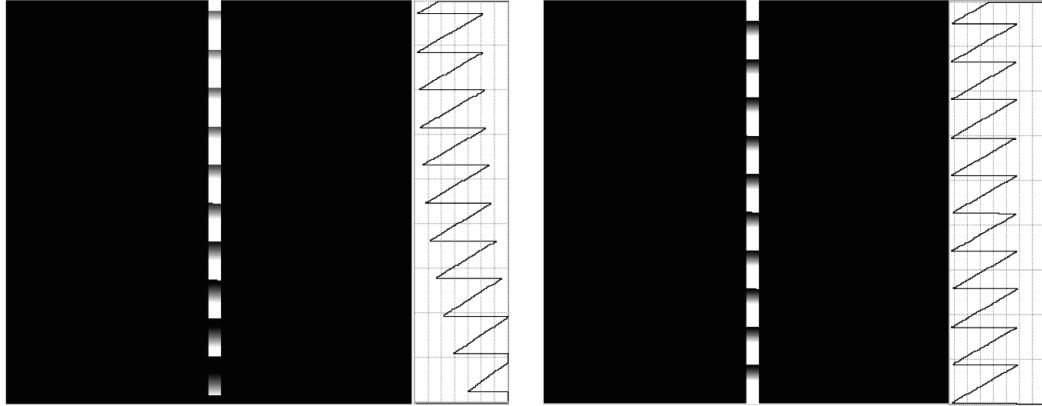


Figure 4.26 Example of ramping signal from ADC bias levels. Both frames are taken with a function generator with a sawtooth signal attached to an input channel of a detector driver. The signal changes in amplitude on the left because the ADC biases are still changing during the readout. The frame on the right is taken after a five second delay that allows the ADC biases time to settle.

4.2.7.3 Testing detectors at cryogenic temperatures

At cryogenic temperatures, the most prominent features to identify are hot pixels. As the temperature decreases, the number of hot pixels should drastically reduce because they are more sensitive to dark current. At operating temperature the detector should only have a few percent hot pixels. Figure 4.25 shows a detector image at operating temperature of $\sim 65\text{K}$ with a very large amount ($> 10\%$) of hot pixels. This is a sign of detector degradation and this particular detector came from a batch of detectors that has a known defect in the barrier layer (Rauscher et al., 2011, 2014).

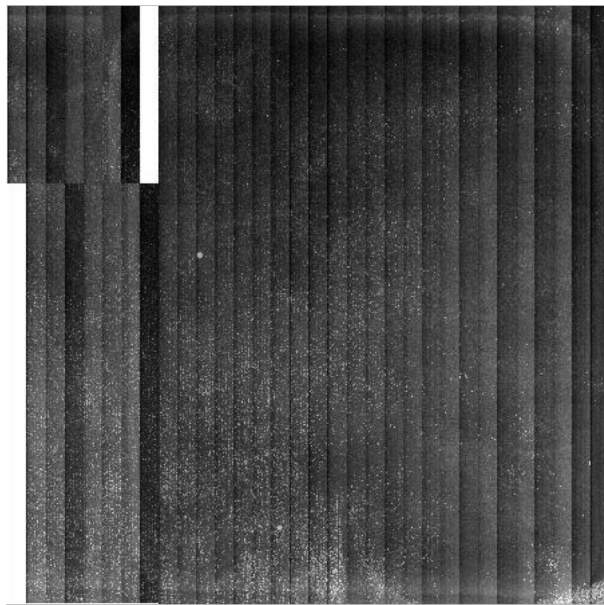


Figure 4.27 Example of column splitting. There is a sudden change in the column readout. This type of problem was due to a software bug in the ADC board.

Chapter 5: RIMAS: Software

Throughout this thesis we have built several software products for RIMAS and other instruments. The following chapter presents these publicly available products.

5.1 RIMAS Quick Reduce Data Pipeline

We have created a quick data reduction pipeline for RIMAS that takes the raw detector science frames from a single H2RG detector acquisition and returns one result frame. The pipeline is available on GitHub¹ and can be run in several configurations.

RIMAS’s H2RG detectors have a border of four reference pixels around the detector that are not illuminated and can be used for common noise rejection. We allow the user to scale each raw image by the reference pixels in five different ways: no correction, removing the median of each column’s reference pixels from a column (“col_med”), removing the median of each row’s reference pixels from a row (“row_med”), perform a linear fit on the top and bottom reference pixels in a column and remove the fit line from a column (“col_allslope”), and perform a linear fit on the median of the top and the median of the bottom reference pixels in a column

¹https://github.com/vickitoy/rimas_quickreduce

and remove the fit line from a column (“col_medslope”). The corrected raw frames are then cropped to exclude the reference pixels.

The user can then specify the acquisition sampling mode, either UTR sampling or Fowler sampling. For UTR sampling we perform a least squares linear regression on each pixel as a function of time. The result frame is the product of the total integration time and the slope of the linear fit. Due to problems with the “ramping” ADC biases described in §4.2.5.5, we also have implemented frame rejection which ignores a particular raw image if the difference between subsequent frames is above $1\text{-}\sigma$. This allows us to reject frames that are largely impacted by the ADC bias ramp.

For Fowler sampling we split the raw images in half and calculate the median of each pixel over the first half of the acquisition (pedestal) and the median of each pixel over the second half of the acquisition (signal). The result frame is the difference of the pedestal and signal frame. Note that the Fowler sampling does not generally require frame rejection because the pedestal and signal frame use the median of a group of frames.

5.2 Generalized Photometric Data Reduction Pipeline

We have created a generalized photometric data reduction pipeline. This pipeline is based on a custom pipeline for the Keck Low Resolution Imaging Spectrometer (LRIS) developed by Dan Perley², but we have made substantial changes to the original pipeline. While we will not list all the changes to the pipeline here, the

²<http://www.dark-cosmology.dk/~dperley/code/code.html>

changes have been well documented in our GitHub developmental pipeline repository³. Some of the major changes include migrating the pipeline from IDL to Python, modularizing the code, reducing the runtime of the pipeline by a factor of two, generalizing the pipeline to work with multiple instruments, improving the astrometric solutions, and including instrumental zeropoint correction errors.

The generalized pipeline is entirely open-source and the most recent version is publicly available on GitHub⁴ (this is a migrated version of the developmental pipeline). The pipeline is written in Python and makes use of multiple Astromatic packages (SExtractor - Bertin & Arnouts 1996, SCAMP - Bertin 2006, SWarp - Bertin et al. 2002, MissFITS - Marmo & Bertin 2008) as well as standard Python packages (numpy, scipy, pyfits, astropy - Astropy Collaboration et al. 2013). The pipeline comes with a source bash script that automatically verifies that all the Astromatic packages are installed and adds the pipeline Python code to the system Python path.

The pipeline can be run autonomously or can be run manually with user interaction. We break the pipeline into three separate components: preprocessing, data reduction, and photometry. The pipeline is written such that the only instrument specific component is in the preprocessing stage. All subsequent components assume that the data is formatted correctly.

³<https://github.com/cenko/RATIR-GSFC>

⁴https://github.com/vickitoy/photometry_pipeline

5.2.1 Preprocessing Stage

The preprocessing component of the pipeline uses a defined class based instrument structure that allows the user to process data from any photometric instrument. The instrument class is made up of abstract methods that allow freedom in defining different methods for individual instruments but creates a structure for the rest of the pipeline to follow. Each instrument inherits this generalized instrument class and a class is defined for each new instrument that the pipeline can use.

In the preprocessing stage, the pipeline takes the raw calibration and science frames and formats the file name, fits header, and crops the frame according to the defined class methods for the specified instrument. Additionally, the calibration and science frames can be selected either manually or automatically. The user can set limits on the pixel values of the frames based on percentage of saturation and can also automatically reject any frame with saturated pixels. At the end of the selection phase, the script will display all images for inspection. This section of the pipeline also can be used to make master calibration files (bias, dark, flat) by calculating the sigma-clipped median for each pixel.

5.2.2 Data Reduction Stage

The bulk of the pipeline is the data reduction stage which begins with automatically setting paths for the Astromatic software and setting file naming conventions from the user defined parameter file called “pipeautoproc.par”. These parameters and others are saved into a Python dictionary that is passed to all subsequent steps

in the data reduction stage.

The data reduction stage consists of seven possible steps that can be run autonomously. The user can select which steps to run using the keywords “only”, “start”, “stop”, or “step”. This gives the user the freedom to interrupt the pipeline at any stage, rerun steps, or only run small portions of the pipeline. The data pipeline component can also run in quiet mode, which displays minimal outputs, and is entirely modularized making it easy to understand and debug. Finally, we have increased the data reduction speed by a factor of two, resulting in a robust and fast data reduction pipeline.

The pipeline assumes that the master calibration files are in the folder where the data will be reduced. Step (1) is the “prepare” step. During this step the pipeline performs dark and bias subtractions for cameras with master darks or biases in the reduction folder. The pipeline also removes extraneous FITS header keywords in this step and saves the altered files with a prefix “p” to denote that the files have been prepared. Step (2) is the “flatten” step. During this step the pipeline divides the images by a master flat based on the filter specified in the FITS header of each image. The processed images are saved with a prefix of “f” to denote that the files have been flat-fielded.

Step (3) is the “makesky” step. During this step the pipeline makes a master sky flat for each filter. First the pipeline masks out saturated pixels for each image with the same filter FITS header keyword. Then the sources within each image are identified and masked by performing an iterative sigma-clipping using a specified object threshold. Finally, the master sky flats are made from a sigma-clipped median

of each pixel from a 3-D array of images for that filter with the saturated and source pixels masked out. Step (4) is the “skysub” step. During this step the master sky flat is scaled to and subtracted from each image. Then the each image is normalized to zero and the processed images are saved with a prefix of “s” to denote that the files have been sky-subtracted.

Step (5) is the “crclean” step. During this step the pipeline models and removes cosmic rays from each image using an open- source Python script⁵ that makes use of the Laplacian edge detection method described in van Dokkum (2001). The processed images are saved with a prefix of “z” to denote that the files have been cosmic ray zapped.

Step (6) is the “astrometry” step. During this step the pipeline calculates and applies astrometric solutions that account for offset and distortion. The astrometric solutions are created first using a coarse correction from pair-distance matching and asterism matching and then secondly using a fine correction from Scamp. This creates better astrometric solutions because Scamp will fail if the astrometric solution is not close enough to the actual solution and the pair-distance matching cannot accurately account for distortion. The processed images are saved with a prefix of “a” to denote that the files have astrometric solutions applied.

Finally, step (7) is the “stack” step. During this step the pipeline coadds all the images of the same target and filter using SWarp and calculates the instrumental zeropoint. In order to calculate the instrumental zeropoint, we create spectral energy distributions (SEDs) for ugrizyBVRIJHK filters by combining catalogs from the Two

⁵http://obswww.unige.ch/~tewes/cosmics_dot_py/

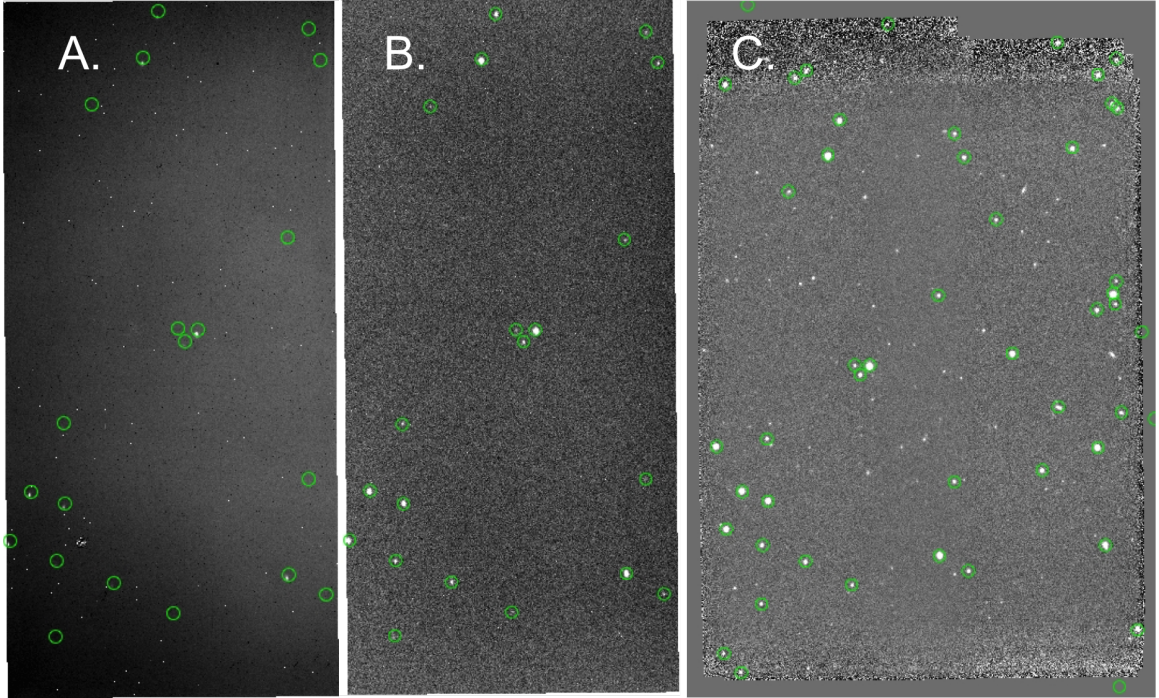


Figure 5.1 Example of pipeline processed images from RATIR’s J-band camera aligned with World Coordinate Systems. Overlaid in green circles are 2MASS catalog sources within the field. (A) A cropped raw J-band image. Note that the astrometry has not been corrected. (B) A full corrected J-band image (an “azsfp” frame). (C) A stack of all the J-band images for this particular target. The coadded image is a stack of dithered frames so the field is larger than the single images shown in (A) and (B).

Micron All Sky Survey (2MASS; Skrutskie et al., 2006) and either Sloan Digital Sky Survey (SDSS; Aihara et al., 2011), AAVSO Photometric All-Sky Survey (APASS⁶), or USNO-B1 (Monet et al., 2003) in that preferred order. We then calculate the difference between SExtractor aperture photometry and the catalog photometry. Robust statistics are used to remove outliers and the instrumental zeropoint and associated error are written into the FITS header file. The coadded frames are saved with a prefix “coadd” and saved with a median timestamp of the stacked images as well as the target name and filter name.

⁶This research has made use of the APASS database, located at the AAVSO web site. Funding for APASS has been provided by the Robert Martin Ayers Sciences Fund.

If all the steps are run, the final corrected individual image will have prefix “azsfp”. The pipeline will print the names of any failed images to the console after processing all the data. The pipeline can be run so that after each step is complete, the previous steps’ files are removed to save hard drive space. The pipeline requires all steps to be run to proceed to the photometry stage except the cosmic ray zapping step may be skipped with an optional flag. Additionally, the pipeline can be run to not produce a master sky and instead simply subtract the median of entire frame. Figure 5.1 shows an example of processed images from the pipeline for the J-band camera of the Reionization and Transients InfraRed camera/telescope (RATIR).

5.2.3 Photometry Stage

In the photometry stage, the pipeline assumes that the stacked images have been produced using the data reduction stage. The pipeline performs aperture photometry with SExtractor using apertures that match the seeing. A composite color image is created using SWarp by stacking all the filter images for the same target. The pipeline creates an html page with the composite image along with each filter image labeled with all the objects in the field. The html page displays a photometry table that contains the photometry for each filter of every object. This table also includes errors from the instrumental zeropoint correction.

5.2.4 Pipeline Applications

The pipeline has been tested on two different photometers: RATIR and LMI. We have compared our pipeline’s results with the automated RATIR pipeline (which does not make quality cuts) and produce similar photometric results. However, our pipeline includes instrumental errors, so our errors are larger but represent more realistic associated errors. Additionally, we have compared our generalized photometry pipeline’s results to our LMI custom IRAF pipeline and produce similar photometric results. Finally, we have written an instrument class for RIMAS and it will be tested once the instrument is commissioned.

5.3 RIMAS Instrument Throughput Models

We created instrument throughput models for all three observing modes. Following the light path for the instrument we include (1) atmospheric transmission efficiencies from Kitt Peak (Hinkle et al., 2003), (2) reflection efficiencies from the telescope’s primary and secondary mirrors, (3) transmission efficiency estimates for the dichroic beam splitter in the center of the instrument cube, (4) transmission efficiencies through windowed surfaces, (5) slit transmission efficiencies for low- and high-resolution spectroscopy, (6) transmission efficiencies through collimator (five AR coated lenses), (7) either reflection or transmission efficiencies through dichroic beam splitter, (8) reflection efficiencies only for mirror on redder optical arm (95%), (9) transmission efficiencies through filter (for photometry), grating (for low-resolution spectroscopy), or cross-disperser+straightening prism+grating (for

high-resolution spectroscopy), (10) transmission efficiencies through camera lenses (five AR coated lenses each optical arm), and (11) quantum efficiency estimates for the H2RG detectors (since we did not have time to measure the quantum efficiency we use conservative estimates of 80% from measurements of similar detectors). The effective instrument photometric throughput is shown in Figure 5.2 and the low- and high-resolution spectroscopy throughputs are shown in Figure 5.3 and 5.4 respectively.

Additionally, we calculate the instrument throughput for the slit-viewer camera using items (1)-(4) from the main instrument model as well as (5) reflection efficiency for the mirrored surfaces around the slits, (6) transmission efficiencies through the slit-viewer optics (four AR coated lenses), (7) reflection efficiency for mirror below collimator (95%), (8) transmission efficiencies for a J-band filter, and (9) quantum efficiency estimates for the InSb detector (since we did not have time to measure the quantum efficiency we use a conservative estimate of 70% from measurements of similar detectors).

5.4 RIMAS Observing Calculators

We have developed observing calculators for RIMAS users. These calculators are based on our instrument efficiency models and allow the user to calculate limiting magnitudes and exposure times for RIMAS. These calculators are available at <http://rimas.astro.umd.edu/> and the code is available on GitHub⁷. Figure 5.5 is an example of the online RIMAS observing calculators. We also make guide star

⁷https://github.com/vickitoy/observing_calculators

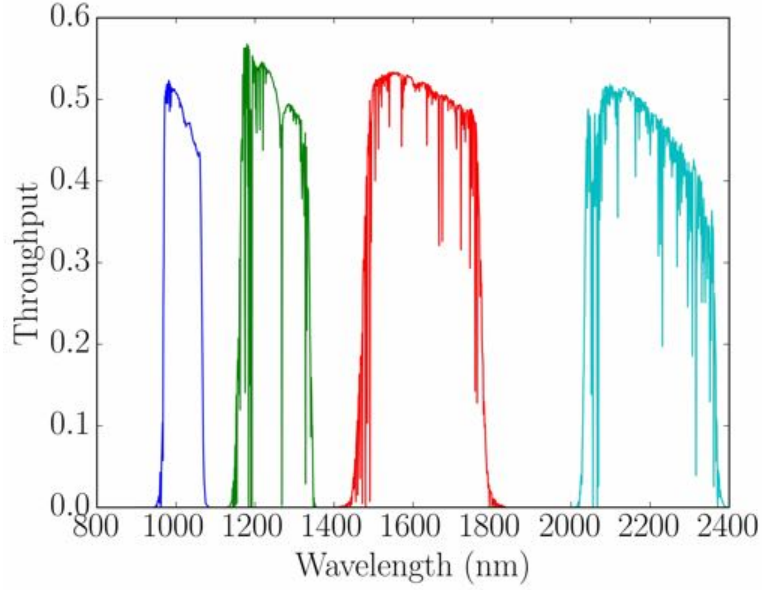


Figure 5.2 RIMAS photometric throughput.

calculations for the slit-viewer camera based on our instrument efficiency models.

5.4.1 Limiting Magnitudes

We calculate the limiting magnitude given a signal-to-noise ratio, exposure time, and instrument mode. We can start with the background noise level. The total noise of an image is a combination of dark noise, read noise, background photon noise, and signal photon noise. These are all independent and can be added in quadrature. We need to multiply the dark noise and read noise by the number of pixels that an object is smeared over because each pixel will contribute more noise. Thus the total background and detector noise is:

$$\sigma_{bgd+det}^2 = \sigma_{bgd}^2 + n_p \sigma_{dark}^2 + n_p \sigma_{read}^2 \quad (5.1)$$

where n_p is the number of pixels the object is smeared over. Assuming the signal

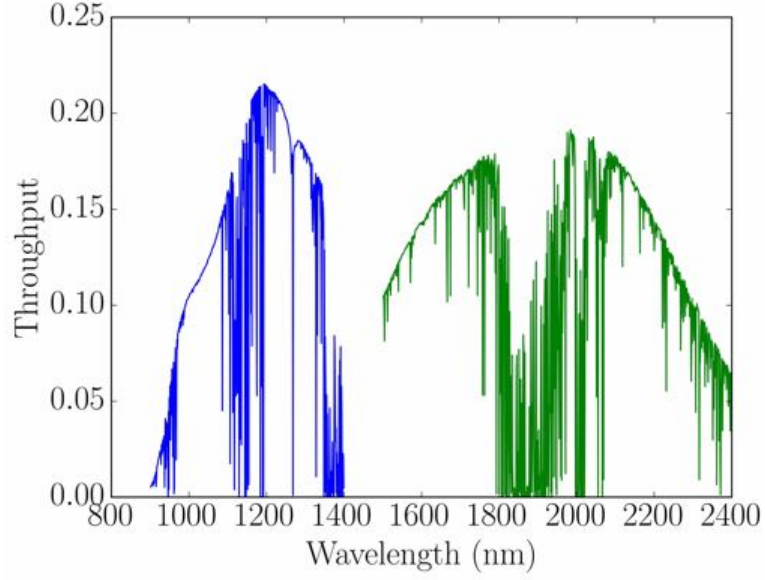


Figure 5.3 Low-resolution spectroscopy throughput for RIMAS.

follows Poisson statistics ($S_* = \sigma_{sig}^2$) and that we are measuring the signal and noise in terms of electrons:

$$SN = \frac{S_*}{\sqrt{\sigma_{sig}^2 + \sigma_{bgd+det}^2}} = \frac{S_*}{\sqrt{S + \sigma_{bgd+det}^2}} \quad (5.2)$$

This leads to a signal of:

$$S_* = 0.5 * \left(SN^2 + \sqrt{SN^4 + 4 \times SN^2 \times \sigma_{bgd+det}^2} \right) \quad (5.3)$$

Once we know the signal we can calculate the limiting flux and therefore limiting magnitude of the system for a particular signal-to- noise ratio. The flux of the signal is:

$$F = \frac{S_*}{A_{eff} \times \Delta\lambda \times t \times \epsilon} \quad (5.4)$$

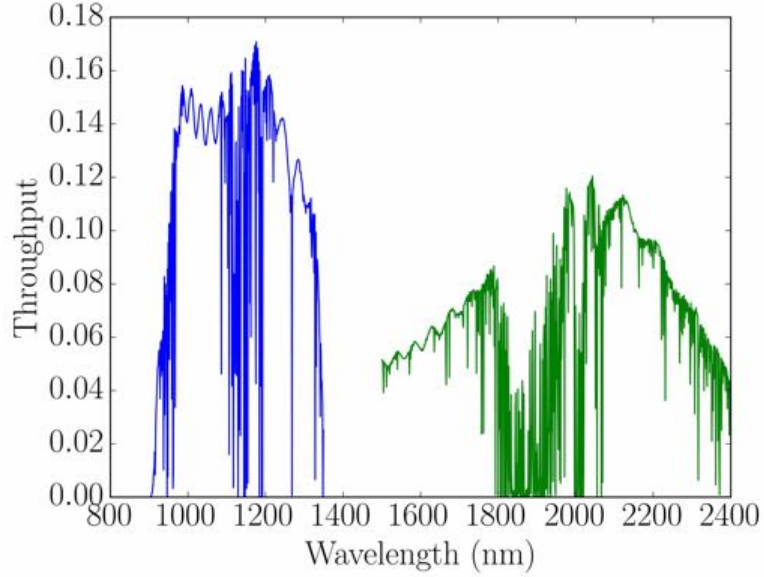


Figure 5.4 High-resolution spectroscopy throughput for RIMAS.

where A_{eff} is the effective area of the telescope, $\Delta\lambda$ is the bandpass, t is the exposure time, and ϵ is the instrument efficiency for the observing mode.

5.4.2 Exposure time calculator

We can also calculate the exposure time given a signal-to-noise ratio, signal magnitude, and instrument mode. From Equation 5.2 we know what the signal-to-noise ratio in terms of electrons. Given a signal magnitude for a point source, we can calculate the exposure time noting that the signal flux, background flux, and dark current are functions of exposure time:

$$t_{exp} = \frac{-B + \sqrt{B^2 - 4AC}}{2A} \quad (5.5)$$

where:

The image shows two side-by-side screenshots of a web browser. The left screenshot displays the 'RIMAS Observer Calculators' page with two calculator options: 'Limiting magnitude calculator' (selected) and 'Exposure time calculator'. The 'Limiting magnitude calculator' has input fields for Exposure time (60s), S/N ratio (10), Instrument Mode (Photometry), and Filter (Y). The 'Exposure time calculator' has input fields for AB Magnitude (20), S/N ratio (10), Instrument Mode (Photometry), and Filter (Y). A 'Submit' button is at the bottom. The right screenshot shows the results page titled 'Calculated AB limiting magnitude: 19.8'. It includes a table for 'Limiting Magnitude Calculator Inputs' and a table for 'Assumptions'.

Calculated AB limiting magnitude: 19.8

Limiting Magnitude Calculator Inputs:

Exposure time (s):	60
Signal-to-noise ratio:	10
Filter:	Y
Observing mode:	Photometry

Assumptions:

Telescope diameter:	428 cm
F/#:	2.47
Pixel size:	18 um
Plate scale:	0.35 "/pix
Secondary vignetting:	0.93
Binning:	1x1
Dark current:	0.005 e-/s
Read noise:	6 e-
Object spread over N pixels:	4
Observing mode efficiency:	0.447

Figure 5.5 Example of RIMAS limiting magnitude calculator that can be found at <http://rimas.astro.umd.edu/>

$$A = N_* - SN^2 \times D^2 \times n_p$$

$$B = -SN^2 \times (N_* + S_* \times n_p) \quad (5.6)$$

$$C = -SN^2 \times \sigma_{read}^2 \times n_p$$

N_* and S_* are the count rate in electrons per second of the source and background respectively. D is the dark current of the detector in electrons per second and σ_{read} is the read noise in electrons.

Table 5.1. Slit-viewer Limiting Magnitude SNR=5

t_{int} (s)	AB Mag
1	18.39
2	18.77
5	19.27

5.4.3 Guide Star Calculations

The InSb detector will be used as a guider during both high- and low-resolution spectroscopy mode. The slit-viewer camera will need to quickly relay position corrections to DCT and will guide on either the host galaxy or guide stars. In chapter 4 we reported the InSb detector characterization the InSb detector. If we assume that the detector met the *Spitzer* specifications of $1 e^-/s$ dark current and had a quantum efficiency of 70% based on previous IRAC testing on similar grade InSb detectors from the same batch, then we can use our instrument efficiency models to calculate a slit-viewer camera efficiency of 41%. We calculate limiting magnitudes from our limiting magnitude calculator for our slit-viewer camera using a J-band filter for a signal-to- noise ratio of 5 (Table 5.1).

The host galaxy magnitude drops off with redshift (Figure 5.6; Jakobsson et al., 2011) so even with our highest limiting magnitudes, we will be unable to guide on host galaxies of $z \gtrsim 0.5$. Although the GRB afterglow will be observable, almost all of the light from the GRB will be directed into the spectroscopic slit and we will be unable to use the afterglow as a guider other than sending position corrections when the afterglow shifts into view on the InSb detector. This will be more difficult to model. The preferred method is to use a guide star. Thus, we calculated the

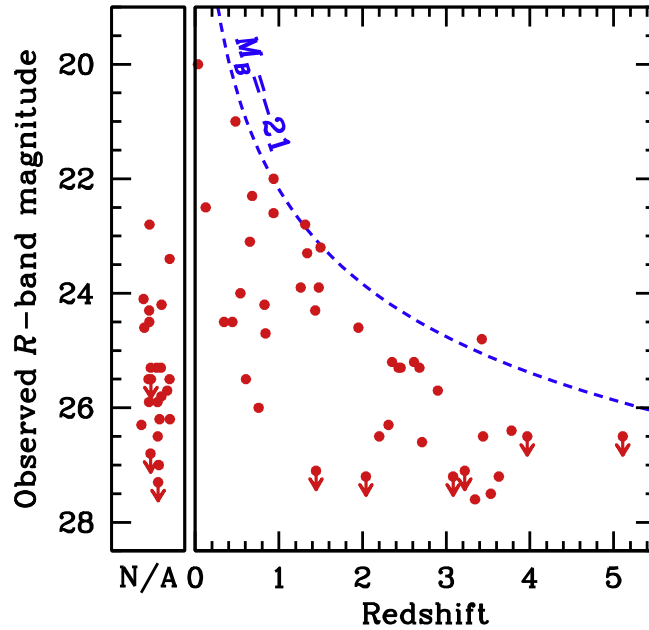


Figure 5.6 R-band host galaxy magnitude as a function of redshift. Figure from Jakobsson et al. (2011).

probability that at least one guide star is in our field of view.

2MASS is a useful tool for finding the number of stars within a field based on magnitude, however, 2MASS is only complete up to J-band magnitudes of ~ 15.5 -16. Instead, we used the Diffuse Infrared Background Experiment (DIRBE) Faint Source Model (Arendt et al., 1998) predictions for the cumulative counts of stars per square degree with our limiting magnitude for three fields (Figure 5.7): (l,b)=(5, 20), (l,b)=(75, -75), and (l,b)=(90, 30).

We calculated the probability of finding at least 1 guide star in each of our three test fields for a standard broadband J filter with $t_{int} = 1, 2, 5$ seconds for SN=5 (Table 5.2). At moderately low galactic latitudes there is a >80 -90% probability of finding a guide star. At higher galactic latitudes there is 40-60% probability of finding a guide star. In order to have a 99% probability of finding a guide star

Table 5.2. Guide Star Probabilities SNR=5

t_{int} (s)	Field (l,b)	N(<m) (stars/deg ²)	λ (stars/FOV)	P(0)	P(n>0)
1	(5,20)	2.3e4	8.92	1.3e-4	~1
	(75,-75)	1.4e3	0.54	0.58	0.42
	(90,30)	5.0e3	1.94	0.14	0.86
2	(5,20)	3.0e4	11.64	8.8e-6	~1
	(75,-75)	1.7e3	0.66	0.52	0.48
	(90,30)	6.0e3	2.33	9.7e-2	0.9
5	(5,20)	4.4e4	17.07	3.86e-8	~1
	(75,-75)	2.1e3	0.89	0.41	0.59
	(90,30)	7.0e3	2.71	6.7e-2	0.93

at these latitudes, our limiting magnitude would have to be >25 AB which is not realistic for the short integration times required for a guiding camera. Thus, there will be a high probability of guide stars in moderately low galactic latitudes and if there are no guide stars in the high galactic latitudes we will have to guide on the afterglow source that shifts off the spectroscopic slit.

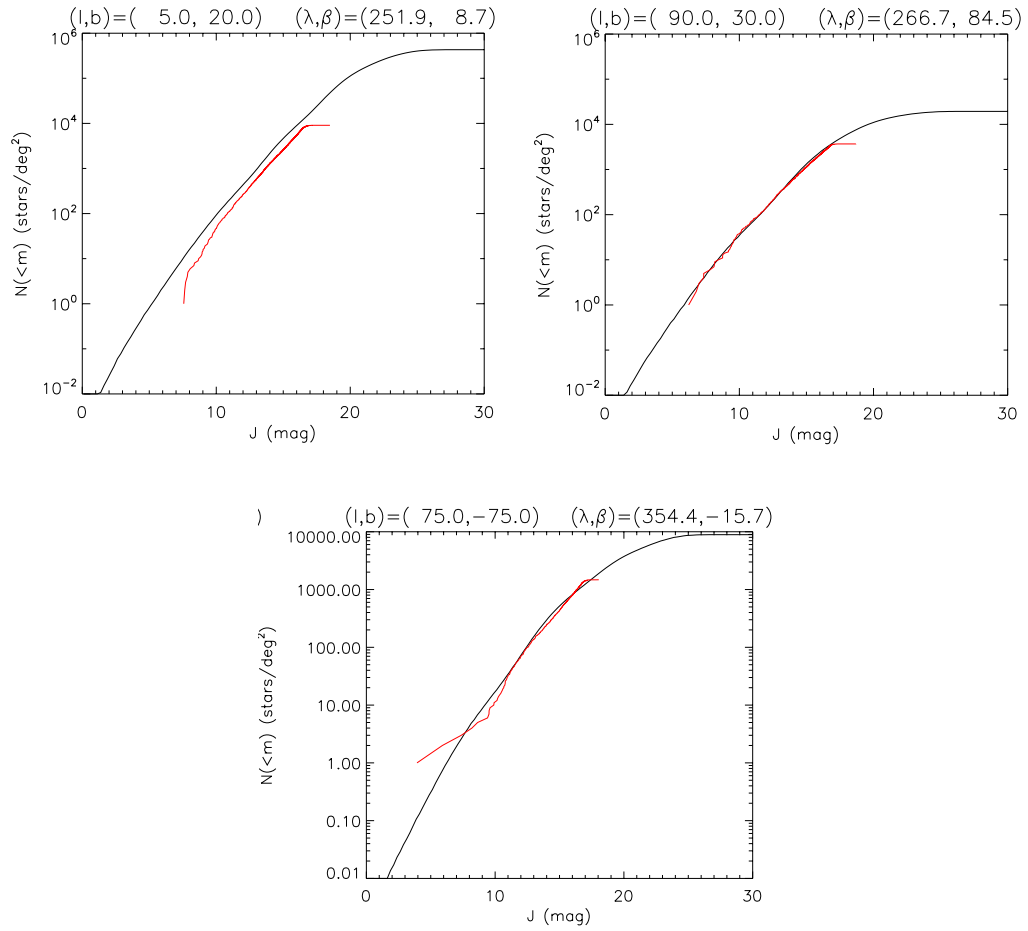


Figure 5.7 Cumulative distribution function for three fields in J magnitudes from DIRBE Faint Source Model in black and cumulative distribution from 2MASS in red (from private communication with Rick Arendt).

Chapter 6: Final considerations

This thesis has explored using GRB afterglows to probe the high-redshift universe. We began by examining the progenitors and host galaxies of long GRBs using existing instrumentation (both ground-based and space-based). Then we described the development of an upcoming near-infrared imager and spectrometer, RIMAS. RIMAS will be able to extend the observational studies outlined in this thesis and study both dusty and high-redshift GRB afterglows in the near future.

In chapter 2 we have performed a detailed analysis of a nearby supernova associated with a GRB (GRB 130702A/SN 2013dx) to use as a template for other GRB-SNe. SN 2013dx is a particularly interesting GRB-SNe because it has an $E_{\gamma,\text{iso}}$ that is intermediate between low-luminosity and cosmological GRB-SNe. We compared SN 2013dx to both SN Ic-BL with and without GRBs and looked in depth at the similarities and differences with the SN 1998bw. Then we examined the GRB characteristics with SN parameters of all 10 well-studied GRB-SNe to determine if we could use GRB parameters to identify SN explosion parameters for more distant bursts. We found there is no correlation between the parameters which indicates that the SN is not imprinted with information from the GRB. For future studies of GRB-SNe, late time follow-up of the SN will be critical to understanding the

asymmetric nature of these objects. We highly encourage deep and extensive study of these rare transient objects due to the small sample of GRB-SNe with detailed photometric and spectroscopic follow-up.

In chapter 3 we have analyzed the host galaxies of GRB associated with DLAs. Our sample increases the number of detected host galaxies with associated DLAs by a factor of three, from 13 to 46, and adds an additional 12 upper limits. We examined the host properties of our sample (star formation rates, stellar masses, etc.) and found that GRB-DLA galaxies tend to have higher detection rates and star formation rates than QSO-DLA galaxies. We suspect, despite overlapping HI column densities and redshift, that these objects may be from a different population than our GRB-DLA galaxies. Our GRB-DLA galaxy sample should be considered when comparing observations with cosmological simulations as our sample adds a significant number of DLA galaxy detections to a previously small sample. Future deep and multi-band observations can be conducted on the GRB-DLA host galaxies on the remainder of our sample to increase the number of detected GRB-DLA galaxies. Additionally, our sample only encompassed GRB-DLAs through mid-2014 and can be expanded to objects past this date.

In chapter 4 and chapter 5 we discuss the development of RIMAS's hardware and software respectively. In particular, these chapters cover the RIMAS detector characterization, the data reduction pipeline, and observing calculators. Both the detector hardware and data reduction software will allow observers to have better constraints on both the photometry and spectroscopy. Once RIMAS is permanently installed on the DCT, it will provide an extremely useful tool to rapidly follow-up

high-redshift GRB afterglows allowing study of galaxies and stars in the very early Universe.

Bibliography

- Aihara, H., Allende Prieto, C., An, D., et al. 2011, *ApJS*, 193, 29
- Arendt, R. G., Odegard, N., Weiland, J. L., et al. 1998, *ApJ*, 508, 74
- Arnett, D. 1996, *Supernovae and Nucleosynthesis: An Investigation of the History of Matter from the Big Bang to the Present* (Princeton: Princeton University Press.)
- Arnett, W. D. 1982, *ApJ*, 253, 785
- Asplund, M., Grevesse, N., Sauval, A. J., & Scott, P. 2009, *ARA&A*, 47, 481
- Astropy Collaboration, Robitaille, T. P., Tollerud, E. J., et al. 2013, *A&A*, 558, A33
- Atwood, W. B., Abdo, A. A., Ackermann, M., et al. 2009, *ApJ*, 697, 1071
- Barnes, L. A., & Haehnelt, M. G. 2009, *MNRAS*, 397, 511
- Barthelmy, S. D., Butterworth, P., Cline, T. L., et al. 1998, in *American Institute of Physics Conference Series*, Vol. 428, *Gamma-Ray Bursts*, 4th Hunstville Symposium, ed. C. A. Meegan, R. D. Preece, & T. M. Koshut, 99–103
- Barthelmy, S. D., Barbier, L. M., Cummings, J. R., et al. 2005, *Space Sci. Rev.*, 120, 143
- Basa, S., Cuby, J. G., Savaglio, S., et al. 2012, *A&A*, 542, A103
- Becker, R. H., Fan, X., White, R. L., et al. 2001, *AJ*, 122, 2850
- Bennett, C. L., Larson, D., Weiland, J. L., & Hinshaw, G. 2014, *ApJ*, 794, 135
- Berger, E. 2014, *ARA&A*, 52, 43
- Berger, E., Kulkarni, S. R., Frail, D. A., & Soderberg, A. M. 2003, *ApJ*, 599, 408
- Berger, E., Chornock, R., Holmes, T. R., et al. 2011, *ApJ*, 743, 204

- Bertin, E. 2006, in *Astronomical Society of the Pacific Conference Series*, Vol. 351, *Astronomical Data Analysis Software and Systems XV*, ed. C. Gabriel, C. Arviset, D. Ponz, & S. Enrique, 112
- Bertin, E., & Arnouts, S. 1996, *A&AS*, 117, 393
- Bertin, E., Mellier, Y., Radovich, M., et al. 2002, in *Astronomical Society of the Pacific Conference Series*, Vol. 281, *Astronomical Data Analysis Software and Systems XI*, ed. D. A. Bohlender, D. Durand, & T. H. Handley, 228
- Bietenholz, M. F., De Colle, F., Granot, J., Bartel, N., & Soderberg, A. M. 2014, *MNRAS*, 440, 821
- Bigiel, F., Leroy, A., Walter, F., et al. 2010, *AJ*, 140, 1194
- . 2008, *AJ*, 136, 2846
- Bird, S., Vogelsberger, M., Haehnelt, M., et al. 2014, *MNRAS*, 445, 2313
- Blanchard, P. K., Berger, E., & Fong, W.-f. 2016, *ApJ*, 817, 144
- Blanton, M. R., & Roweis, S. 2007, *AJ*, 133, 734
- Blondin, S., Modjaz, M., Kirshner, R., Challis, P., & Calkins, M. 2007, *Central Bureau Electronic Telegrams*, 808, 1
- Blondin, S., & Tonry, J. L. 2007, *ApJ*, 666, 1024
- Bolatto, A. D., Leroy, A. K., Jameson, K., et al. 2011, *ApJ*, 741, 12
- Bouché, N., Murphy, M. T., Kacprzak, G. G., et al. 2013, *Science*, 341, 50
- Bouwens, R. J., Illingworth, G. D., Oesch, P. A., et al. 2010, *ApJ*, 709, L133
- Briggs, M. S., Paciasas, W. S., Pendleton, G. N., et al. 1996, *ApJ*, 459, 40
- Bromberg, O., Nakar, E., & Piran, T. 2011, *ApJ*, 739, L55
- Bufano, F., Pian, E., Sollerman, J., et al. 2012, *ApJ*, 753, 67
- Burrows, D. N., Hill, J. E., Nousek, J. A., et al. 2005, *Space Sci. Rev.*, 120, 165
- Butler, N., Klein, C., Fox, O., et al. 2012, in *Society of Photo-Optical Instrumentation Engineers (SPIE) Conference Series*, Vol. 8446, 10
- Butler, N., Watson, A. M., Kutyrev, A., et al. 2013, *GRB Coordinates Network*, 14993, 1
- Campana, S., Mangano, V., Blustin, A. J., et al. 2006, *Nature*, 442, 1008
- Cannizzo, J. K., Barthelmy, S., Cummings, J. R., Melandri, A., & de Pasquale, M. 2013, *GCN Report*, 429

Cano, Z. 2013, MNRAS, 434, 1098
—, 2014, ApJ, 794, 121
Cano, Z., Bersier, D., Guidorzi, C., et al. 2011, ApJ, 740, 41
Cano, Z., de Ugarte Postigo, A., Perley, D., et al. 2015, arXiv e-prints (astro-ph/1505.03522), arXiv:1505.03522
Capone, J. 2016, PhD thesis, University of Maryland, College Park
Cappellaro, E., Mazzali, P. A., Benetti, S., et al. 1997, A&A, 328, 203
Cardelli, J. A., Clayton, G. C., & Mathis, J. S. 1989, ApJ, 345, 245
Castor, J. I. 1970, MNRAS, 149, 111
Castro, S., Galama, T. J., Harrison, F. A., et al. 2003, ApJ, 586, 128
Cenko, S. B., Gal-Yam, A., Kasliwal, M. M., et al. 2013, GRB Coordinates Network, 14998, 1
Cenko, S. B., Fox, D. B., Moon, D.-S., et al. 2006, PASP, 118, 1396
Cenko, S. B., Fox, D. B., Penprase, B. E., et al. 2008, ApJ, 677, 441
Chen, H.-W., Perley, D. A., Pollack, L. K., et al. 2009, ApJ, 691, 152
Chen, H.-W., Perley, D. A., Wilson, C. D., et al. 2010, ApJ, 723, L218
Cheung, T., Vianello, G., Zhu, S., et al. 2013, GRB Coordinates Network, 14971, 1
Chornock, R., Berger, E., Fox, D. B., et al. 2013, ApJ, 774, 26
Chornock, R., Berger, E., Levesque, E. M., et al. 2010, ArXiv e-prints, arXiv:1004.2262
Ciardi, B., & Loeb, A. 2000, ApJ, 540, 687
Clocchiatti, A., Suntzeff, N. B., Covarrubias, R., & Candia, P. 2011, AJ, 141, 163
Clocchiatti, A., & Wheeler, J. C. 1997, ApJ, 491, 375
Cobb, B. E., Bloom, J. S., Perley, D. A., et al. 2010, ApJ, 718, L150
Collazzi, A. C., & Connaughton, V. 2013, GRB Coordinates Network, 14972, 1
Cooke, J., & O'Meara, J. M. 2015, ApJ, 812, L27
Cooke, J., Wolfe, A. M., Gawiser, E., & Prochaska, J. X. 2006, ApJ, 652, 994
Corsi, A., Ofek, E. O., Frail, D. A., et al. 2011, ApJ, 741, 76

Costa, E., Frontera, F., Heise, J., et al. 1997, *Nature*, 387, 783

Covino, S., Melandri, A., Salvaterra, R., et al. 2013, *MNRAS*, 432, 1231

Crichton, N. H. M., Murphy, M. T., Prochaska, J. X., et al. 2015, *MNRAS*, 452, 217

Cucchiara, A., Fumagalli, M., Rafelski, M., et al. 2015, *ApJ*, 804, 51

Cucchiara, A., Levan, A. J., Fox, D. B., et al. 2011, *ApJ*, 736, 7

da Cunha, E., Charlot, S., & Elbaz, D. 2008, *MNRAS*, 388, 1595

da Cunha, E., Walter, F., Smail, I. R., et al. 2015, *ApJ*, 806, 110

Daddi, E., Dannerbauer, H., Krips, M., et al. 2009, *ApJ*, 695, L176

D’Avanzo, P., D’Elia, V., Tagliaferri, G., et al. 2013, *GRB Coordinates Network*, 14984, 1

D’Avanzo, P., Perri, M., Fugazza, D., et al. 2010, *A&A*, 522, A20

Davé, R., & Oppenheimer, B. D. 2007, *MNRAS*, 374, 427

Dawson, K. S., Schlegel, D. J., Ahn, C. P., et al. 2013, *AJ*, 145, 10

de Ugarte Postigo, A., Castro-Tirado, A. J., Gorosabel, J., et al. 2005, *A&A*, 443, 841

D’Elia, V., D’Avanzo, P., Melandri, A., et al. 2013, *GRB Coordinates Network*, 15000, 1

D’Elia, V., Fynbo, J. P. U., Goldoni, P., et al. 2014, *A&A*, 564, A38

D’Elia, V., Pian, E., Melandri, A., et al. 2015, *A&A*, 577, A116

Della Valle, M., Chincarini, G., Panagia, N., et al. 2006, *Nature*, 444, 1050

Deng, J., Tominaga, N., Mazzali, P. A., Maeda, K., & Nomoto, K. 2005, *ApJ*, 624, 898

Dessart, L., Hillier, D. J., Li, C., & Woosley, S. 2012, *MNRAS*, 424, 2139

Dessauges-Zavadsky, M., Calura, F., Prochaska, J. X., D’Odorico, S., & Matteucci, F. 2007, *A&A*, 470, 431

Drout, M. R., Soderberg, A. M., Gal-Yam, A., et al. 2011, *ApJ*, 741, 97

Eichler, D., Livio, M., Piran, T., & Schramm, D. N. 1989, *Nature*, 340, 126

Eisenstein, D. J., Weinberg, D. H., Agol, E., et al. 2011, *AJ*, 142, 72

- Elmegreen, B. G. 2015, *ApJ*, 814, L30
- Evans, P. A., Beardmore, A. P., Page, K. L., et al. 2009, *MNRAS*, 397, 1177
- Faber, S. M., Phillips, A. C., Kibrick, R. I., et al. 2003, in *Society of Photo-Optical Instrumentation Engineers (SPIE) Conference Series*, Vol. 4841, *Instrument Design and Performance for Optical/Infrared Ground-based Telescopes*, ed. M. Iye & A. F. M. Moorwood, 1657–1669
- Feroci, M., Frontera, F., Costa, E., et al. 1997, in *Proc. SPIE*, Vol. 3114, *EUV, X-Ray, and Gamma-Ray Instrumentation for Astronomy VIII*, ed. O. H. Siegmund & M. A. Gummin, 186–197
- Ferrero, P., Kann, D. A., Zeh, A., et al. 2006, *A&A*, 457, 857
- Filippenko, A. V. 1982, *PASP*, 94, 715
- . 1997, *ARA&A*, 35, 309
- Fisher, A., Branch, D., Nugent, P., & Baron, E. 1997, *ApJ*, 481, L89
- Fishman, G. J., & Meegan, C. A. 1995, *ARA&A*, 33, 415
- Font-Ribera, A., Miralda-Escudé, J., Arnau, E., et al. 2012, *J. Cosmology Astropart. Phys.*, 11, 059
- Förster Schreiber, N. M., Genzel, R., Bouché, N., et al. 2009, *ApJ*, 706, 1364
- Fowler, A. M., & Gatley, I. 1990, *ApJ*, 353, L33
- Fox, O. D., Kuttyrev, A. S., Rapchun, D. A., et al. 2012, in *Society of Photo-Optical Instrumentation Engineers (SPIE) Conference Series*, Vol. 8453, 1
- Friis, M., De Cia, A., Krühler, T., et al. 2015, *MNRAS*, 451, 167
- Fumagalli, M., O’Meara, J. M., Prochaska, J. X., & Kanekar, N. 2010, *MNRAS*, 408, 362
- Fumagalli, M., O’Meara, J. M., Prochaska, J. X., Kanekar, N., & Wolfe, A. M. 2014, *MNRAS*, 444, 1282
- Fumagalli, M., O’Meara, J. M., Prochaska, J. X., Rafelski, M., & Kanekar, N. 2015, *MNRAS*, 446, 3178
- Fumagalli, M., O’Meara, J. M., Prochaska, J. X., & Worseck, G. 2013, *ApJ*, 775, 78
- Fynbo, J. P. U., Jakobsson, P., Möller, P., et al. 2003, *A&A*, 406, L63
- Fynbo, J. P. U., Gorosabel, J., Smette, A., et al. 2005, *ApJ*, 633, 317
- Fynbo, J. P. U., Watson, D., Thöne, C. C., et al. 2006, *Nature*, 444, 1047

- Fynbo, J. P. U., Ledoux, C., Noterdaeme, P., et al. 2011, MNRAS, 413, 2481
- Fynbo, J. U., Møller, P., & Warren, S. J. 1999, MNRAS, 305, 849
- Gal-Yam, A. 2012, Science, 337, 927
- Gal-Yam, A., Moon, D.-S., Fox, D. B., et al. 2004, ApJ, 609, L59
- Gal-Yam, A., Fox, D. B., Price, P. A., et al. 2006, Nature, 444, 1053
- Galama, T. J., Vreeswijk, P. M., van Paradijs, J., et al. 1998, Nature, 395, 670
- Gawiser, E., Francke, H., Lai, K., et al. 2007, ApJ, 671, 278
- Gehrels, N., Ramirez-Ruiz, E., & Fox, D. B. 2009, ARA&A, 47, 567
- Gehrels, N., Chincarini, G., Giommi, P., et al. 2004, ApJ, 611, 1005
- Genzel, R., Tacconi, L. J., Eisenhauer, F., et al. 2006, Nature, 442, 786
- Giacomazzo, B., Perna, R., Rezzolla, L., Troja, E., & Lazzati, D. 2013, ApJ, 762, L18
- Glover, S. C. O., & Clark, P. C. 2012, MNRAS, 421, 9
- Gnedin, N. Y., & Kravtsov, A. V. 2010, ApJ, 714, 287
- Goldstein, A., Preece, R. D., Mallozzi, R. S., et al. 2013, ApJS, 208, 21
- Golenetskii, S., Aptekar, R., Pal'Shin, V., et al. 2013, GRB Coordinates Network, 14986, 1
- González-Casanova, D. F., De Colle, F., Ramirez-Ruiz, E., & Lopez, L. A. 2014, ApJ, 781, L26
- Graham, J. F., & Fruchter, A. S. 2013, ApJ, 774, 119
- Greiner, J., Mazzali, P. A., Kann, D. A., et al. 2015a, Nature, 523, 189
- Greiner, J., Fox, D. B., Schady, P., et al. 2015b, ApJ, 809, 76
- Guaita, L., Acquaviva, V., Padilla, N., et al. 2011, ApJ, 733, 114
- Gunn, J. E., & Peterson, B. A. 1965, ApJ, 142, 1633
- Hamuy, M. 2003, ApJ, 582, 905
- Hibon, P., Cuby, J.-G., Willis, J., et al. 2010, A&A, 515, A97
- Hinkle, K. H., Wallace, L., & Livingston, W. 2003, in Bulletin of the American Astronomical Society, Vol. 35, American Astronomical Society Meeting Abstracts, 1260

- Hjorth, J., & Bloom, J. S. 2012, *The Gamma-Ray Burst - Supernova Connection* (Cambridge University Press: Cambridge), 169–190
- Hjorth, J., Malesani, D., Jakobsson, P., et al. 2012, *ApJ*, 756, 187
- Hogg, D. W., Baldry, I. K., Blanton, M. R., & Eisenstein, D. J. 2002, arXiv e-prints (astro-ph/0210394), astro-ph/0210394
- Hopkins, A. M., Rao, S. M., & Turnshek, D. A. 2005, *ApJ*, 630, 108
- Horne, K. 1986, *PASP*, 98, 609
- Hunt, L. K., Palazzi, E., Michałowski, M. J., et al. 2014, *A&A*, 565, A112
- Iwamoto, K., Mazzali, P. A., Nomoto, K., et al. 1998, *Nature*, 395, 672
- Iwamoto, K., Nakamura, T., Nomoto, K., et al. 2000, *ApJ*, 534, 660
- Jakobsson, P., Malesani, D., Hjorth, J., Fynbo, J. P. U., & Milvang-Jensen, B. 2011, in *American Institute of Physics Conference Series*, Vol. 1358, American Institute of Physics Conference Series, ed. J. E. McEnery, J. L. Racusin, & N. Gehrels, 265–270
- Japelj, J., Vergani, S. D., Salvaterra, R., et al. 2016, ArXiv e-prints, arXiv:1604.01034
- Jeffery, D. J. 1989, *ApJS*, 71, 951
- Jimenez, R., Bowen, D. V., & Matteucci, F. 1999, *ApJ*, 514, L83
- Jorgenson, R. A., Murphy, M. T., & Thompson, R. 2013, *MNRAS*, 435, 482
- Jorgenson, R. A., Murphy, M. T., Thompson, R., & Carswell, R. F. 2014, *MNRAS*, 443, 2783
- Jorgenson, R. A., & Wolfe, A. M. 2014, *ApJ*, 785, 16
- Kalberla, P. M. W., Burton, W. B., Hartmann, D., et al. 2005, *A&A*, 440, 775
- Kaneko, Y., Ramirez-Ruiz, E., Granot, J., et al. 2007, *ApJ*, 654, 385
- Kann, D. A., Klose, S., & Zeh, A. 2006, *ApJ*, 641, 993
- Kann, D. A., Klose, S., Zhang, B., et al. 2010, *ApJ*, 720, 1513
- Kelly, P. L., Filippenko, A. V., Fox, O. D., Zheng, W., & Clubb, K. I. 2013, *ApJ*, 775, L5
- Kelson, D. D. 2003, *PASP*, 115, 688
- Kennicutt, Jr., R. C. 1998, *ApJ*, 498, 541

- Kinney, A. L., Calzetti, D., Bohlin, R. C., et al. 1996, *ApJ*, 467, 38
- Klebesadel, R. W., Strong, I. B., & Olson, R. A. 1973, *ApJ*, 182, L85
- Kocevski, D., West, A. A., & Modjaz, M. 2009, *ApJ*, 702, 377
- Kocevski, D., Modjaz, M., Bloom, J. S., et al. 2007, *ApJ*, 663, 1180
- Kouveliotou, C., Meegan, C. A., Fishman, G. J., et al. 1993, *ApJ*, 413, L101
- Krogager, J.-K., Fynbo, J. P. U., Møller, P., et al. 2012, *MNRAS*, 424, L1
- Krug, H. B., Veilleux, S., Tilvi, V., et al. 2012, *ApJ*, 745, 122
- Krühler, T., Greiner, J., Schady, P., et al. 2011, *A&A*, 534, A108
- Krühler, T., Ledoux, C., Fynbo, J. P. U., et al. 2013, *A&A*, 557, A18
- Krumholz, M. R. 2012, *ApJ*, 759, 9
- . 2013, *MNRAS*, 436, 2747
- . 2014, *Phys. Rep.*, 539, 49
- Krumholz, M. R., McKee, C. F., & Tumlinson, J. 2009, *ApJ*, 699, 850
- Kulkarni, S. R., Frail, D. A., Wieringa, M. H., et al. 1998, *Nature*, 395, 663
- Lang, D., Hogg, D. W., Mierle, K., Blanton, M., & Roweis, S. 2010, *AJ*, 139, 1782
- Lanzetta, K. M., Yahata, N., Pascarelle, S., Chen, H.-W., & Fernández-Soto, A. 2002, *ApJ*, 570, 492
- Laskar, T., Berger, E., & Chary, R.-R. 2011, *ArXiv e-prints*, arXiv:1102.1022
- Law, N. M., Kulkarni, S. R., Dekany, R. G., et al. 2009, *PASP*, 121, 1395
- Leach, R. W., & Low, F. J. 2000, in *Proc. SPIE*, Vol. 4008, *Optical and IR Telescope Instrumentation and Detectors*, ed. M. Iye & A. F. Moorwood, 337–343
- Levan, A. J., Tanvir, N. R., Fruchter, A. S., et al. 2014, *ApJ*, 792, 115
- Levesque, E. M., Berger, E., Kewley, L. J., & Bagley, M. M. 2010, *AJ*, 139, 694
- Lithwick, Y., & Sari, R. 2001, *ApJ*, 555, 540
- Lyman, J., Bersier, D., James, P., et al. 2014a, *ArXiv e-prints*, arXiv:1406.3667
- Lyman, J. D., Bersier, D., & James, P. A. 2014b, *MNRAS*, 437, 3848
- MacFadyen, A. I., & Woosley, S. E. 1999, *ApJ*, 524, 262
- Madau, P. 1995, *ApJ*, 441, 18

- Madau, P., Ferguson, H. C., Dickinson, M. E., et al. 1996, *MNRAS*, 283, 1388
- Maeda, K., Nakamura, T., Nomoto, K., et al. 2002, *ApJ*, 565, 405
- Malesani, D., Tagliaferri, G., Chincarini, G., et al. 2004, *ApJ*, 609, L5
- Margutti, R., Milisavljevic, D., Soderberg, A. M., et al. 2014a, *ApJ*, 797, 107
- . 2014b, *ApJ*, 797, 107
- Marmo, C., & Bertin, E. 2008, in *Astronomical Society of the Pacific Conference Series*, Vol. 394, *Astronomical Data Analysis Software and Systems XVII*, ed. R. W. Argyle, P. S. Bunclark, & J. R. Lewis, 619
- Matheson, T., Filippenko, A. V., Ho, L. C., Barth, A. J., & Leonard, D. C. 2000, *AJ*, 120, 1499
- Matheson, T., Garnavich, P. M., Stanek, K. Z., et al. 2003, *ApJ*, 599, 394
- Mawatari, K., Inoue, A. K., Kousai, K., et al. 2016, *ApJ*, 817, 161
- Mazzali, P. A., McFadyen, A. I., Woosley, S. E., Pian, E., & Tanaka, M. 2014, *MNRAS*, 443, 67
- Mazzali, P. A., Walker, E. S., Pian, E., et al. 2013, *MNRAS*, 432, 2463
- Mazzali, P. A., Kawabata, K. S., Maeda, K., et al. 2005, *Science*, 308, 1284
- Mazzali, P. A., Deng, J., Pian, E., et al. 2006, *ApJ*, 645, 1323
- McBreen, S., Krühler, T., Rau, A., et al. 2010, *A&A*, 516, A71
- McGuire, J. T. W., Tanvir, N. R., Levan, A. J., et al. 2015, *ArXiv e-prints*, arXiv:1512.07808
- McLean, I. S., Steidel, C. C., Epps, H. W., et al. 2012, in *Society of Photo-Optical Instrumentation Engineers (SPIE) Conference Series*, Vol. 8446, 0
- Meegan, C., Lichti, G., Bhat, P. N., et al. 2009, *ApJ*, 702, 791
- Meegan, C. A., Fishman, G. J., Wilson, R. B., et al. 1992, *Nature*, 355, 143
- Melandri, A., Pian, E., Ferrero, P., et al. 2012, *A&A*, 547, A82
- Melandri, A., Pian, E., D’Elia, V., et al. 2014, *A&A*, 567, A29
- Metzger, M. R., Djorgovski, S. G., Kulkarni, S. R., et al. 1997, *Nature*, 387, 878
- Milisavljevic, D., Margutti, R., Parrent, J. T., et al. 2015, *ApJ*, 799, 51
- Mirabal, N., Halpern, J. P., An, D., Thorstensen, J. R., & Terndrup, D. M. 2006, *ApJ*, 643, L99

- Modjaz, M., Liu, Y. Q., Bianco, F. B., & Graur, O. 2015, ArXiv e-prints, arXiv:1509.07124
- Modjaz, M., Stanek, K. Z., Garnavich, P. M., et al. 2006, ApJ, 645, L21
- Modjaz, M., Kewley, L., Kirshner, R. P., et al. 2008, AJ, 135, 1136
- Modjaz, M., Li, W., Butler, N., et al. 2009, ApJ, 702, 226
- Modjaz, M., Blondin, S., Kirshner, R. P., et al. 2014, AJ, 147, 99
- Møller, P., & Warren, S. J. 1993, A&A, 270, 43
- Møller, P., Warren, S. J., Fall, S. M., Fynbo, J. U., & Jakobsen, P. 2002, ApJ, 574, 51
- Monet, D. G., Levine, S. E., Canzian, B., et al. 2003, AJ, 125, 984
- Mulchaey, J., Kasliwal, M. M., Arcavi, I., Bellm, E., & Kelson, D. 2013a, GRB Coordinates Network, 14985, 1
- . 2013b, The Astronomer’s Telegram, 5191, 1
- Murphy, M. T., & Bernet, M. L. 2016, MNRAS, 455, 1043
- Nagamine, K., Wolfe, A. M., Hernquist, L., & Springel, V. 2007, ApJ, 660, 945
- Nakar, E. 2015, arXiv e-prints (astro-ph/1503.00441), arXiv:1503.00441
- Narayan, R., Paczynski, B., & Piran, T. 1992, ApJ, 395, L83
- Neeleman, M., Prochaska, J. X., Zwaan, M. A., et al. 2016, ApJ, 820, L39
- Noterdaeme, P., Ledoux, C., Petitjean, P., & Srianand, R. 2008, A&A, 481, 327
- Noterdaeme, P., Petitjean, P., Ledoux, C., & Srianand, R. 2009, A&A, 505, 1087
- Noterdaeme, P., Petitjean, P., Pâris, I., et al. 2014, A&A, 566, A24
- Noterdaeme, P., Petitjean, P., Carithers, W. C., et al. 2012a, A&A, 547, L1
- Noterdaeme, P., Laursen, P., Petitjean, P., et al. 2012b, A&A, 540, A63
- Oesch, P. A., Bouwens, R. J., Illingworth, G. D., et al. 2012, ApJ, 759, 135
- Oke, J. B., & Gunn, J. E. 1982, PASP, 94, 586
- . 1983, ApJ, 266, 713
- Oke, J. B., Cohen, J. G., Carr, M., et al. 1995, PASP, 107, 375
- Olivares E., F., Greiner, J., Schady, P., et al. 2012, A&A, 539, A76

- . 2015, *A&A*, 577, A44
- O’Meara, J. M., Chen, H.-W., & Kaplan, D. L. 2006, *ApJ*, 642, L9
- O’Meara, J. M., Prochaska, J. X., Burles, S., et al. 2007, *ApJ*, 656, 666
- O’Meara, J. M., Prochaska, J. X., Worseck, G., Chen, H.-W., & Madau, P. 2013, *ApJ*, 765, 137
- Parrent, J. T., Milisavljevic, D., Soderberg, A. M., & Parthasarathy, M. 2015, *ArXiv e-prints*, arXiv:1505.06645
- Patat, F., Cappellaro, E., Danziger, J., et al. 2001, *ApJ*, 555, 900
- Pei, Y. C. 1992, *ApJ*, 395, 130
- Pendleton, G. N., Paciesas, W. S., Briggs, M. S., et al. 1994, *ApJ*, 431, 416
- Perley, D. A., Cenko, S. B., Bloom, J. S., et al. 2009, *AJ*, 138, 1690
- Perley, D. A., Morgan, A. N., Updike, A., et al. 2011, *AJ*, 141, 36
- Perley, D. A., Levan, A. J., Tanvir, N. R., et al. 2013, *ApJ*, 778, 128
- Perley, D. A., Cenko, S. B., Corsi, A., et al. 2014, *ApJ*, 781, 37
- Perley, D. A., Krühler, T., Schulze, S., et al. 2016a, *ApJ*, 817, 7
- Perley, D. A., Tanvir, N. R., Hjorth, J., et al. 2016b, *ApJ*, 817, 8
- Péroux, C., Bouché, N., Kulkarni, V. P., York, D. G., & Vladilo, G. 2012, *MNRAS*, 419, 3060
- Péroux, C., McMahon, R. G., Storrie-Lombardi, L. J., & Irwin, M. J. 2003, *MNRAS*, 346, 1103
- Péroux, C., Quiret, S., Rahmani, H., et al. 2016, *MNRAS*, 457, 903
- Phillips, M. M. 1993, *ApJ*, 413, L105
- Pian, E., Mazzali, P. A., Masetti, N., et al. 2006, *Nature*, 442, 1011
- Piran, T. 1999, *Phys. Rep.*, 314, 575
- . 2004, *Reviews of Modern Physics*, 76, 1143
- Piro, A. L., & Nakar, E. 2013, *ApJ*, 769, 67
- Planck Collaboration, Ade, P. A. R., Aghanim, N., et al. 2016, *A&A*, 594, A13
- Prochaska, J. X., Chen, H.-W., Dessauges-Zavadsky, M., & Bloom, J. S. 2007, *ApJ*, 666, 267

Prochaska, J. X., Herbert-Fort, S., & Wolfe, A. M. 2005, *ApJ*, 635, 123

Prochaska, J. X., O’Meara, J. M., & Worseck, G. 2010, *ApJ*, 718, 392

Prochaska, J. X., & Wolfe, A. M. 1997, *ApJ*, 487, 73

—. 2009, *ApJ*, 696, 1543

Prochaska, J. X., Sheffer, Y., Perley, D. A., et al. 2009, *ApJ*, 691, L27

Racusin, J. L., Liang, E. W., Burrows, D. N., et al. 2009, *ApJ*, 698, 43

Rafelski, M., Gardner, J. P., Fumagalli, M., et al. 2016, *ArXiv e-prints*, arXiv:1604.08597

Rafelski, M., Neeleman, M., Fumagalli, M., Wolfe, A. M., & Prochaska, J. X. 2014, *ApJ*, 782, L29

Rafelski, M., Wolfe, A. M., & Chen, H.-W. 2011, *ApJ*, 736, 48

Rafelski, M., Wolfe, A. M., Prochaska, J. X., Neeleman, M., & Mendez, A. J. 2012, *ApJ*, 755, 89

Rahmati, A., & Schaye, J. 2014, *MNRAS*, 438, 529

Rahmati, A., Schaye, J., Bower, R. G., et al. 2015, *MNRAS*, 452, 2034

Rahmati, A., Schaye, J., Crain, R. A., et al. 2016, *MNRAS*, 459, 310

Rau, A., Kulkarni, S. R., Law, N. M., et al. 2009, *PASP*, 121, 1334

Rauscher, B. J., Lindler, D. J., Mott, D. B., et al. 2011, *PASP*, 123, 953

Rauscher, B. J., Boehm, N., Cagiano, S., et al. 2014, *PASP*, 126, 739

Ribaudo, J., Lehner, N., & Howk, J. C. 2011, *ApJ*, 736, 42

Rieke, G. H. 2007, *ARA&A*, 45, 77

Roming, P. W. A., Kennedy, T. E., Mason, K. O., et al. 2005, *Space Sci. Rev.*, 120, 95

Salvaterra, R., Della Valle, M., Campana, S., et al. 2009, *Nature*, 461, 1258

Sari, R., Piran, T., & Narayan, R. 1998, *ApJ*, 497, L17

Savaglio, S., Glazebrook, K., & Le Borgne, D. 2009, *ApJ*, 691, 182

Schady, P., Dwelly, T., Page, M. J., et al. 2012, *A&A*, 537, A15

Schlafly, E. F., & Finkbeiner, D. P. 2011, *ApJ*, 737, 103

Schmidt, M. 1959, *ApJ*, 129, 243

- Schulze, S., Leloudas, G., Xu, D., et al. 2013, GRB Coordinates Network, 14994, 1
- Schulze, S., Fynbo, J. P. U., Milvang-Jensen, B., et al. 2012, A&A, 546, A20
- Schulze, S., Malesani, D., Cucchiara, A., et al. 2014, A&A, 566, A102
- Silverman, J. M., Kong, J. J., & Filippenko, A. V. 2012, MNRAS, 425, 1819
- Silverman, J. M., Vinko, J., Marion, G. H., et al. 2015, MNRAS, 451, 1973
- Singer, L. P., Cenko, S. B., Kasliwal, M. M., et al. 2013a, ApJ, 776, L34
- . 2013b, GRB Coordinates Network, 14967, 1
- Skrutskie, M. F., Cutri, R. M., Stiening, R., et al. 2006, AJ, 131, 1163
- Sobolev, V. V. 1960, *Moving envelopes of stars* (Cambridge: Harvard University Press)
- Soderberg, A. M., Chakraborti, S., Pignata, G., et al. 2010, Nature, 463, 513
- Sollerman, J., Holland, S. T., Challis, P., et al. 2002, A&A, 386, 944
- Sollerman, J., Jaunsen, A. O., Fynbo, J. P. U., et al. 2006, A&A, 454, 503
- Sparre, M., Hartoog, O. E., Krühler, T., et al. 2014, ApJ, 785, 150
- Srianand, R., Hussain, T., Noterdaeme, P., et al. 2016, MNRAS, arXiv:1604.06475
- Stanek, K. Z., Matheson, T., Garnavich, P. M., et al. 2003, ApJ, 591, L17
- Stanway, E. R., Levan, A. J., Tanvir, N. R., Wiersema, K., & van der Laan, T. P. R. 2015, ApJ, 798, L7
- Starling, R. L. C., Wiersema, K., Levan, A. J., et al. 2011, MNRAS, 411, 2792
- Steele, I. A., Smith, R. J., Rees, P. C., et al. 2004, in *Society of Photo-Optical Instrumentation Engineers (SPIE) Conference Series*, Vol. 5489, *Ground-based Telescopes*, ed. J. M. Oschmann, Jr., 679–692
- Steidel, C. C., Giavalisco, M., Dickinson, M., & Adelberger, K. L. 1996, AJ, 112, 352
- Storrie-Lombardi, L. J., & Wolfe, A. M. 2000, ApJ, 543, 552
- Sutherland, P. G., & Wheeler, J. C. 1984, ApJ, 280, 282
- Tanvir, N. R., Levan, A. J., Fruchter, A. S., et al. 2013, Nature, 500, 547
- Tanvir, N. R., Fox, D. B., Levan, A. J., et al. 2009, Nature, 461, 1254
- Thomas, R. C., Nugent, P. E., & Meza, J. C. 2011, PASP, 123, 237

Thomsen, B., Hjorth, J., Watson, D., et al. 2004, *A&A*, 419, L21

Thöne, C. C., Campana, S., Lazzati, D., et al. 2011, *MNRAS*, 414, 479

Thöne, C. C., Fynbo, J. P. U., Goldoni, P., et al. 2013, *MNRAS*, 428, 3590

Tilvi, V., Rhoads, J. E., Hibon, P., et al. 2010, *ApJ*, 721, 1853

Tinney, C., Stathakis, R., Cannon, R., et al. 1998, *IAU Circ.*, 6896

Toy, V. L., Kuttyrev, A. S., Lyness, E. I., et al. 2014, in *Proc. SPIE*, Vol. 9147, Ground-based and Airborne Instrumentation for Astronomy V, 91472W

Toy, V. L., Cucchiara, A., Veilleux, S., et al. 2016a, *ApJ*, 832, 175

Toy, V. L., Kuttyrev, A. S., Capone, J. I., et al. 2016b, in *Proc. SPIE*, Vol. 9147, Ground-based and Airborne Instrumentation for Astronomy VI, 91472W

Toy, V. L., Cenko, S. B., Silverman, J. M., et al. 2016c, *ApJ*, 818, 79

Troja, E., Sakamoto, T., Guidorzi, C., et al. 2012, *ApJ*, 761, 50

Tyson, N. D. 1988, *ApJ*, 329, L57

Umeda, H., & Nomoto, K. 2008, *ApJ*, 673, 1014

Usov, V. V. 1992, *Nature*, 357, 472

Valenti, S., Benetti, S., Cappellaro, E., et al. 2008, *MNRAS*, 383, 1485

van Dokkum, P. G. 2001, *PASP*, 113, 1420

van Paradijs, J., Groot, P. J., Galama, T., et al. 1997, *Nature*, 386, 686

Wade, R. A., & Horne, K. 1988, *ApJ*, 324, 411

Wang, F. Y., & Dai, Z. G. 2014, *ApJS*, 213, 15

Wang, W.-H., Chen, H.-W., & Huang, K.-Y. 2012, *ApJ*, 761, L32

Watson, A. M., Richer, M. G., Bloom, J. S., et al. 2012, in *Society of Photo-Optical Instrumentation Engineers (SPIE) Conference Series*, Vol. 8444, 5

Weatherley, S. J., Warren, S. J., Møller, P., et al. 2005, *MNRAS*, 358, 985

Wheeler, J. C., Johnson, V., & Clocchiatti, A. 2015, *MNRAS*, 450, 1295

Wijers, R. A. M. J., & Galama, T. J. 1999, *ApJ*, 523, 177

Wijers, R. A. M. J., Rees, M. J., & Meszaros, P. 1997, *MNRAS*, 288, L51

Wolfe, A. M., & Chen, H.-W. 2006, *ApJ*, 652, 981

- Wolfe, A. M., Gawiser, E., & Prochaska, J. X. 2005, *ARA&A*, 43, 861
- Wolfe, A. M., & Prochaska, J. X. 1998, *ApJ*, 494, L15
- Wolfire, M. G., McKee, C. F., Hollenbach, D., & Tielens, A. G. G. M. 2003, *ApJ*, 587, 278
- Woosley, S. E. 1993, *ApJ*, 405, 273
- Woosley, S. E., & Bloom, J. S. 2006, *ARA&A*, 44, 507
- Xu, D., de Ugarte Postigo, A., Leloudas, G., et al. 2013, *ApJ*, 776, 98
- Yaron, O., & Gal-Yam, A. 2012, *PASP*, 124, 668
- Zafar, T., Péroux, C., Popping, A., et al. 2013, *A&A*, 556, A141
- Zafar, T., Watson, D., Fynbo, J. P. U., et al. 2011, *A&A*, 532, A143
- Zafar, T., Watson, D. J., Malesani, D., et al. 2010, *A&A*, 515, A94
- Zhang, B.-B., Fan, Y.-Z., Shen, R.-F., et al. 2012, *ApJ*, 756, 190
- Zwaan, M. A., & Prochaska, J. X. 2006, *ApJ*, 643, 675